X-811-71-40

NASA TM X 65669

ARRAYS OF LARGE APERTURE ANTENNAS—AN EXPERIMENTAL EVALUATION

FEBRUARY 1971

Reproduced by
NATIONAL TECHNICAL
INFORMATION SERVICE
Springfield, Va. 22151

GSFC

GODDARD SPACE FLIGHT CENTER

GREENBELT, MARYLAND

FACILITY FORM 602

N71-33372 (ACCESSION NUMBER)
109 (PAGES)
TMX 65669 (NASA CR OR TMX OR AD NUMBER)
(THRU) G3
(CODE) 07
(CATEGORY)

X-811-71-40

ARRAYS OF LARGE APERTURE ANTENNAS —

AN EXPERIMENTAL EVALUATION

Leonard F. Deerkoski

February 1971

GODDARD SPACE FLIGHT CENTER
Greenbelt, Maryland

PRECEDING PAGE BLANK NOT FILMED

ARRAYS OF LARGE APERTURE ANTENNAS - AN EXPERIMENTAL EVALUATION

Leonard F. Deerkoski

ABSTRACT

The system requirements for arrays of large aperture antennas are presented. Several alternative phasing and weighting techniques are analyzed for their suitability in providing optimum gain improvement for the array over that of the elements. The gain improvement capability of a two element array of large aperture antennas using a phase lock receiver with automatic gain control weighting was measured and found to provide within 0.5 db of the theoretical maximum. These measurements were made at VHF and S-band while tracking spacecraft. A digital time delay compensation system was developed that extends the bandwidth capability of a two element array at up to 2800 feet separation by a factor of 50 times. The time delay compensation system had no detectable effect upon the coherent receiver used for predetection combining.

PRECEDING PAGE BLANK NOT FILMED

CONTENTS

		Page
1	INTRODUCTION	1
2	RECEIVER REQUIREMENTS	1
	2.1 Coherence	1
	2.2 Weighting	8
	2.2.1 Selection Diversity	8
	2.2.2 Equal Gain Diversity	8
	2.2.3 Maximal Ratio Weighting	9
	2.2.3a Out of Band Noise Detection	12
	2.2.3b Correlation Detectors	12
	2.2.3c Non Coherent AGC	15
	2.2.3d Bandpass Limiter	15
	2.2.4 Coherent AGC Weighting	24
	2.3 Time Delay	29
3	EXPERIMENTS	45
	3.1 Measurement Technique	45
	3.2 VHF Results	52
	3.3 S-Band Results	66
4	SUMMARY	74
Appendix A	Economics of Arrays	77
Appendix B	Phase Front Distortion	89
5	ACKNOWLEDGEMENT	99
	REFERENCES	100

ILLUSTRATIONS

Figure		Page
2-1	Geometry for Calculation of Differential Doppler Frequency Shifts	2
2-2	Receiver for Arraying Independently Steerable Antennas (Reference 1)	4
2-3	Simplified Block Diagram of the APDAR Receiver	5
2-4	Functional Block Diagram of a Phase Stripping Receiver (Reference 3)	6
2-5	Maximal Ratio Weighting Using Out of Band Noise Detectors	13
2-6	Maximal Ratio Weighting Using Correlation Detector Output	14
2-7	Block Diagram of Coherent Receiver with Non Coherent AGC Loops	16
2-8	Output from a Non Coherent AGC with 0 dbm Output C + N	17
2-9	SNR Characteristics of a Bandpass Limiter	18
2-10	Maximal Ratio Weighting Circuit Using Bandpass Limiter	19
2-11	Output Carrier Level (C') vs. Input CNR for a Bandpass Limiter	20
2-12	Effects of Interference, $\left(\frac{C}{N}\right)_{IF}$ = +15 db	21
2-13	Effects of Interference, $\left(\frac{C}{N}\right)_{IF}$ = +10 db	22
2-14	Effects of Interference, $\left(\frac{C}{N}\right)_{IF}$ = +5 db	23
2-15	Effects of Interference, $\left(\frac{C}{N}\right)_{IF}$ = 0 db	24
2-16	Comparison of Performance for Equal Gain, Selection and Maximal Ratio Diversity Weighting Techniques (Reference 10)	25

ILLUSTRATIONS (Continued)

Figure		Page
2-17	System Model for Studying APDAR AGC Weighting Process.....	26
2-18	Maximum Theoretical SNR Improvement vs. Input Conditions ...	30
2-19	CNR Improvement vs. Relative Carrier Levels for Several Channel Noise Conditions.....	31
2-20	CNR Improvement vs. Relative Carrier Levels for Several Channel Gain Conditions.....	32
2-21	Maximum CNR Improvement vs. System Parameters for a Receiver with AGC Weighting	33
2-22	Model for Determining Time of Arrival Delay.....	34
2-23	Maximum SNR Loss at Band Edge vs. Bandwidth for Several Antenna Spacings	35
2-24	Minimum Element Spacing vs. Minimum Elevation to Prevent Shadowing.....	36
2-25	Transient Response of a 720 Nanosecond Transmission Line Time Delay Breadboard Model Using RG 178/U Coaxial Cable ..	37
2-26	Transient Response of an 8 Section Lumped Parameter Network Breadboard Model	38
2-27	Incorporation of Time Delay System into APDAR Receiver	39
2-28	Block Diagram of Time Delay Compensation System.....	41
2-29	Block Diagram of Time Delay System with Automatic Control...	42
2-30	Effect of Time Delay Switching on Receiver AGC	43
2-31	Effect of Time Delay Switching on Relative Channel Phase.....	44
3-1	Site Layout of Antenna Combing Range	46
3-2	Block Diagram of Measurement Scheme	48

ILLUSTRATIONS (Continued)

Figure		Page
3-3	Sampling Switch	49
3-4	Typical Detection Sequence for CNR Measurements	50
3-5	Two Element VHF Array and Electronics Van	53
3-6	Circuit Diagram of Monopulse Network for a Five Element Yagi Array	54
3-7	Sum Pattern of YAGI Array, RHC Polarization	55
3-8	Azimuth Difference Pattern for YAGI Array, RHC Polarization	56
3-9	Combined Results Including Data from Channels 1 and 2	57
3-10	Cumulative Distribution of the Measured and Expected Gain Improvement (ATS-C Experiment)	58
3-11	RELAY 2 Experiment, 180' Antenna Spacing	59
3-12	ESSA-6 Experiment, 180' Antenna Spacing	60
3-13	RELAY 2 Experiment, 440' Antenna Spacing	62
3-14	ESSA-3 Experiment, 440' Antenna Spacing	63
3-15	RELAY 2 Experiment, 900' Antenna Spacing	64
3-16	RELAY 2 Experiment, 900' Antenna Spacing	65
3-17	Two Element Array of 15' Diameter Parabolic Antennas at S-Band	67
3-18	Block Diagram of S-Band Feed and Monopulse Network	68
3-19a	Sum Channel in Azimuth Plane for RHC and LHC Polarization	69
3-19b	Azimuth Error Channel in Azimuth Plane for RHC and LHC Polarization	70

ILLUSTRATIONS (Continued)

Figure		Page
3-20	Block Diagram of Converter Preamplifier	71
3-21	Block Diagram of S-Band System	72
3-22	Gain Improvement Distribution Over Input Channels	73
A-1	Antenna Gain vs. Surface Tolerance (Reference 15)	78
A-2	State of the Art Gain vs. Antenna Diameter for 2, 6, 10, and 30 GHz	79
A-3	Cost of Construction and 10 Year Maintenance of Several Array Sizes vs. Gain at 2 GHz	83
A-4	Cost of Construction and 10 Year Maintenance of Several Array Sizes at 6 GHz	84
A-5	Cost of Construction and 10 Year Maintenance of Several Array Sizes at 10 GHz	85
A-6	Cost of Construction and 10 Year Maintenance of Several Array Sizes at 15 GHz	86
A-7	Cost of Construction and 10 Year Maintenance of Several Array Sizes at 30 GHz	87
B-1	Maximum Gain Loss vs. Antenna Diameter for Tropospheric Phase Front Distortion, F = 6 GHz	91
B-2	Maximum Gain Loss vs. Antenna Diameter for Tropospheric Phase Front Distortion, F = 10 GHz	92
B-3	Maximum Gain Loss vs. Antenna Diameter for Tropospheric Phase Front Distortion, F = 15 GHz	93
B-4	Maximum Gain Loss vs. Antenna Diameter for Tropospheric Phase Front Distortion, F = 30 GHz	94

ILLUSTRATIONS (Continued)

Figure		Page
B-5	Angle of Arrival Fluctuations vs. Frequency	96
B-6	Maximum Gain Loss vs. Frequency for Ionospheric Phase Front Distortion	97

ARRAYS OF LARGE APERTURE ANTENNAS — AN EXPERIMENTAL EVALUATION

1 INTRODUCTION

The achievement of high gain receiving capability with a single aperture antenna is limited by both technical and economic factors. The economic limitations result from the requirement of maintaining the reflector surface accuracy (Appendix A). The technical limitations include the effects of phase front distortion (Appendix B) as well as the ability to maintain reflector surface tolerance.

This report is a summary of the system requirements of large aperture arrays and the results of gain improvement and relative phase measurements at VHF and S-band. A two element array was used at each frequency. These experiments were designed to permit a more detailed gain improvement analysis of large aperture arrays than previous work in this area at Ohio State University [1].

2 RECEIVER REQUIREMENTS

2.1 Coherence

A signal transmitted from a spacecraft will, in general, differ in phase and frequency when received at the array elements. The received carrier will contain a doppler frequency shift determined by the relative velocity of the spacecraft with respect to the receiving antenna. The one way doppler shift is given by

$$F_d = \frac{v_r}{c} F_o \tag{1}$$

where

F_d = doppler frequency shift

v_r = relative velocity

F_o = carrier frequency

c = velocity of light

The relative velocity of spacecraft to ground antenna will, in general, be unique and the v_r seen by one antenna in an array will not be equal to that for any other array element. Figure 2-1 depicts the situation for a two element array at a separation D. The relative velocity of the spacecraft seen by antenna 2 is then given by

$$v_2 = v_1 \cos \alpha$$

where

$$\alpha = \sin^{-1}\left[\frac{D}{R_1} \sin \beta\right]$$

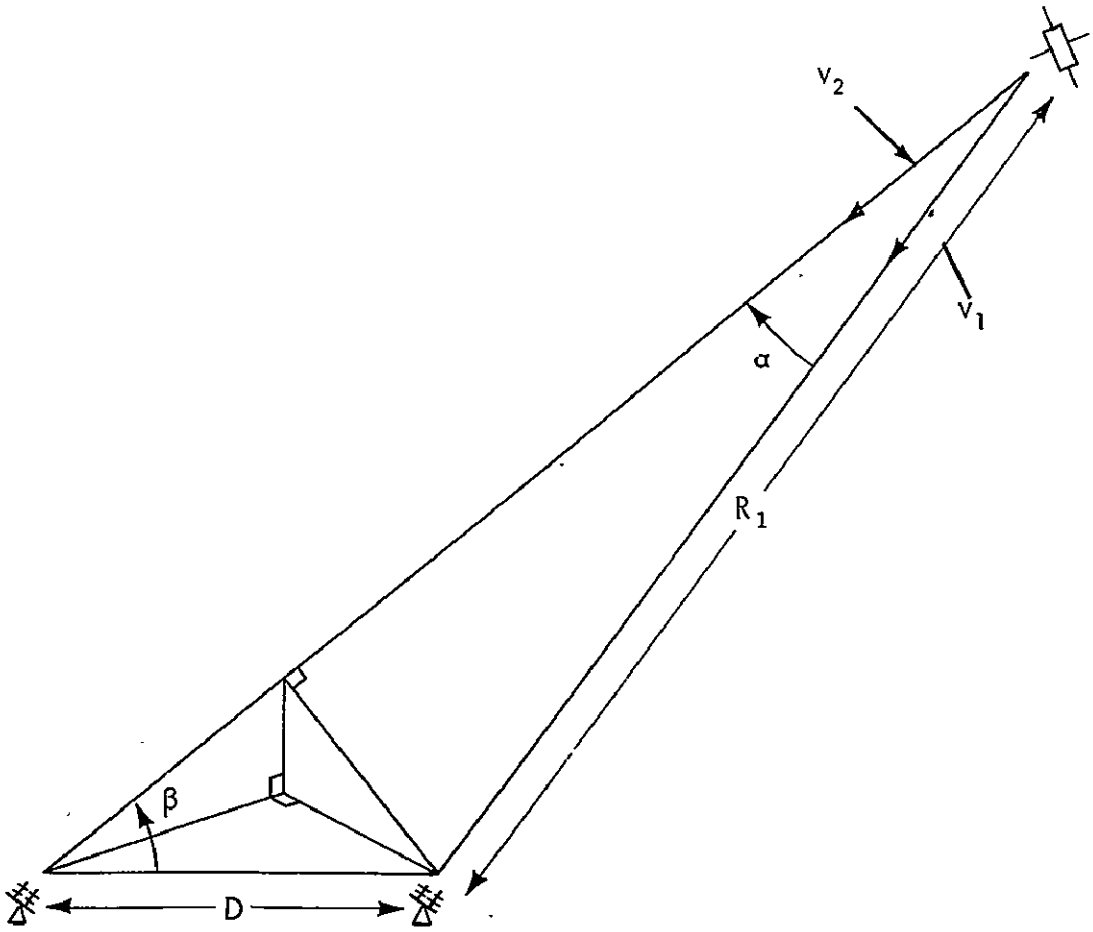

Figure 2-1: Geometry for Calculation of Differential Doppler Frequency Shifts

and using Equation (1), the differential doppler between array elements can be expressed as

$$F_1 - F_2 = \frac{v_1}{c} F_o \left\{ 1 - \cos \left[\sin^{-1} \left(\frac{D}{R_1} \sin \beta \right) \right] \right\} \quad (2)$$

The differential doppler frequency shift is a function of the transmitted frequency as well as the satellite orbit, antenna separation and baseline orientation. The differential doppler shift at VHF was less than one Hertz for the spacecraft tracked but was several Hertz at S-band.

The receiver used for a spaced array is therefore required to coherently combine signals which, in general, are of different phase and frequency. The requirement is complicated by the doppler frequency shifts common to both antennas which were 40 kHz, typically, at S-band when tracking OGO-6. A receiver using n + 1 phase lock loops for an array of n elements (Figure 2-2) was suggested by Shraeder [2] for this application. Shraeder's circuit converts the incoming signals to baseband prior to combining. It would be more efficient to first combine the individual channels of the array and thereby raise the signal to noise ratio at IF prior to baseband detection. This improvement was incorporated into the General Dynamics Advanced Polarization Diversity Autotrack Receiver (APDAR) in which combining is done at an 11 MHz IF frequency [3]. A block diagram of the APDAR is shown in Figure 2-3.

The APDAR receiver uses three phase lock loops (PLL) to perform the coherence operation. Each input channel is heterodyned to 11 MHz and locked to an internal reference. The 11 MHz signals are then combined and the output supplied to a third PLL that closes on each of the input channels. The input PLLs are second order with selectable 1, 3, 10 and 30 Hz tracking bandwidth, providing good phase control up to ±5 kHz from the carrier. The combined loop is third order, with selectable 10, 30, 100 and 300 Hz tracking bandwidth, providing the ±250 kHz operating range required for large doppler frequency shifts. The receiver was designed to operate at frequencies up to 10 GHz and therefore provides more operational range than required for either the VHF or S-band programs. The measured phase lock threshold for the receiver is -130 dbm at the input terminal.

Another method of meeting the coherence requirement is to use a phase stripping circuit [4]. A simplified block diagram of this circuit is shown in Figure 2-4. The phase stripping process can be shown by

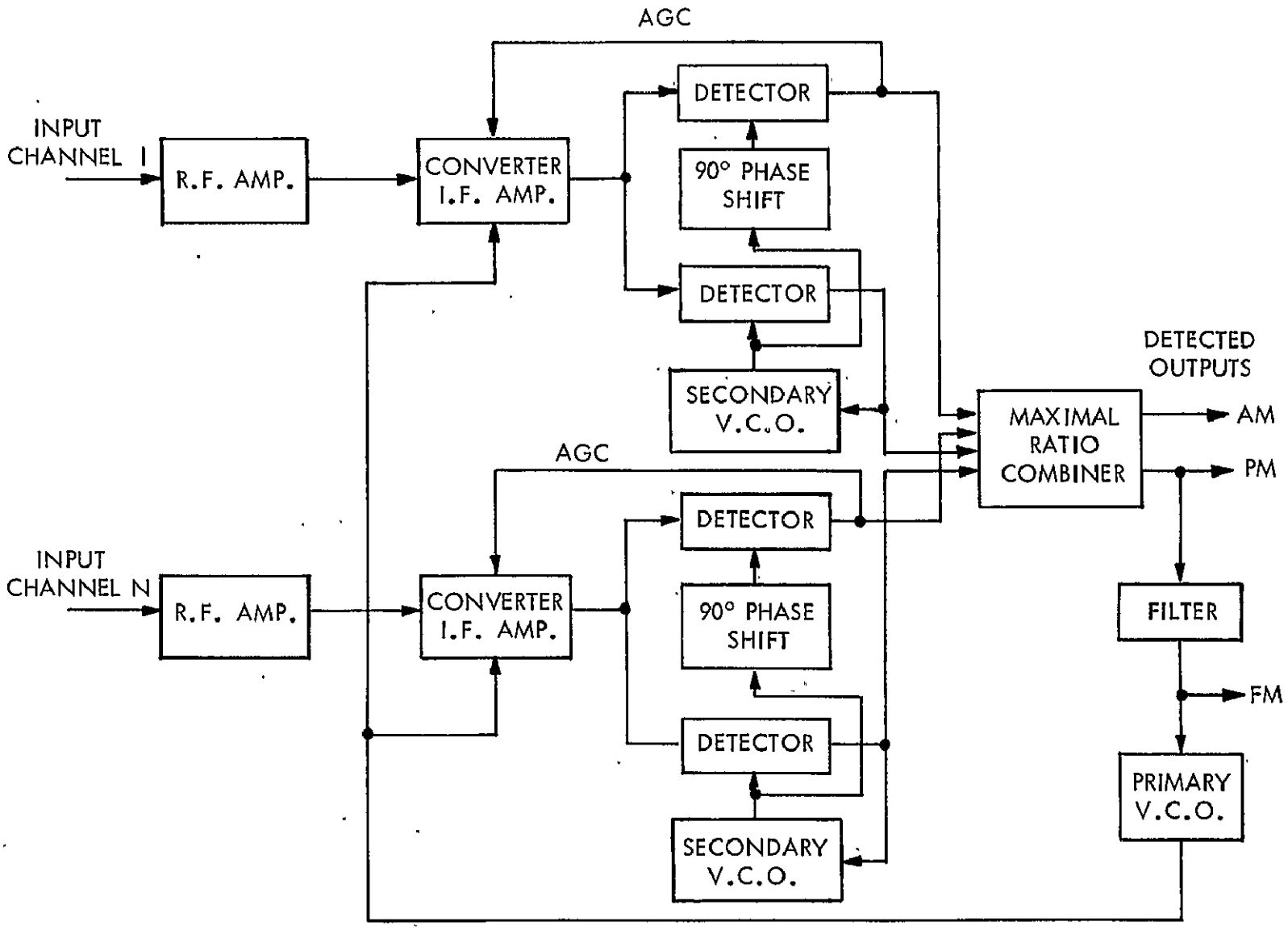

Figure 2-2: Receiver for Arraying Independently Steerable Antennas (Reference 1)

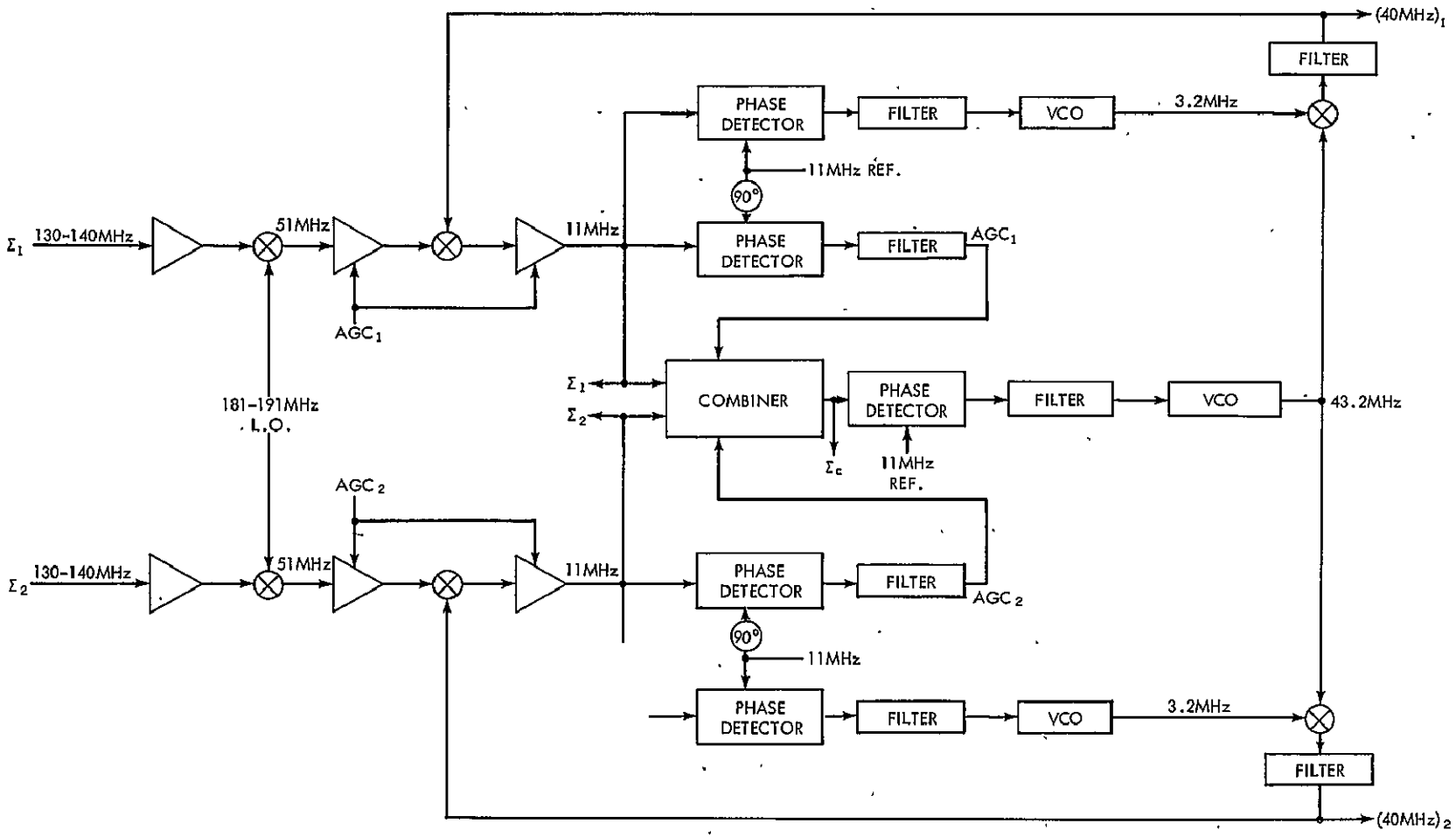

Figure 2-3: Simplified Block Diagram of the APDAR Receiver

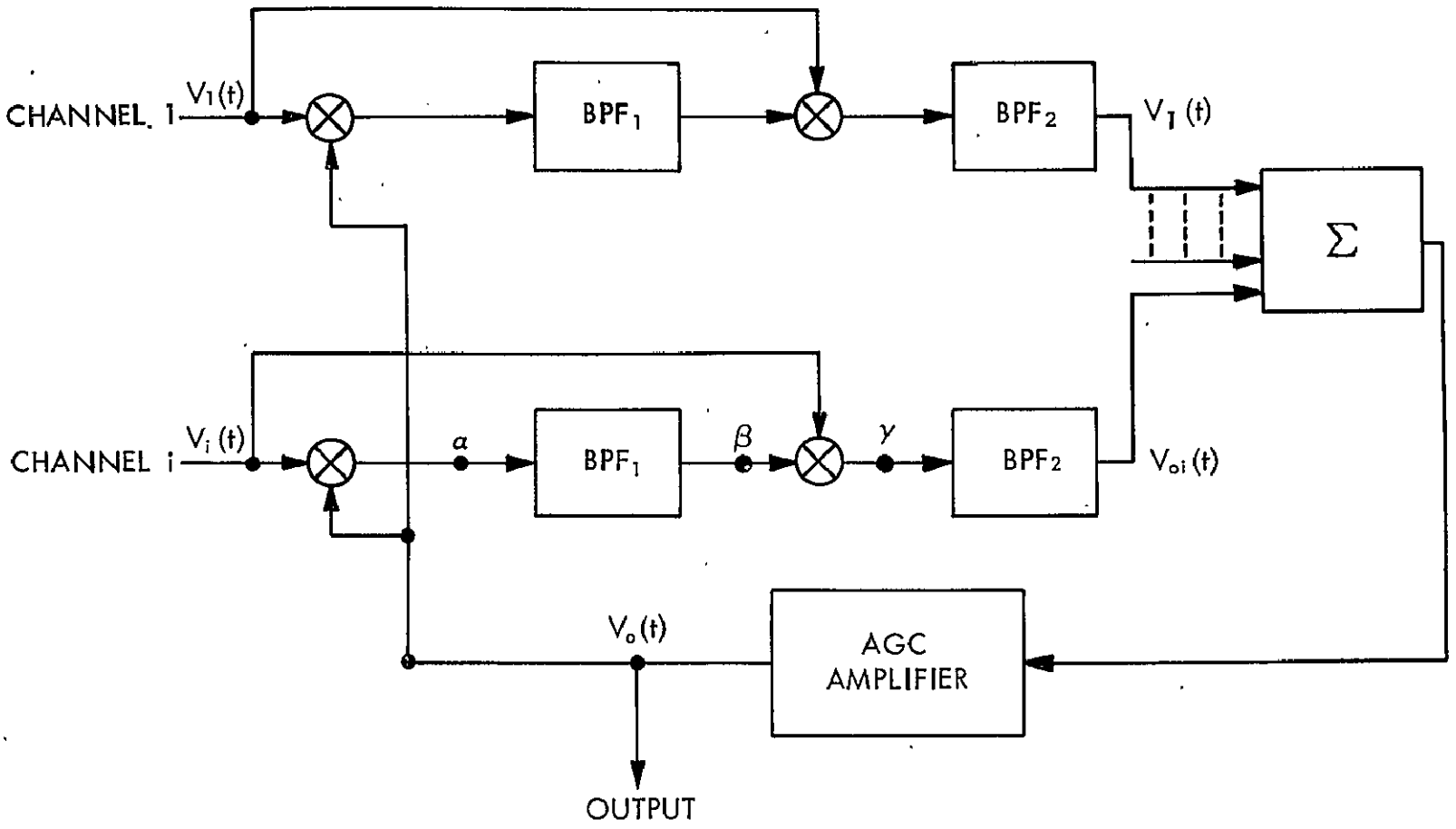

Figure 2-4: Functional Block Diagram of a Phase Stripping Receiver (Reference 3)

considering an idealized noiseless condition with the i^{th} input channel given by

$$V_i(t) = A \cos(\omega_1 t + \theta_i)$$

where θ_i is an arbitrary phase term associated with channel i. Assuming that the combined output signal has the form

$$V_o(t) = C \cos(\omega_o t + \phi)$$

then the signal at α will be

$$V_\alpha(t) = \frac{AC}{2}\left\{\cos\left[(\omega_1 + \omega_o)\, t + \theta_i + \phi\right] + \cos\left[(\omega_1 - \omega_o)\, t + \theta_i - \phi\right]\right\}$$

Passing $V_\alpha(t)$ through an infinitely narrow bandpass filter BPF_1 with center frequency ω_{IF} which corresponds to the lower sideband of $V_\alpha(t)$, that is

$$\omega_{IF} = \omega_1 - \omega_o,$$

we then have at point β

$$V_\beta(t) = \frac{AC}{2}\left\{\cos(\omega_1 - \omega_o)\, t + \theta_i - \phi\right\}$$

The product of $V_i(t)$ and $V_\beta(t)$ at point γ is then given by

$$V_\gamma = \frac{A^2C}{4}\left\{\left[\cos(\omega_{IF} + \omega_1)\, t + 2\theta_i - \phi\right] + \left[\cos(\omega_1 - \omega_{IF})\, t + \phi\right]\right\}$$

The phase term θ_i is present only in the upper sideband of V_γ. By passing only the lower sideband with filter BPF_2 the output signal from the i^{th} channel is independent of the phase characteristic of that channel as indicated below.

$$V_{oi} = \frac{A^2C}{4}\left[\cos \omega_o t + \phi\right]$$

Using this process in each of n input channels, the outputs supplied to the combiner will be coherent and independent of relative phase differences between channels.

A detailed analysis of this technique is given in Reference [3]. The circuit, in addition to achieving phase coherence, also weights each channel on the basis of the carrier level in that channel (assuming BPF_1 infinitely narrow, passing only the carrier frequency). If the noise levels in each channel can be assumed identical and if the sum of the channel gains is a constant (no independent AGC control) then this circuit weighting will approximate ratio squared weighting (Section 2.2.3 of this report). The conditions required for the weighting process to work effectively make this circuit more restrictive than an AGC weighting system (Section 2.2.4 of this report). In addition, the finite bandwidth of the filter BPF_1 will introduce multiplicative noise terms at the combiner. The idealized phase stripping circuit, at best, approaches the sensitivity and weighting capability of phase lock receivers for communication applications.

2.2 Weighting

The coherence conditions described above will be sufficient to realize maximum gain improvement when the received CNRs are equal in each input channel. In general, however, the CNRs will not be identical and a weighting process must be included to provide maximum output CNR for a given set of input conditions. Listed and described below are the major classifications of weighting schemes.

2.2.1 Selection Diversity

The receiver selects the channel with the greatest S or S/N level. In either case only one of the channels contributes to the output. Therefore, all the information present in the weaker channel is lost. The effectiveness of this weighting technique is greatest when only one channel has a significant S/N, in which case the remaining channels can be disregarded without fear of losing valuable information.

2.2.2 Equal Gain Diversity

The receiver combines the channels directly with no regard for their relative S or S/N levels. A severely degraded S/N in a channel can reduce the total output SNR below that in the best input channel. This technique works best in situations where channel SNRs can be expected

to be close to identical. This weighting scheme is sometimes referred to as "adding linearly".

2.2.3 Maximum Ratio Weighting

This weighting scheme seeks to optimize the combining process by maximizing the output signal to noise ratio (SNR). The maximum output SNR can be derived from the input signal levels (S_ℓ) and input noise levels (N_ℓ). Assuming that the receiver adjusts the phase of each array channel so that the IF signals are coherent, the S_ℓ levels will add as their voltage while the N_ℓ levels (assuming the noise incoherent[1]) will add as their power. The combined output signal and noise power can be expressed as

$$S_o^2 = \left(\sum_{\ell=1}^{n} S_\ell k_\ell \right)^2$$

$$N_o^2 = \sum_{\ell=1}^{n} N_\ell^2 k_\ell^2 \qquad (1)$$

where k_ℓ is the scalar weighting function imposed on the ℓth channel. Using Swartz's inequality [6]

$$\left[\sum_{j=1}^{k} \mu_j v_j \right]^2 \leq \left[\sum_{j=1}^{k} \mu_j^2 \right] \cdot \left[\sum_{j=1}^{k} v_j^2 \right]$$

the output signal (S_o) can be rewritten as

$$S_o^2 \leq \left[\sum_{\ell=1}^{n} S_\ell^2 \right] \left[\sum_{\ell=1}^{n} k_\ell^2 \right]$$

[1] In a properly designed system, the noise received by the elements of an array of large aperture antennas will be incoherent unless a strong radio star falls within the main beam of the antennas [5].

and dividing by Equation (1) the output signal to noise ratio becomes

$$\frac{S_o^2}{N_o^2} \leq \sum_{\ell=1}^{n} \left(\frac{S_\ell^2}{N_\ell^2} \right) \tag{2}$$

The maximum achievable output signal to noise ratio is the sum of the input signal to noise ratios.

In order to determine the optimum weighting coefficient, a two element array will first be considered. The channel 1 weighting coefficient k_1 will be assumed arbitrary but constant and the output SNR will be maximized by selecting the value of the channel 2 weighting coefficient k_2. The output SNR is given by

$$\frac{S_o}{N_o} = \frac{k_1 S_1 + k_2 S_2}{\sqrt{k_1^2 N_1^2 + k_2^2 N_2^2}} \tag{3}$$

Differentiating $\frac{S_o}{N_o}$ with respect to k_2 and equating the result to zero gives

$$k_2 = \left(k_1 \frac{N_1^2}{S_1} \right) \cdot \frac{S_2}{N_2^2} \tag{4}$$

Equation (4) defines k_2 for maximum output SNR under any input conditions and arbitrary k_1. This relation unfortunately defines the weighting coefficient of channel 2 in terms of both channel 1 and channel 2 signal and noise characteristics. Since an expression for the weighting function of each channel of an array of n elements is desired, an expression for k_2 in terms of only channel 2 characteristics is needed. In order to achieve this goal, the as yet arbitrary weighting function k_1 need only be defined as

$$k_1 = \frac{S_1}{N_1^2}$$

in which case k_2 would be similarly defined in terms of channel 2 characteristics only.

Using this weighting technique, the output SNR from an array of n elements can be derived. The output signal and noise will be given by

$$S_o^2 = \left[\sum_{\ell=1}^{n} S_\ell \cdot \left(\frac{S_\ell}{N_\ell^2} \right) \right]^2 \tag{5}$$

$$N_o^2 = \sum_{\ell=1}^{n} N_\ell^2 \cdot \left(\frac{S_\ell}{N_\ell^2} \right)^2 \tag{6}$$

where

$$k_\ell = \frac{S_\ell}{N_\ell^2}$$

and dividing Equation (5) by Equation (6) the output SNR is given by

$$\left(\frac{S_o}{N_o} \right)^2 = \sum_{\ell=1}^{n} \left(\frac{S_\ell}{N_\ell} \right)^2 \tag{7}$$

This output SNR [Equation (7)], derived for a receiver which weights each channel directly as the signal voltage level and inversely as the noise power in a given channel, is equal to the maximum possible output SNR as defined by Equation (2). This weighting scheme is commonly termed "maximal ratio weighting".

Implementing maximal ratio weighting requires measurement of both signal and noise in each channel. There are three basic techniques for performing this type of weighting, each exhibiting certain undesirable features.

2.2.3a Out of Band Noise Detectors

In a phase lock receiver, the carrier component of the received signal is readily available as the AGC voltage. Assuming a white noise spectrum about the carrier, the noise in a small band outside the bandwidth of the received carrier and modulation will be proportional to the noise within the received signal bandwidth. The out of band noise can be measured and squared to provide an output proportional to the mean square noise within the received signal bandwidth. The ratio of carrier voltage to mean square noise is just the difference of the logarithms of the two quantities. The circuit for this process is given in Figure 2-5. The limitations in this technique are listed below.

1. A narrow noise bandwidth must be used to avoid detection of modulation on the received carrier. Therefore, this technique is susceptible to interference from modulation on carriers transmitted by spacecraft within the vicinity of the desired spacecraft.

2. The sampled noise bandwidth should be as close as possible to the desired carrier to avoid overlapping bandwidths from other spacecraft. However, the signal bandwidths from spacecraft vary widely and the noise BW must be sufficiently far enough from the received carrier to accommodate the widest bandwidth downlink available.

2.2.3b Correlation Detectors

The noise within a narrow band about the received carrier can be measured directly if the carrier can be suppressed and if there is no modulation present within that noise bandwidth. Separation of carrier and noise in this manner has been attempted for measuring the carrier-to-noise ratio of phase lock loop channels [7]. An adaptation of this circuit to accomplish ratio squared weighting is shown in Figure 2-6. This circuit will provide ratio squared weighting under the following conditions.

1. Only PCM/PM exist on the carrier. Any non-discrete phase modulation (such as PFM/PM) or wide band phase modulation will provide a continuous frequency spectrum about the carrier and therefore the noise cannot be isolated.

2. The dynamic range of the technique is limited both by the internal receiver thermal noise and by the residual phase noise on the receiver phase lock reference [7]. The significance of these factors in practice has not yet been fully evaluated.

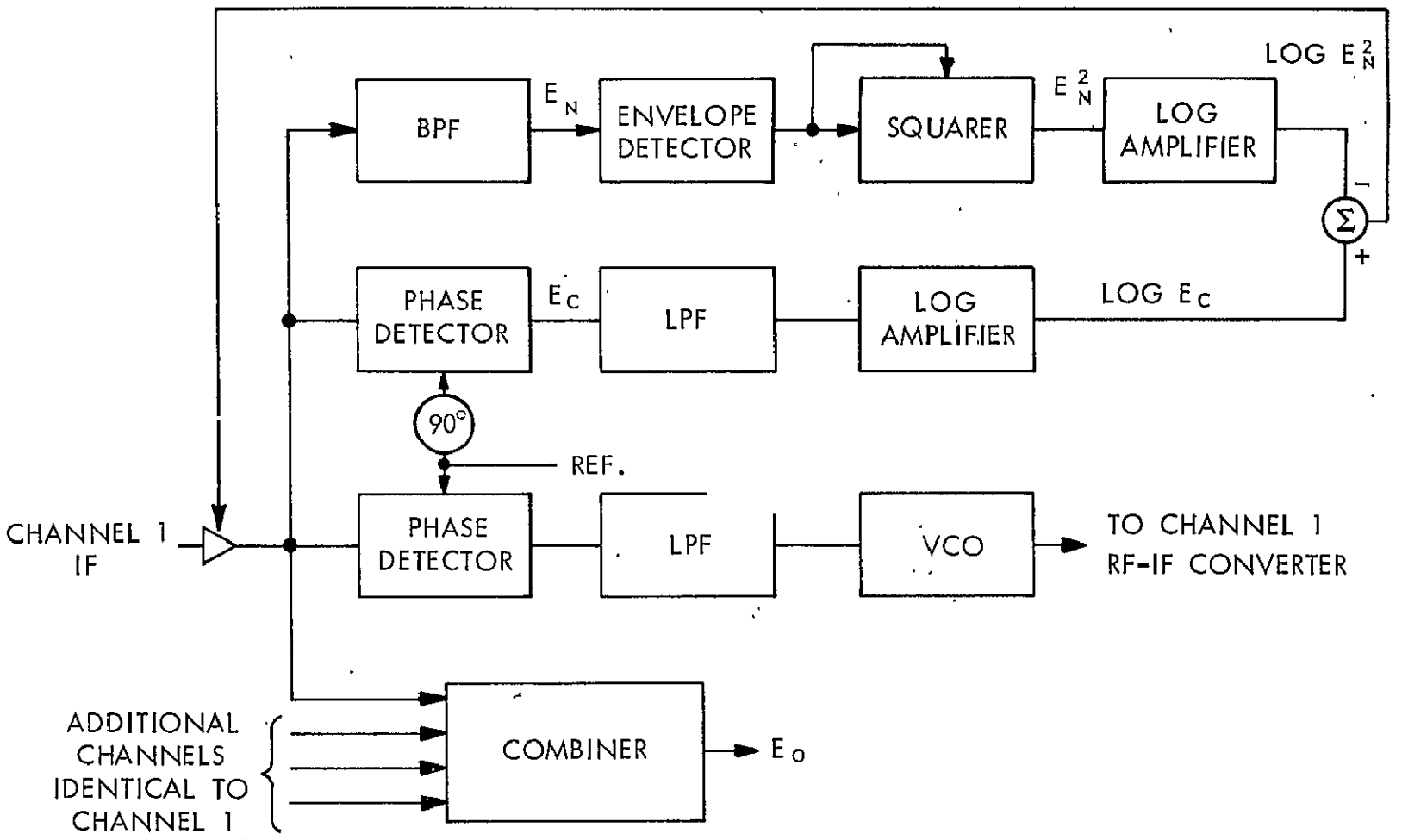

Figure 2-5: Maximal Ratio Weighting Using Out of Band Noise Detectors

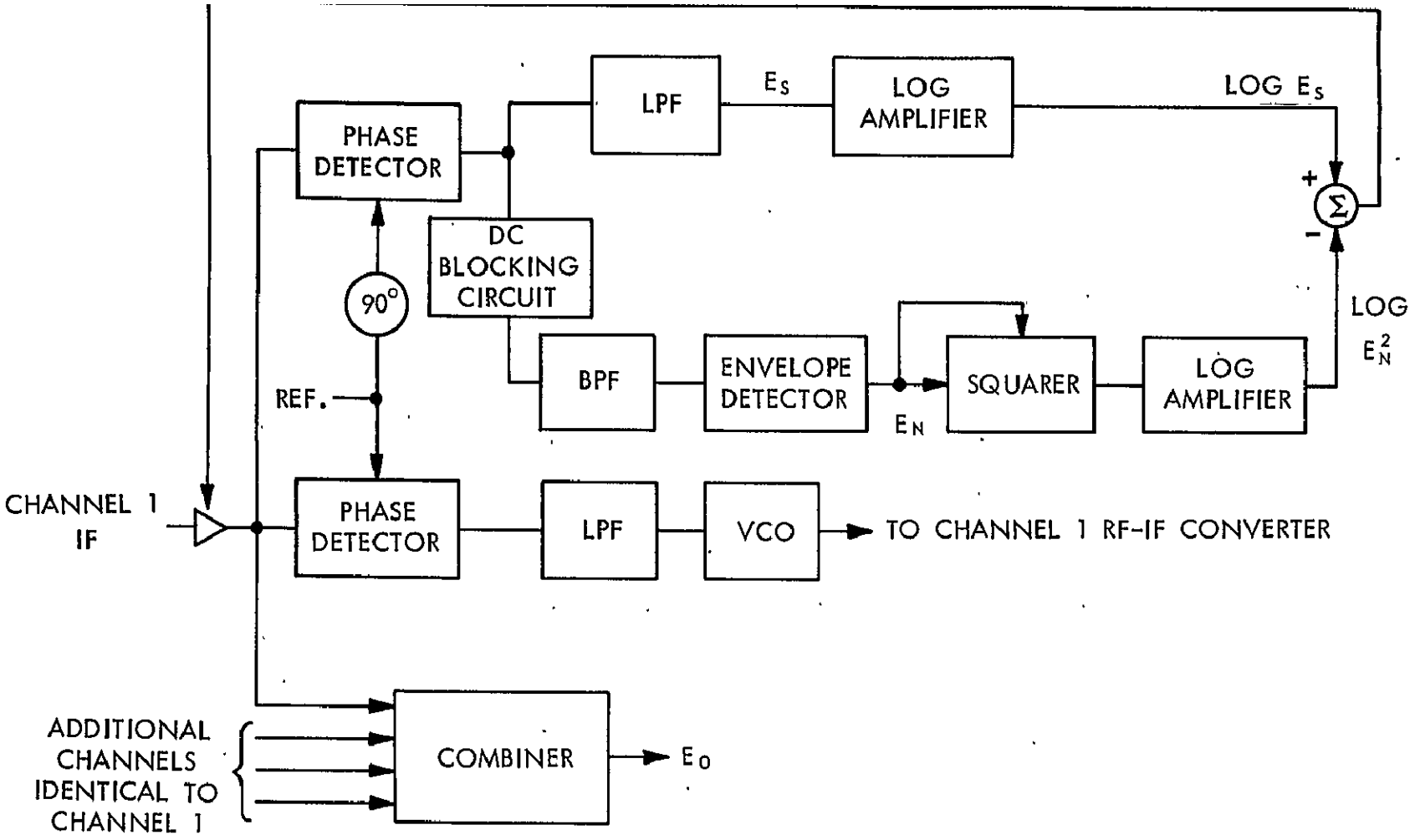

Figure 2-6: Maximal Ratio Weighting Using Correlation Detector Output

2.2.3c Non Coherent AGC

A simpler method of achieving maximal ratio weighting involves the use of a noncoherent AGC loop to maintain the C+N constant prior to coherent detection of the carrier. The dotted lines in Figure 2-7 enclose the noncoherent AGC loop for each input channel of a two element array. The carrier level out of the noncoherent AGC loop (point A in Figure 2-7) will be related to input CNR as in Figure 2-8. If the CNR is below -10 dbm, the CNR can be determined to within 0.5 db by measuring the output carrier level only. The output carrier level is defined by the coherent AGC of the receiver. The weighting operation is then performed on the basis of coherently detected carrier level only (which is linearly related to CNR) and, with the exception of the additional noncoherent AGC loops, the receiver is identical to that for AGC weighting (Section 2.2.4). Within its operational range, this circuit provides weighting on the basis of CNR, an approximation to ratio squared weighting.

In order to extend the capability of this technique to higher CNR levels, the noncoherent AGC loop is used prior to the IF bandpass filter and makes use of a wider RF bandwidth to reduce the CNR. To increase the range of the technique for IF CNRs of up to +10 db, the bandwidth of the noncoherent loop filter (F_1 in Figure 2-7) must be 100 times greater that of the IF filter. This patented technique [8] has been successfully used by NASA in polarization diversity receiver systems for many years.

2.2.3d Bandpass Limiter

Direct noise measurements can be avoided entirely while still providing ratio squared weighting. The procedure is based upon the characteristics of hard limiters [9] to maintain a linear relation between input carrier to noise ratio and output carrier to noise ratio for input CNRs less than -5 db (Figure 2-9). Since the receiver must phase adjust each channel to insure coherent signal summation (Section 2.1), there will be a reference signal available which is coherent with the received carrier. This reference signal, which provides coherent AGC detection at IF, can similarly provide coherent detection of the output carrier from the limiter (Figure 2-10). The detected carrier level out of the limiter C' will vary with input CNR to the limiter as shown in Figure 2-11. Note that if the input CNR is -5 db or less, the coherently detected carrier (C') is linearly related to IF CNR within 0.5 db. Therefore, by selecting the bandpass filter prior to the limiter to be 1 MHz for a 30 kHz IF BW, the detected carrier output will fall within the linear region for IF CNRs of 10 db or less.

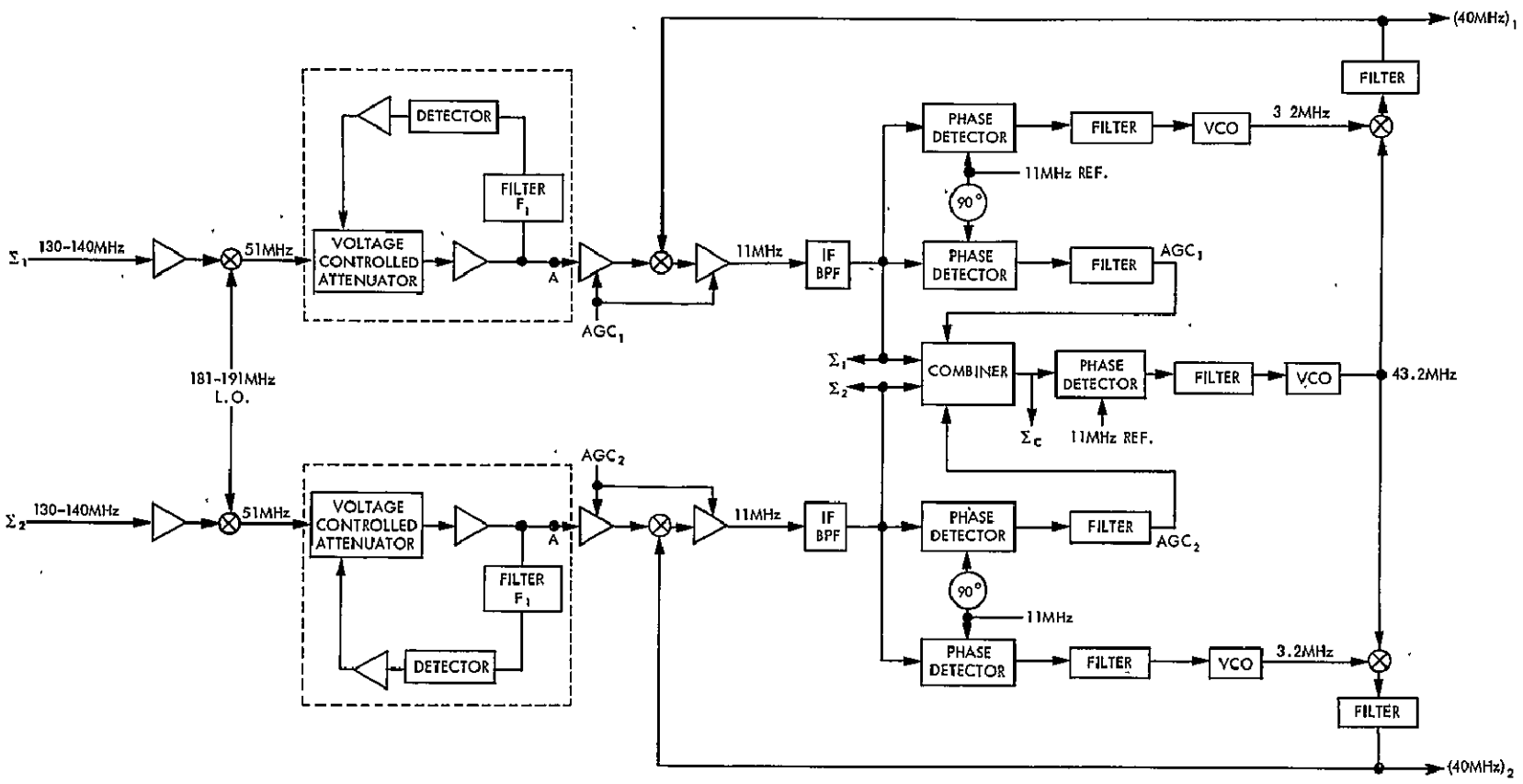

Figure 2-7: Block Diagram of Coherent Receiver with Non Coherent AGC Loops

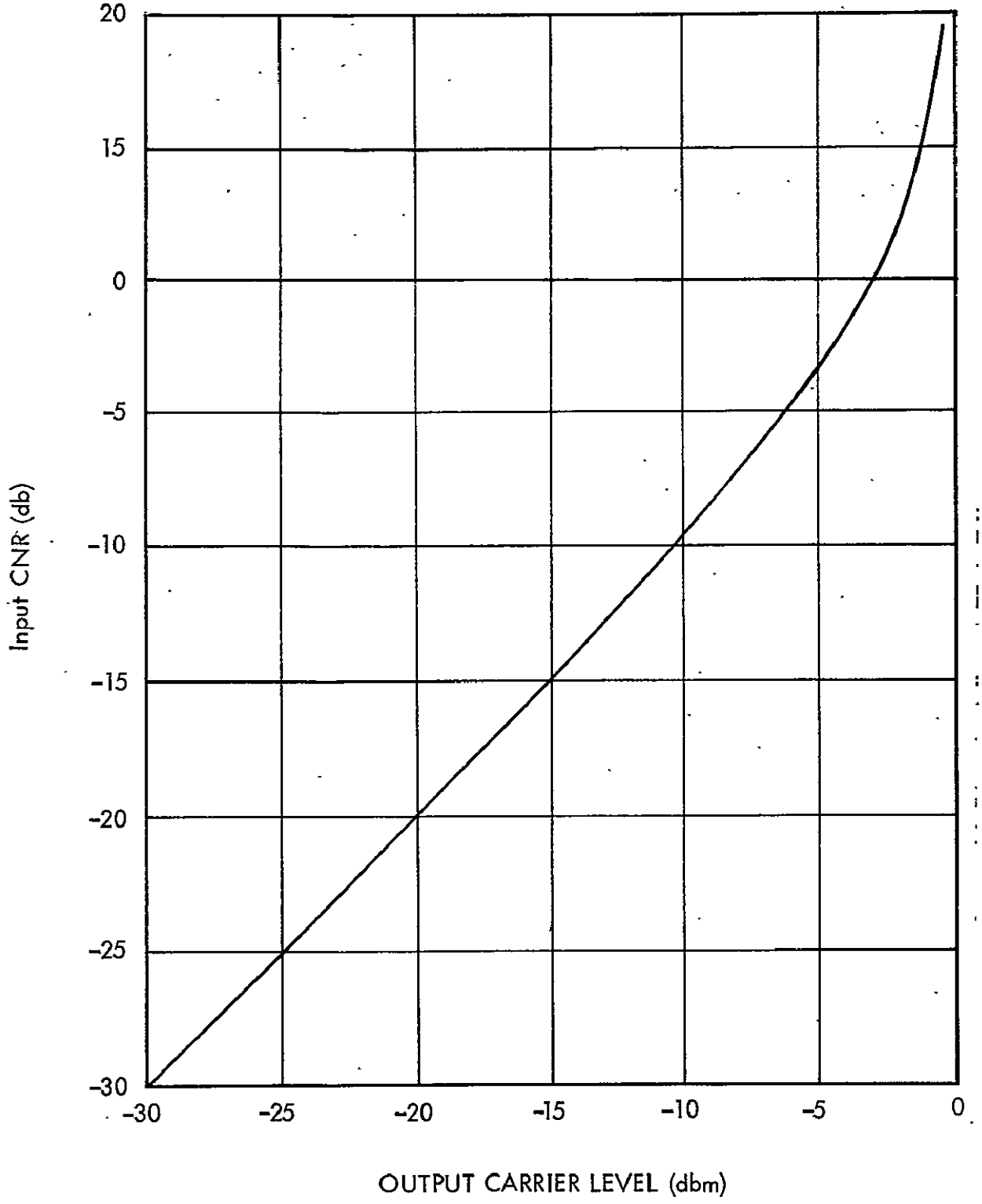

Figure 2-8: Output from a Non Coherent AGC with 0 dbm Output C+N

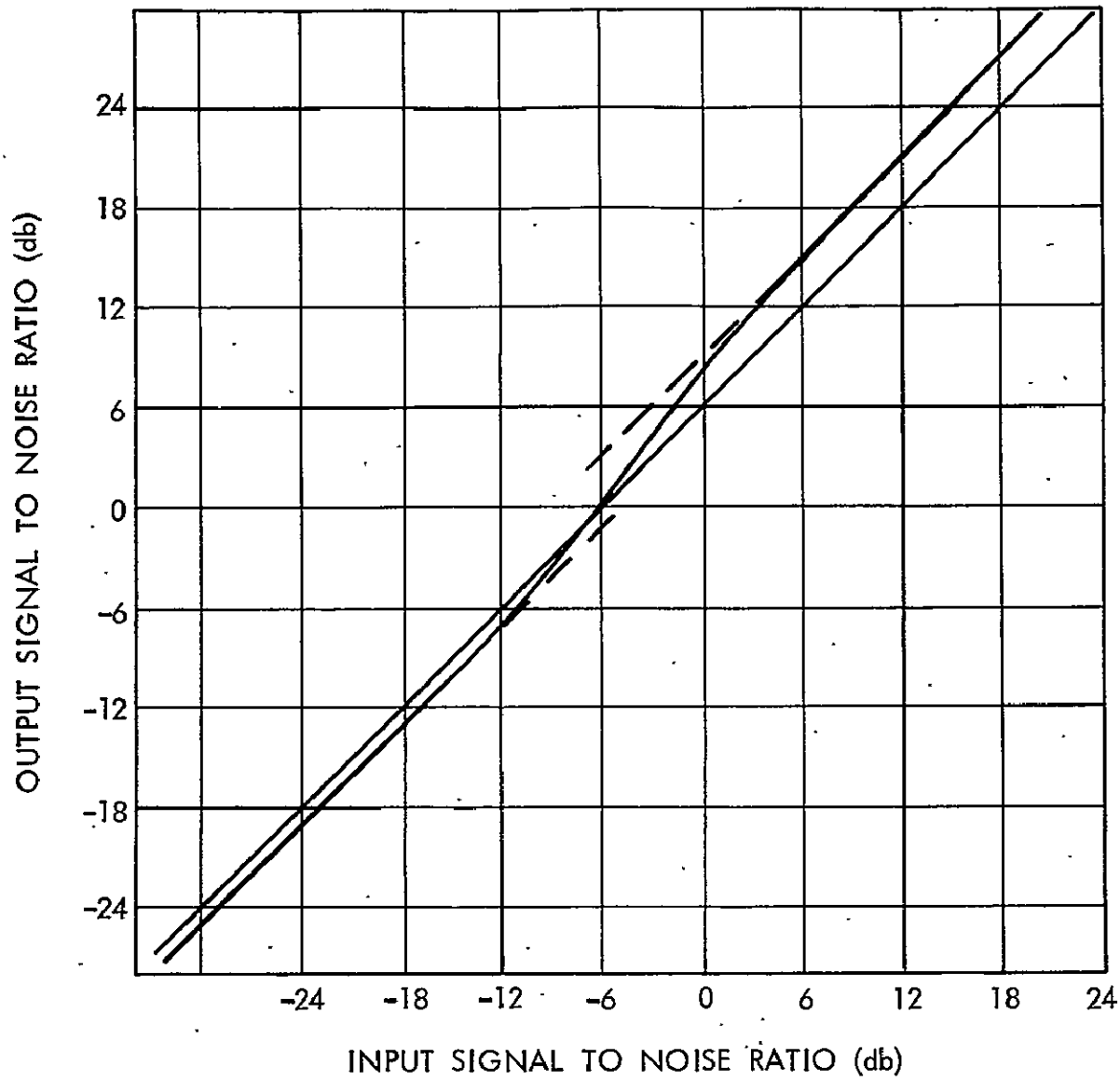

Figure 2-9: SNR Characteristics of a Bandpass Limiter

The coherently detected carrier level out of the limiter (C') is linearly related to CNR in the IF of the receiver. The ratio squared weighting coefficient can be determined by dividing the square of the detected carrier output of the limiter $\left(\frac{C^2}{N^2}\right)$ by the carrier level only (AGC). A block diagram of one channel of a phase lock receiver incorporating such a weighting scheme is shown in Figure 2-10.

The primary disadvantage of this weighting technique is that it requires a wide noise bandwidth to reduce the CNR of the input to the limiter.

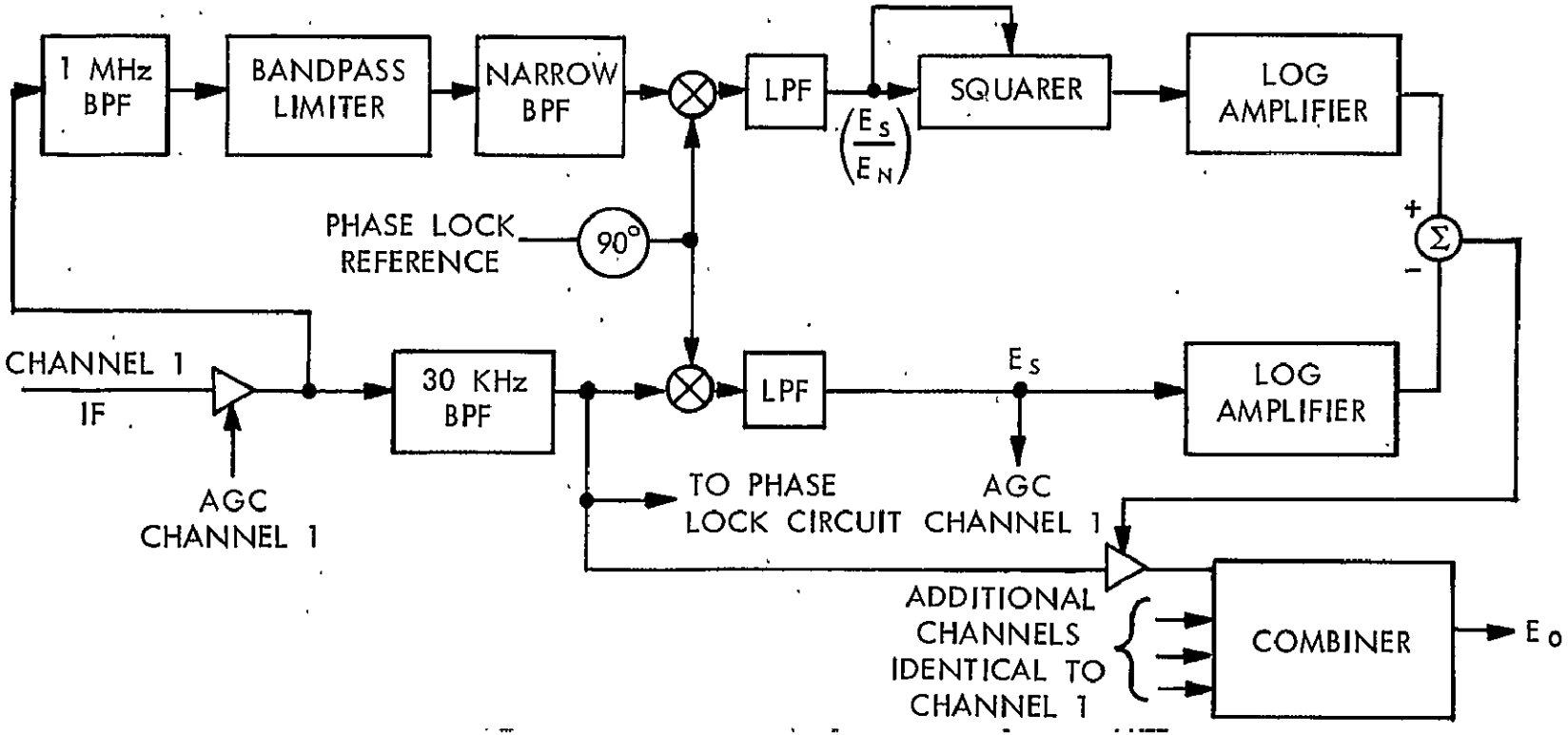

Figure 2-10: Maximal Ratio Weighting Circuit Using Bandpass Limiter

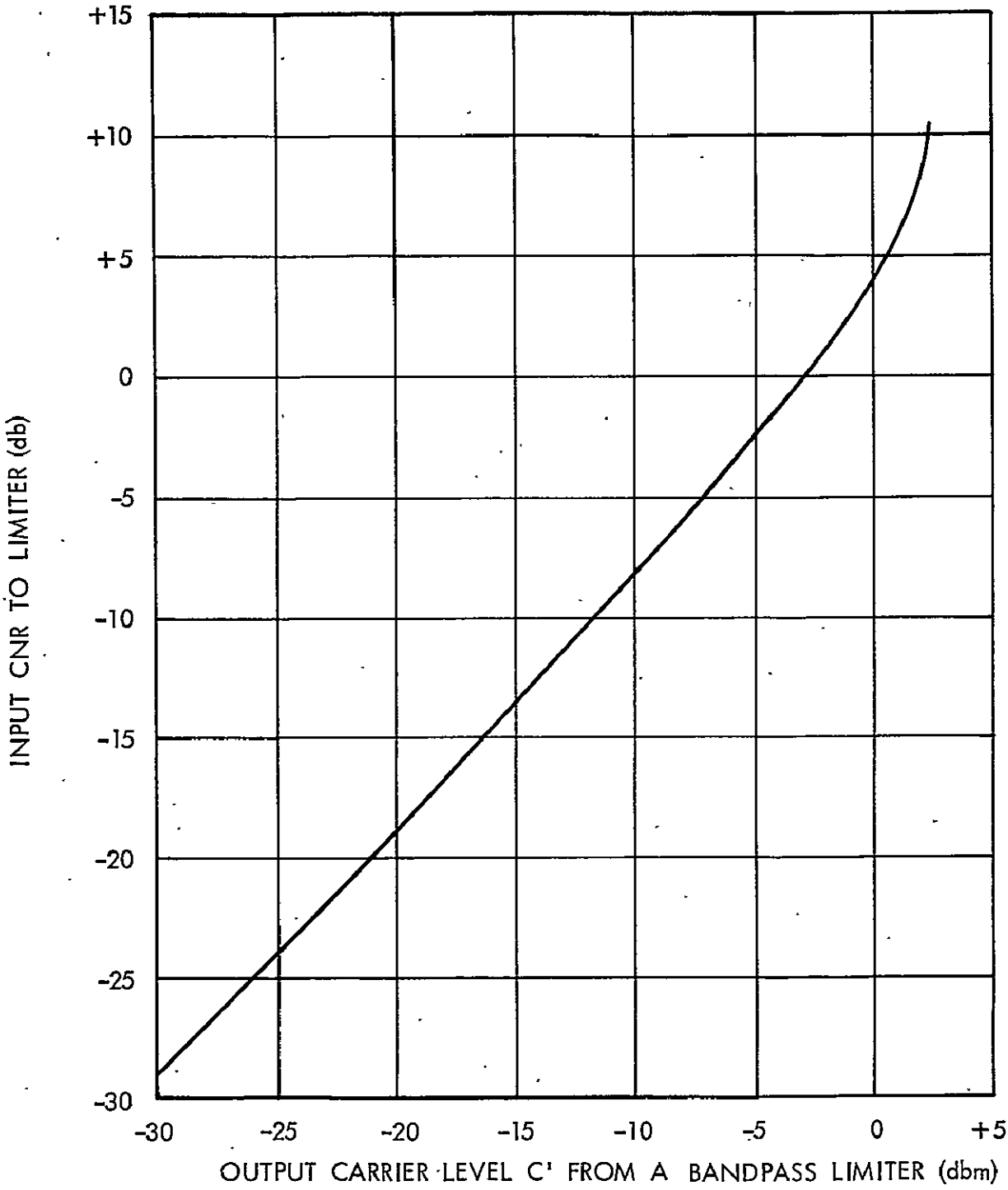

Figure 2-11: Output Carrier Level (C') vs. Input CNR for a Bandpass Limiter

Although this process has no effect on the IF information supplied to the combiner, it does increase the possibility of interference affecting the measurement of C'. For an array of identical antennas, the effect of strong equal interference in all array channels will be to raise the apparent noise level in each channel. At worst, the effect will be to reduce the performance of the circuit to that of an AGC weighting receiver (to be discussed in Section 2.2.4).

When the interference levels are not equal in each antenna, degradation in performance will occur. The amount of degradation depends on both the IF CNR and on the relative magnitude of total interference to desired carrier. Figures 2-12 through 2-15 indicate the maximum CNR

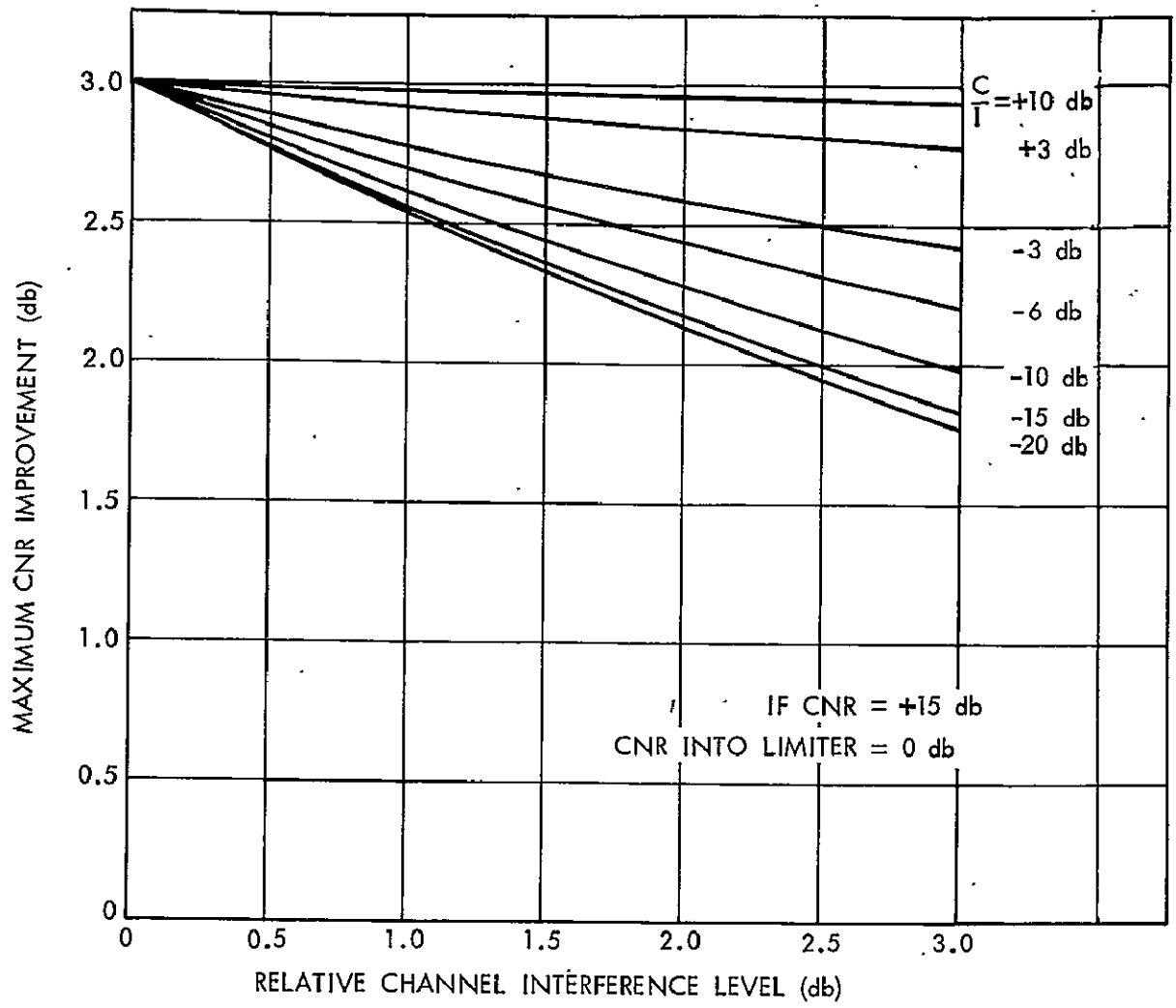

Figure 2-12: Effects of Interference, $\left(\frac{C}{N}\right)_{IF} = +15$ db

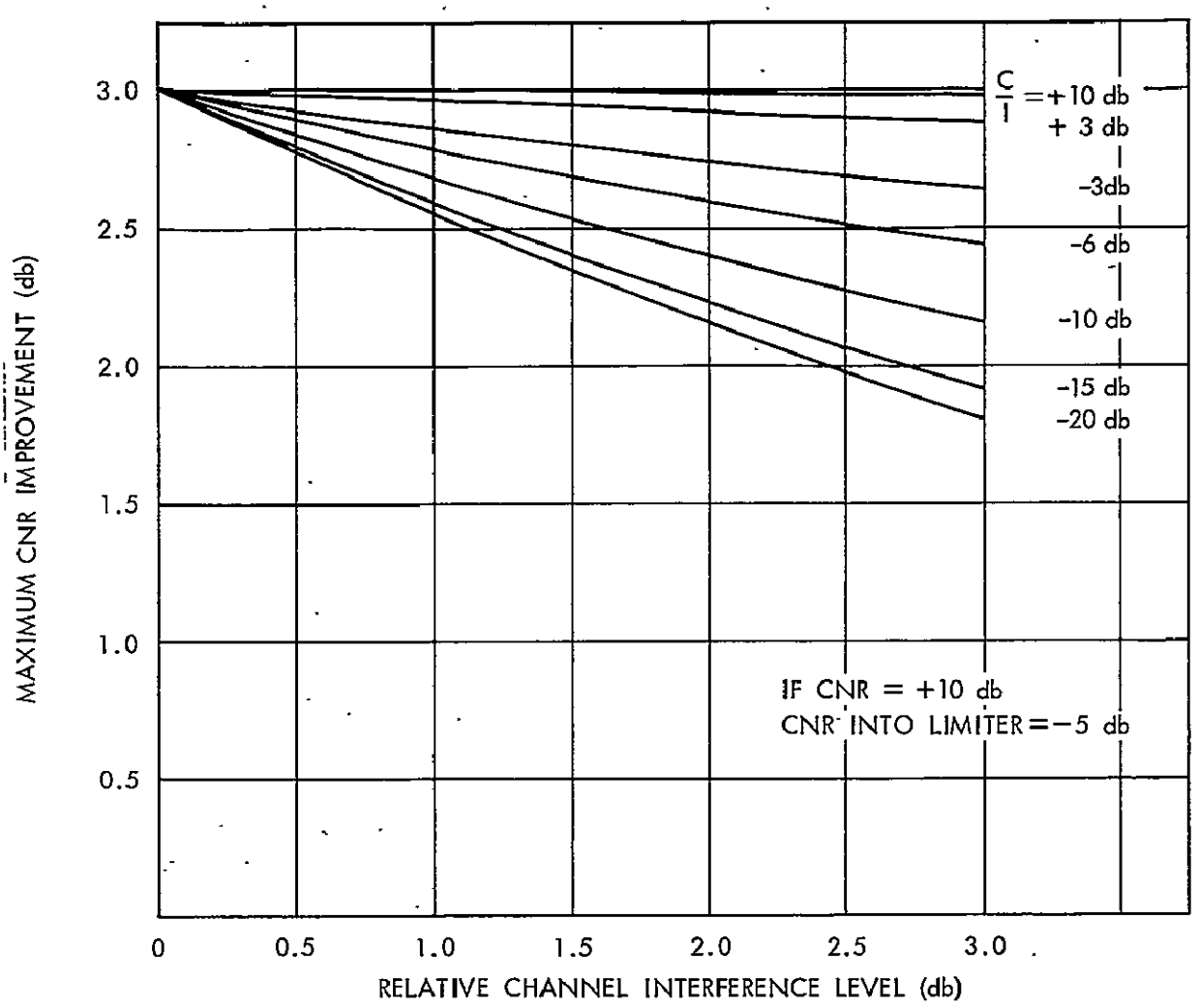

Figure 2-13: Effects of Interference, $\left(\frac{C}{N}\right)_{IF}$ = +10 db

improvement from a two element array as a function of interference conditions. In most cases the difference in interference received by the antennas will be less than 2 db. Under the condition of +15 db IF CNR in each input channel, the total interference to desired carrier ratio (I/C) in the limiter bandwidth would need to be +5 db or greater to result in a 0.5 db loss in the combined output. Note that the +15 db IF CNR condition is high enough so that the improvement is not critical. Under low IF CNR conditions (Figure 2-15), the required I/C would be greater than +15 db for a 0.5 db reduction in combined output (a ΔI of 2 db was assumed as before). The circuit performance under interference improves as the IF CNR decreases. This technique is not affected by the type of modulation received provided a carrier or pilot signal is available for phase lock and coherent detection.

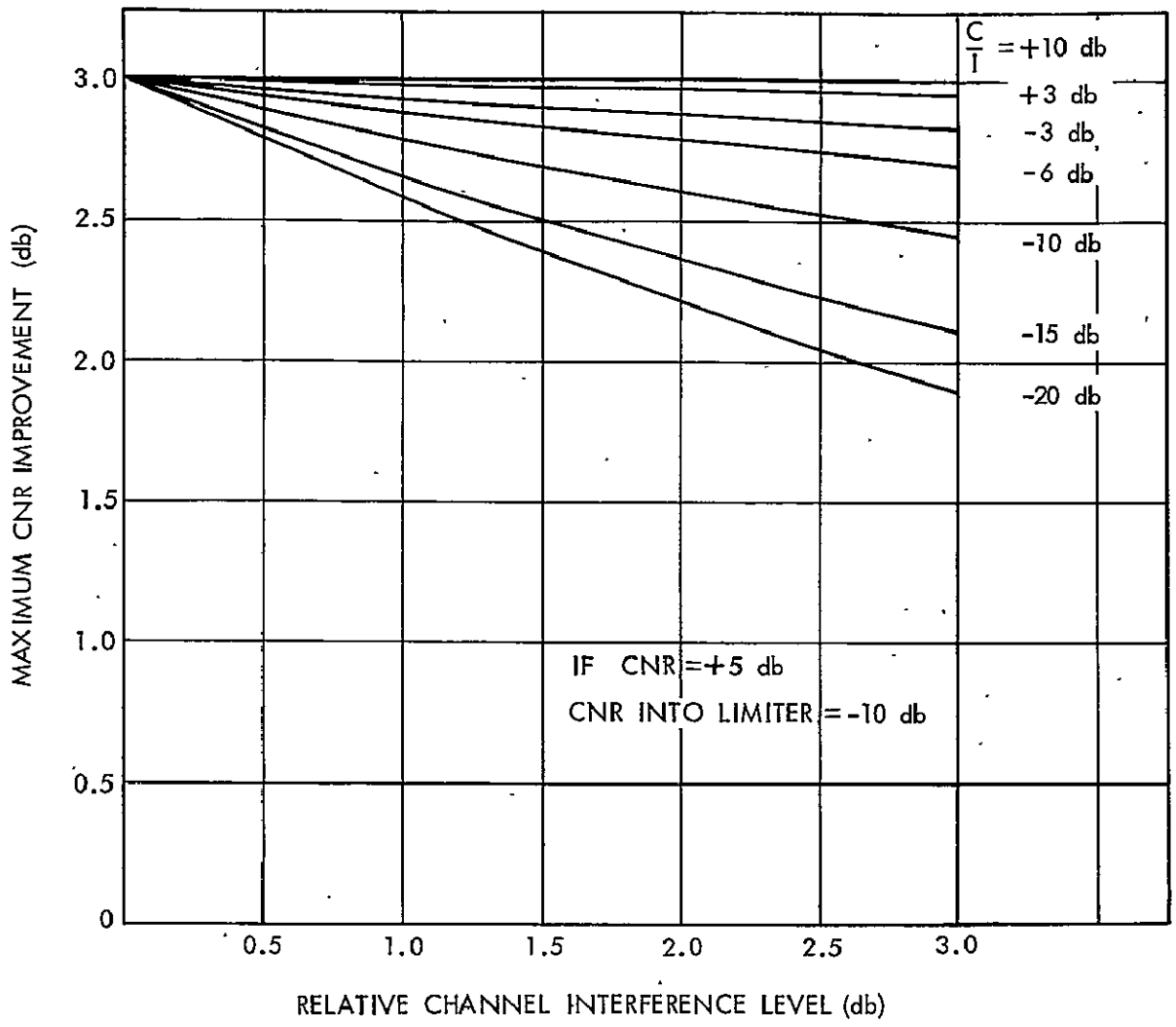

Figure 2-14: Effects of Interference, $\left(\frac{C}{N}\right)_{IF} = +5$ db

The selection of a method for achieving maximal ratio weighting will depend on antenna beamwidth, number of potential interference sources (their frequency and location) and modulation. Irrespective of the method chosen, an effective ratio squared weighting scheme will be superior to either selection or equal gain weighting. Figure 2-16 illustrates the CNR required in each channel of a two element array for equal gain, selection and ratio squared weighting for a combined output of $\left(\frac{C_o}{N_o}\right)^2 = \rho$. At best, equal gain and selection diversity are equivalent to ratio squared weighting under certain conditions. These conditions consist of identical CNRs in

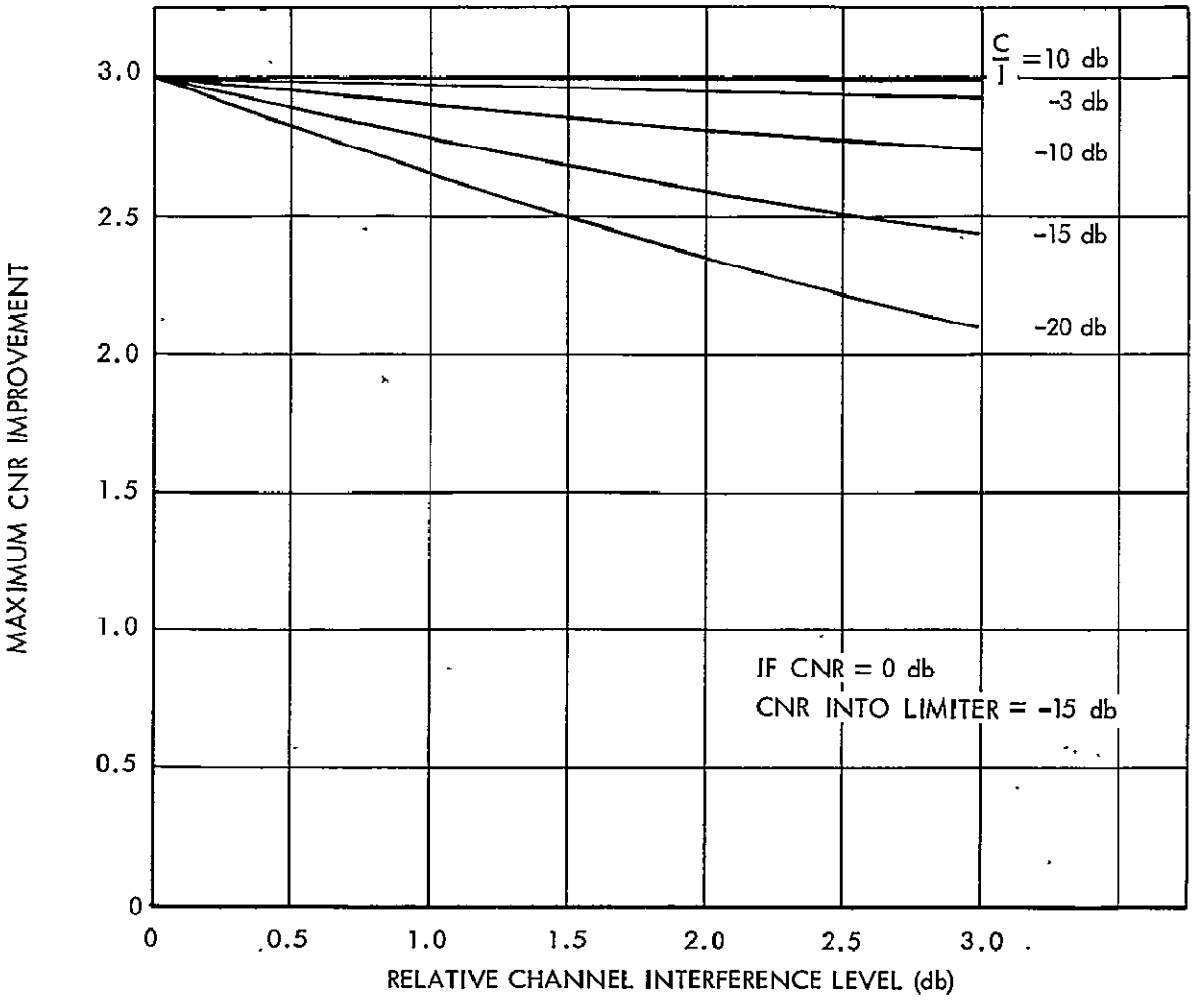

Figure 2-15: Effects of Interference, $\left(\frac{C}{N}\right)_{IF} = 0$ db

each input channel for equal gain diversity and complete fading in one of the input channels for selection diversity.

2.2.4 Coherent AGC Weighting

Although weighting the channels of an array directly as the carrier voltage and inversely as the noise power provides optimum performance, approximate weighting techniques are often used in practice. If the assumption is made that the noise levels in each channel are essentially equivalent, the weighting process can be greatly simplified. Only the carrier levels need be used in the weighting process. The coherently detected AGCs of the receiver provides the required measure of carrier

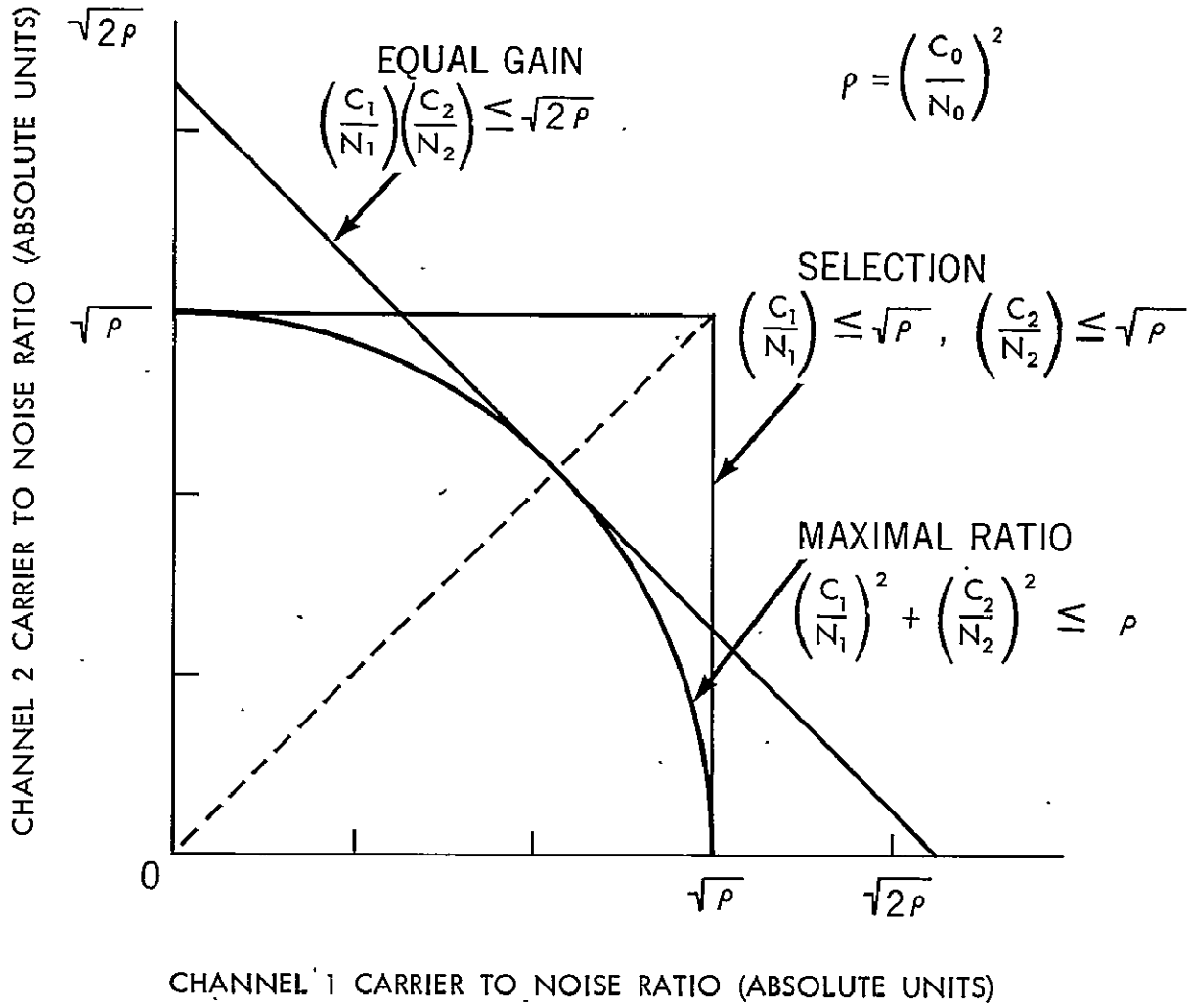

Figure 2-16: Comparison of Performance for Equal Gain, Selection and Maximal Ratio Diversity Weighting Techniques (Reference 10)

levels. Figure 2-3 shows a block diagram of the Advanced Polarization Diversity Autotrack Receiver (APDAR) which performs AGC weighting on the input channels [3].

Since AGC weighting is an approximation to ratio squared weighting, it must be evaluated to determine the effect of unequal noise and unequal channel gain. The simplified system block diagram in Figure 2-17 shows the components affecting the weighting process. The preamplifier in the figure is broken into noise figure and gain sections. The gain figures of G_1 and G_2 represent net gain from the input of the preamplifier to the input of the receiver and therefore include cable losses. The noise figure

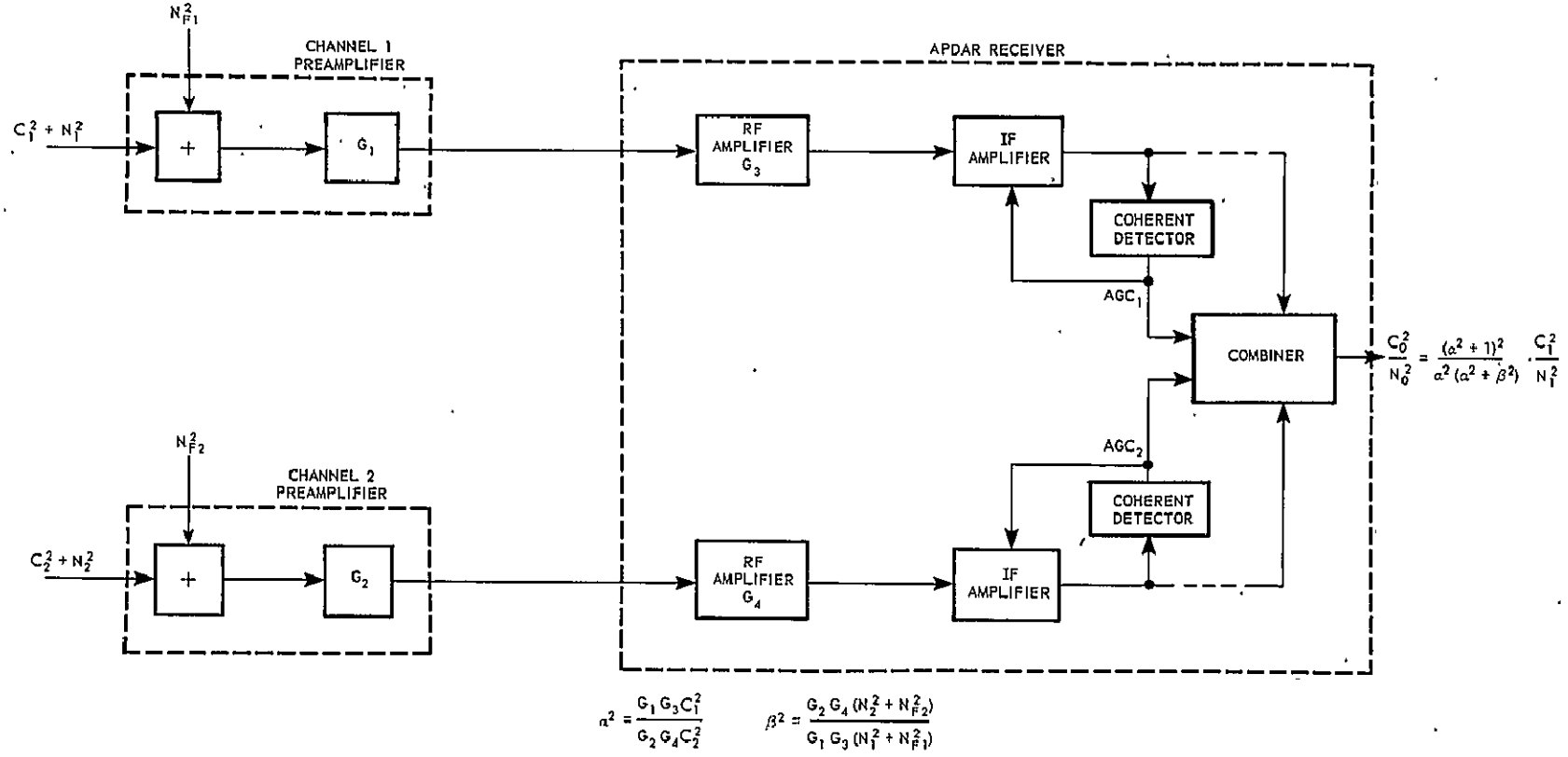

Figure 2-17: System Model for Studying APDAR AGC Weighting Process

contributions shown represent the noise figures of each channel referred to the input of the preamplifier.

The APDAR receiver is divided into three stages: RF amplifier section, IF amplifier section, and combiner section. The RF amplifiers have constant gain characteristics which are adjustable. The IF amplifiers are actively gain controlled by the AGC outputs of the coherent detectors. The output carrier levels from the IF amplifiers are thereby maintained constant. The automatic gain control signal therefore represents a measure of the output carrier from the RF amplifiers. The combiner in turn accepts the AGC output as proportional to the carrier level into the preamplifiers for that channel. This process is correct to within the channel gain differences of the system prior to the IF amplifiers. The total carrier and noise power arriving at the IF amplifiers is given by

$$G_1 G_3 \left(C_1^2 + N_1^2 + N_{F1}^2 \right) \tag{8}$$

for channel 1, and by

$$G_2 G_4 \left(C_2^2 + N_2^2 + N_{F2}^2 \right) \tag{9}$$

for channel 2. The gain products in each channel must be identical for the combiner to weight the signals properly.

The combiner assumes that the AGC or C level is a linear function of the CNR in a given channel. Equations (8) and (9) indicate that the assumption will be in error by the difference in received noise levels N_1 and N_2 and also by the difference in channel noise figure contributions N_{F1} and N_{F2}. The input noise levels are unpredictable and will depend on contributions from numerous sources.

Unequal channel gain products given in Equations (8) and (9) will also lead to inaccurate weighting. However, compensation for gain differences in the preamplifiers (G_1 and G_2) can be made by adjusting the gain of the RF amplifiers (G_3 and G_4) of the receiver. The influence of these parameters on overall system performance can be expressed in mathematical form. Assuming for this analysis that the combiner weights channel 1 in relation to channel 2, the expressions can be written

$$C_o^2 = k\,(\alpha C_1 + C_2)^2 \tag{10}$$

$$N_o^2 = k\left[\alpha^2\left(N_1^2 + N_{F1}^2\right) + N_2^2 + N_{F2}^2\right] \tag{11}$$

where C_o^2 and N_o^2 represent the output carrier and noise levels from the combiner with k a constant of channel 2. The factor α^2 is given by

$$\alpha^2 = \frac{G_1 G_3 C_1^2}{G_2 G_4 C_2^2}$$

and contains the relative gain products of the two channels. Equations (10) and (11) can then be written in terms of channel 1 carrier and noise only

$$C_o^2 = C_1^2\left(\alpha + \frac{1}{\alpha}\right)^2 = C_1^2\left(\frac{\alpha^2 + 1}{\alpha}\right)^2$$

$$N_o^2 = \left(N_1^2 + N_{F1}^2\right)(\alpha^2 + \beta^2)$$

where

$$\beta^2 = \frac{G_2 G_4\left(N_2^2 + N_{F2}^2\right)}{G_1 G_3\left(N_1^2 + N_{F1}^2\right)}$$

The output carrier to noise ratio can now be expressed in terms of the input CNR of channel 1 by

$$\frac{C_o^2}{N_o^2} = \frac{(\alpha^2 + 1)^2}{\alpha^2(\alpha^2 + \beta^2)} \cdot \frac{C_1^2}{N_1^2}$$

If both the noise characteristics and the gain characteristics of each channel are identical with

$$N_2^2 + N_{F2}^2 = N_1^2 + N_{F1}^2 \quad (12)$$

and

$$G_1 G_3 = G_2 G_4 \quad (13)$$

the CNR improvement at the combiner output over that of the best input channel is given in Figure 2-18. Under these conditions, an AGC weighting receiver performs identically to that of an ideal ratio squared weighting system. However, when either Equation (12) or Equation (13) is not true, the CNR improvement will fall below that for an ideal ratio squared system. Figure 2-19 indicates the effect of differences in noise characteristics and Figure 2-20 indicates the effect of differences in gain for a two element array. In each figure, the curves represent maximum possible CNR improvement based upon the conditions specified. A summary of the contribution to combined output CNR reduction from each major system parameter is given in Figure 2-21. Each curve represents the maximum CNR improvement for a given channel ratio of one system parameter, with each of the other two parameter ratios equal to 1.

The differential gain effects are eliminated by properly compensating for these in the RF amplifier stage of the receiver. The channel noise figure differences can be minimized by carefully matching the preamplifier noise figures used in each channel. The effect of differential noise reception, however, cannot be eliminated in an AGC weighted system and these will contribute to a reduction in CNR improvement. If the conditions under which the antenna system is to operate are such as to make the probability of such differential noise reception small, then AGC weighting offers a simplified approach to achieving near-optimum performance.

2.3 Time Delay

The receiver requirements of coherence and channel weighting are sufficient for an array of closely spaced elements. However, the coherence operation is modulo 2π radians at the carrier frequency and is incapable of correcting for phase differences greater than one wavelength of the carrier. With equal length transmission lines connecting each array element to the receiver, phase differences greater than one carrier wavelength will occur primarily as a result of time of arrival delay between reception at the array elements. Figure 2-22 indicates those factors that contribute to time of arrival delay.

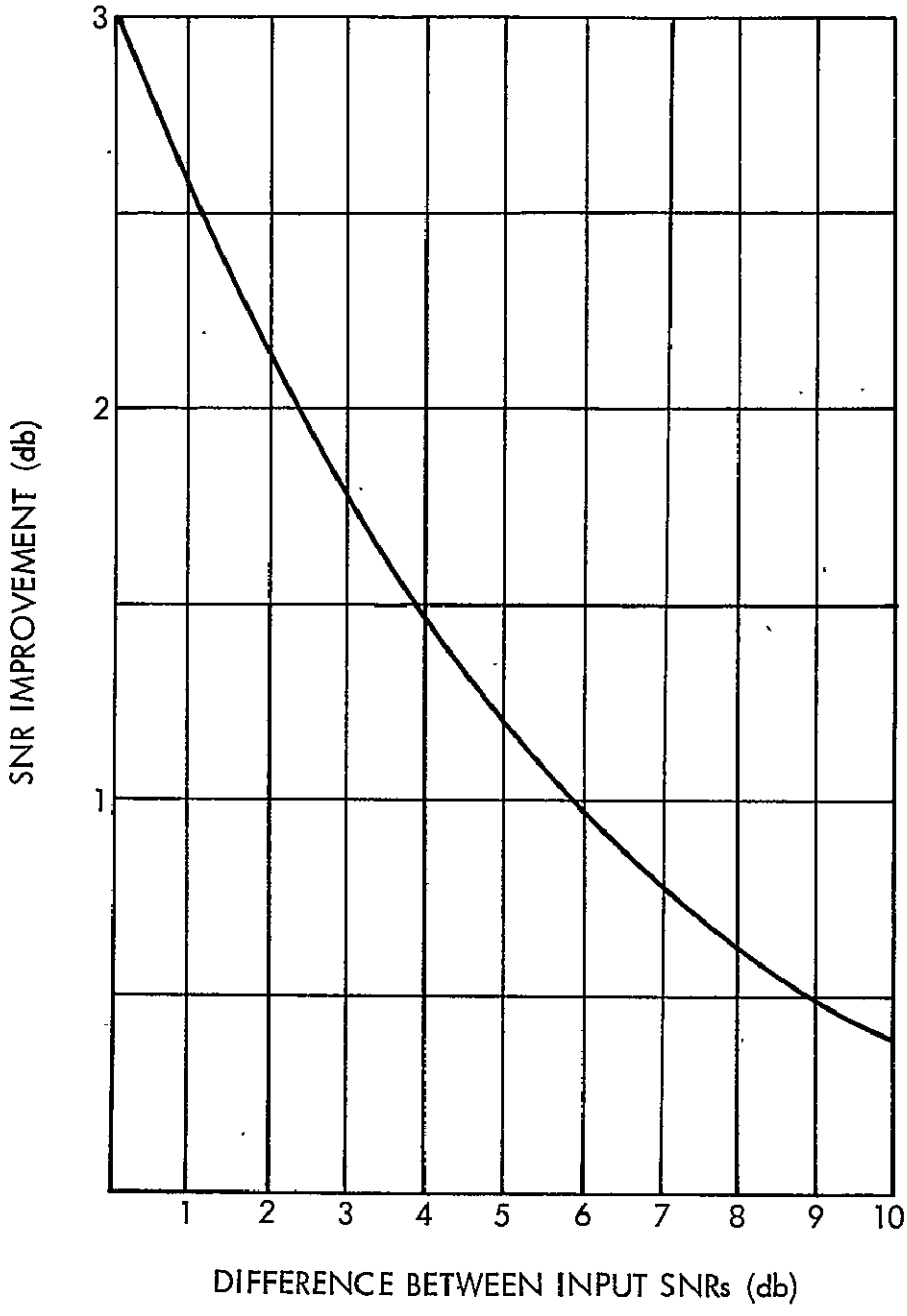

Figure 2-18: Maximum Theoretical SNR Improvement vs. Input Conditions

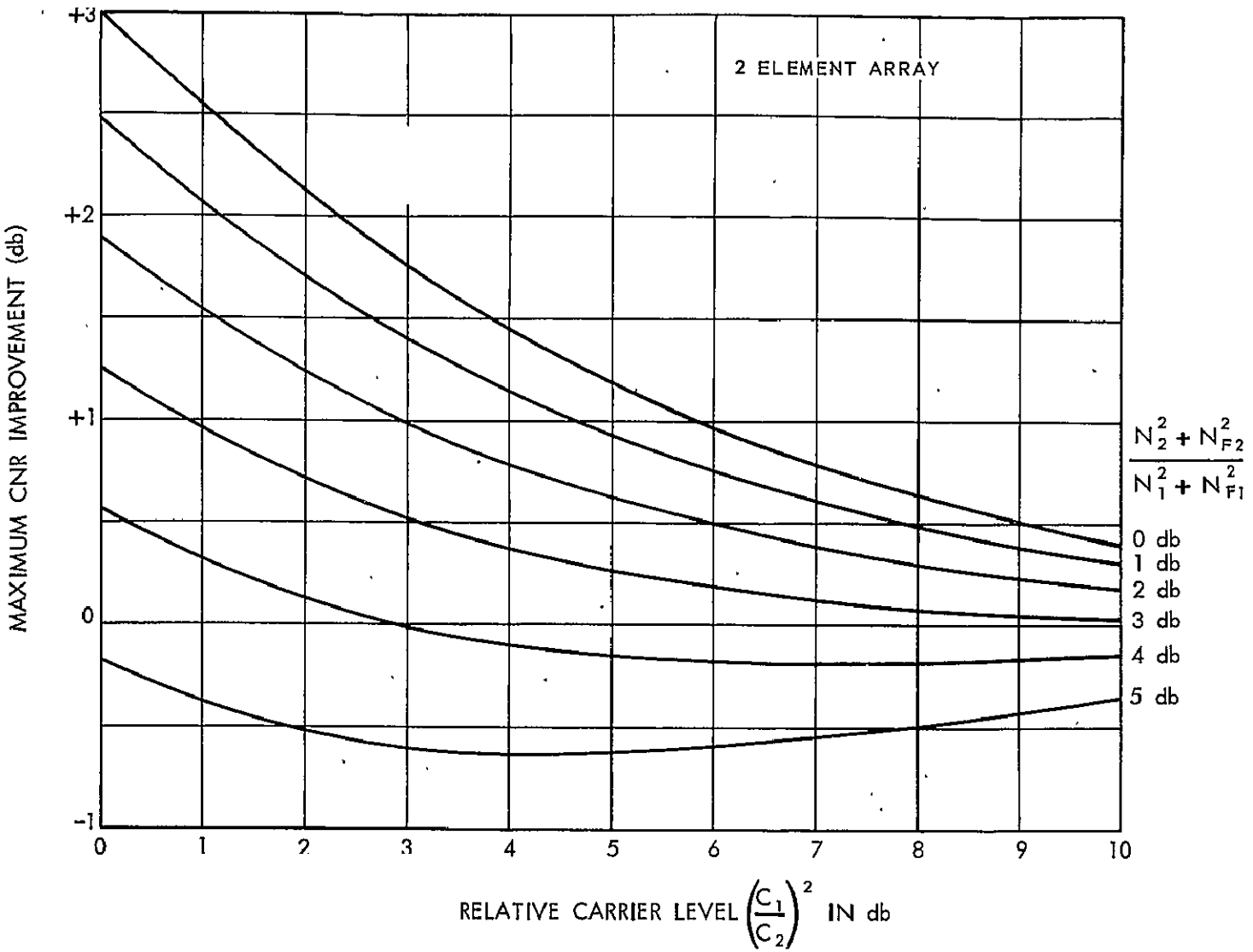

Figure 2-19: CNR Improvement vs. Relative Carrier Levels for Several Channel Noise Conditions

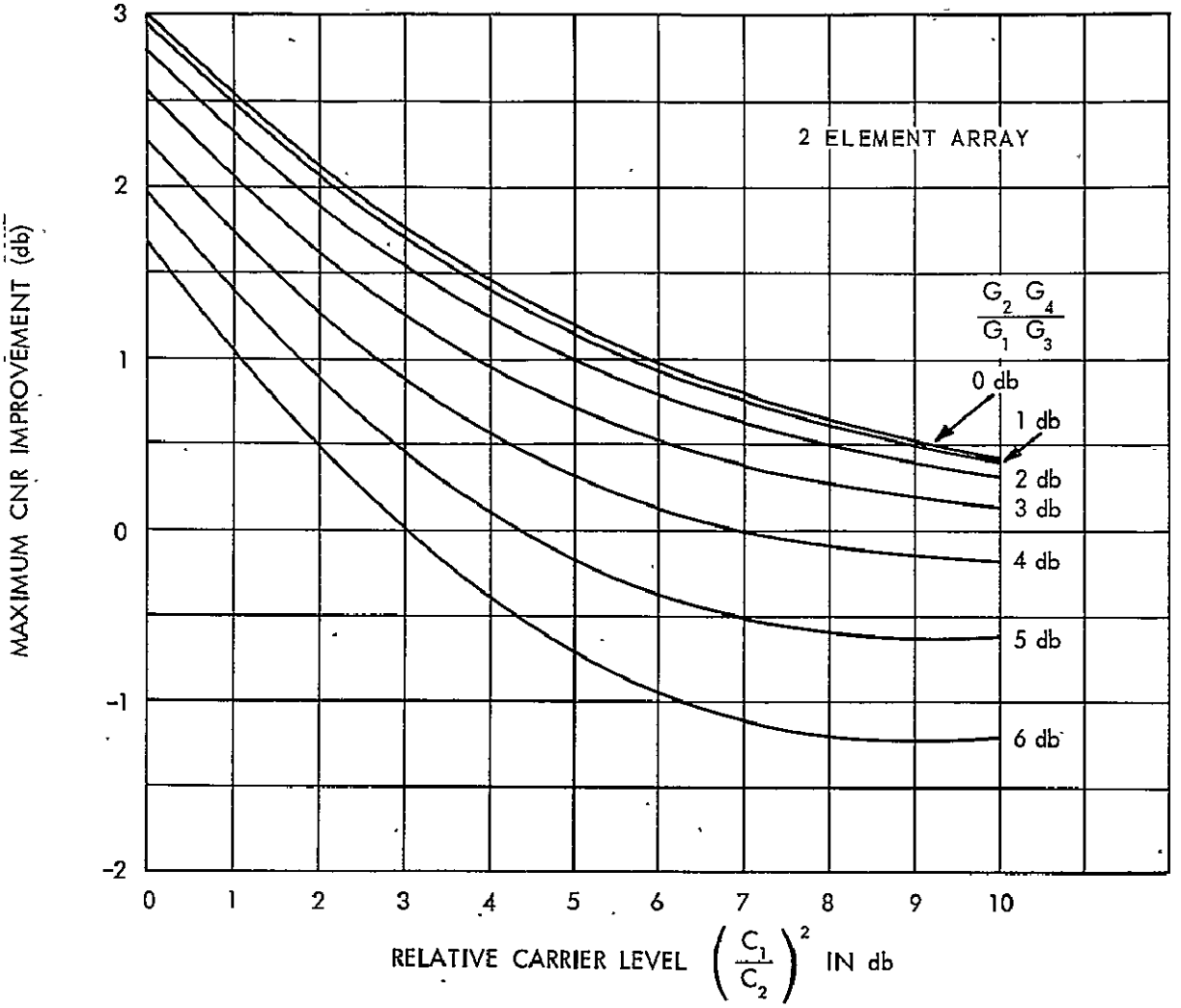

Figure 2-20: CNR Improvement vs. Relative Carrier Levels for Several Channel Gain Conditions

The existence of time of arrival delay has no effect on CW modulated signals: When the received signals have a finite bandwidth, the combining process will degrade the information on the carrier. This degradation is significant when the total time delay between elements becomes significant in comparison to a wavelength of the modulation frequency. Figure 2-23 indicates the maximum degradation of the combined output information (SNR) at band edge for a two element array at several antenna spacings. Considering time of arrival delay alone would indicate keeping the antennas as closely spaced as possible. Mutual shadowing of array elements [11] poses a limitation on the proximity of array elements. Figure 2-24 gives the minimum spacing between elements for a given sky coverage with all antennas mounted at identical elevation. Another

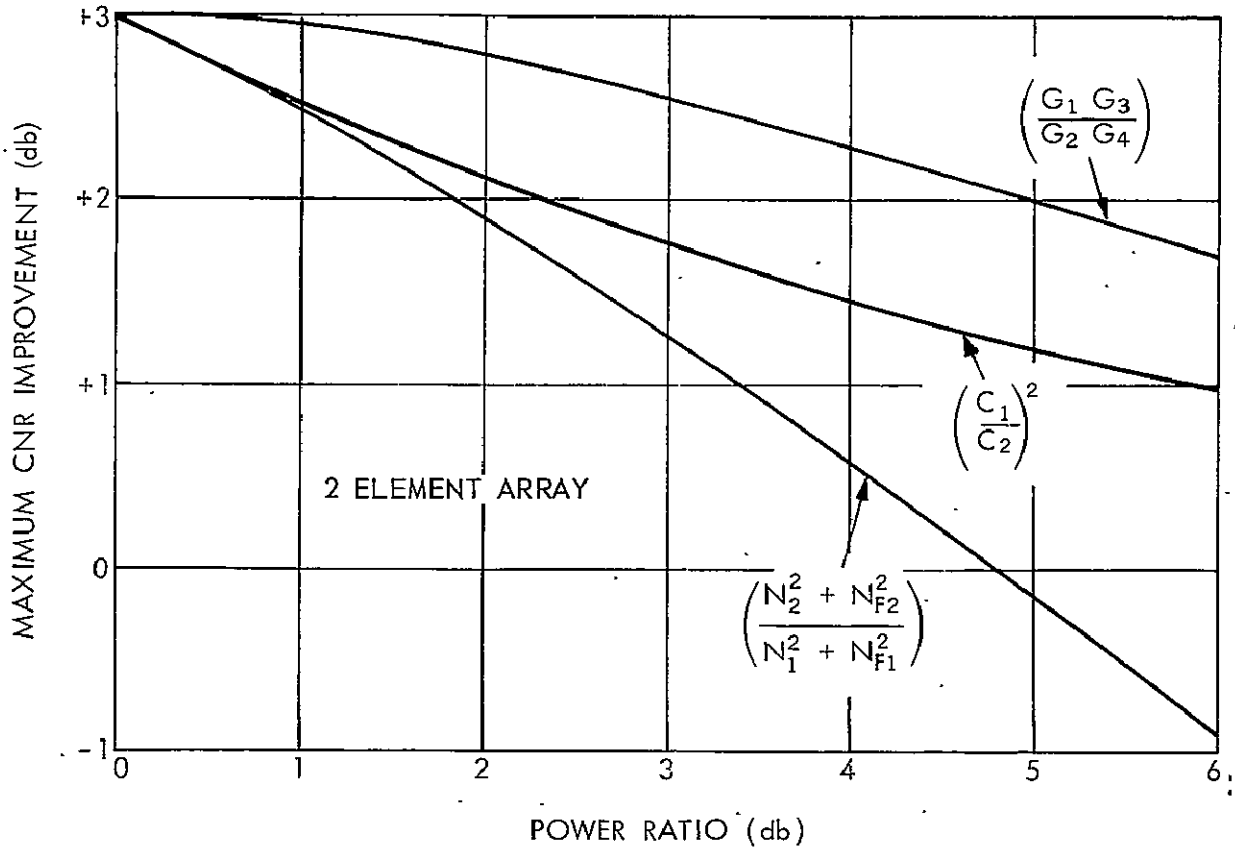

Figure 2-21: Maximum CNR Improvement vs. System Parameters for a Receiver with AGC Weighting

limitation on antenna proximity is spatially correlated fading due to Ionospheric turbulence. Experiments have indicated that, at VHF, antenna spacings of 1,000 feet or greater are required to minimize the effects of Ionospheric turbulence in Equatorial regions [12]. This requirement is independent of antenna diameter.

Since the primary objective of the array is to improve communication performance, a signal bandwidth sufficient to require the elimination of time of arrival delay can be expected. Research Triangle Institute introduced the idea of a digitally controlled time delay system to solve this problem but indicated uncertainty as to possible signal degradation resulting from switching transients [14]. In an effort to resolve the uncertainty, the experiment phase of this program included the development and evaluation of a digitally controlled time delay system.

Three techniques were considered for providing the required delay increments: active devices (such as transister amplifiers), transmission

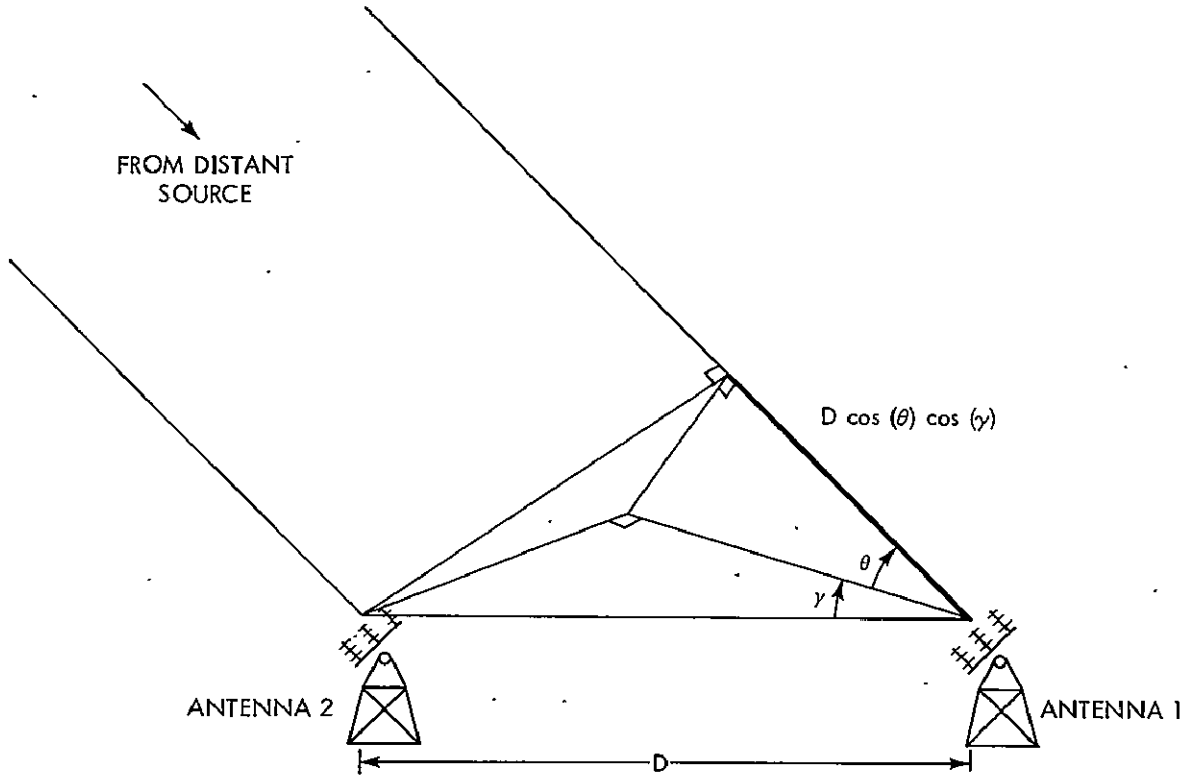

$$T = \frac{D}{C} \cos(\theta) \cos(\gamma) \text{ SECONDS}$$

γ = AZIMUTH ANGLE OF SOURCE REFERRED TO BASELINE
θ = ELEVATION ANGLE OF SOURCE
C = VELOCITY OF LIGHT
D = ANTENNA SEPARATION

Figure 2-22: Model for Determining Time of Arrival Delay

lines and lumped parameter networks. Active devices were not feasible because of the inherent size and power requirements as compared to lumped circuit networks. Transmission lines are feasible but are heavy and bulky. Lumped parameter networks, on the other hand, offer reasonable size and weight.

A breadboard model of 8 delay increments of the transmission line and lumped parameter network techniques was constructed and tested [13]. Each delay increment was approximately 90 n sec and the breadboard circuits therefore provided a total delay of 720 n sec. The time delay system was required to provide a 2 MHz flat top amplitude response centered at the APDAR IF frequency of 11 MHz. Both the transmission line and lumped parameter breadboard models had approximately 0.5 db gain ripple across the band.

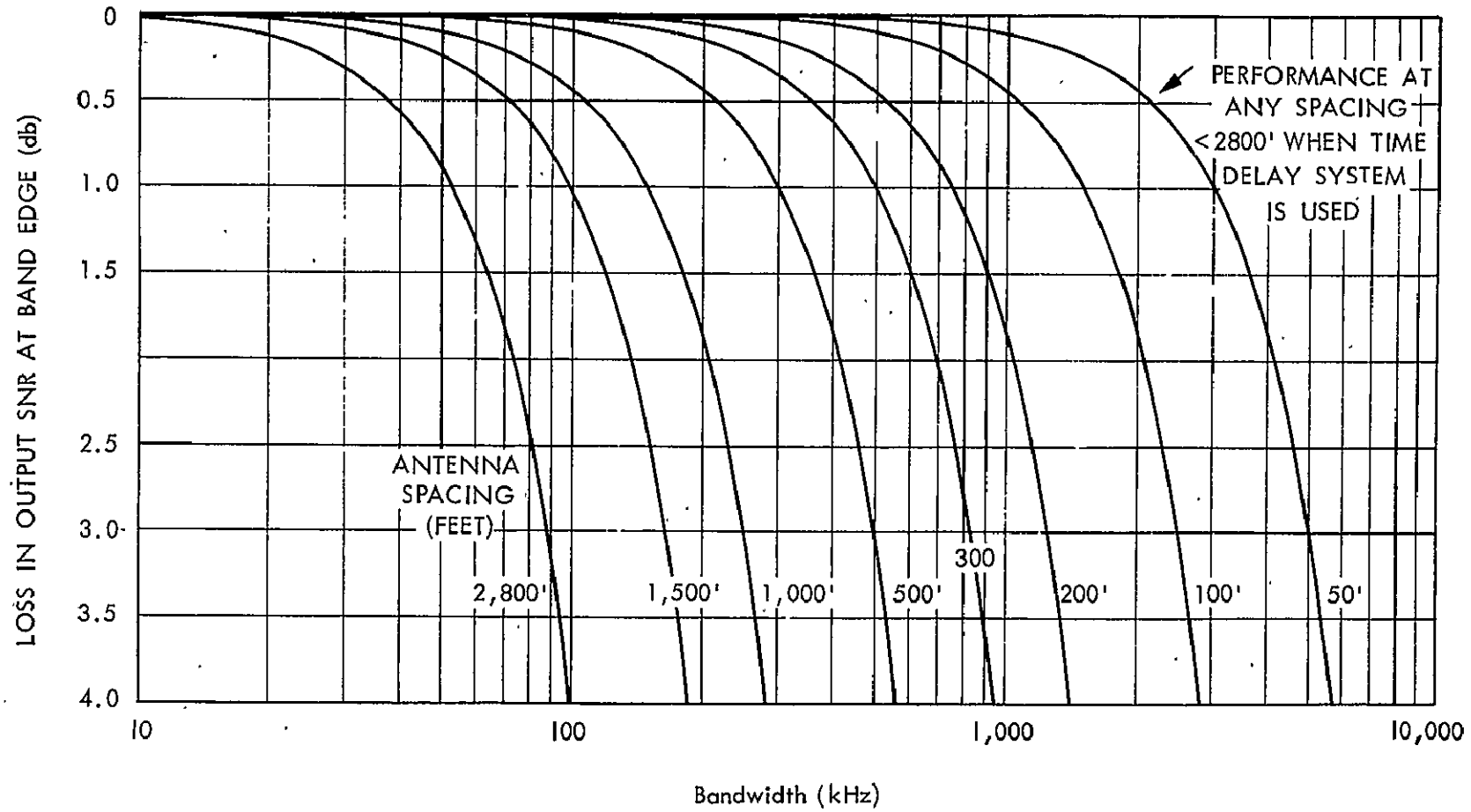

Figure 2-23: Maximum SNR Loss at Band Edge vs. Bandwidth for Several Antenna Spacings

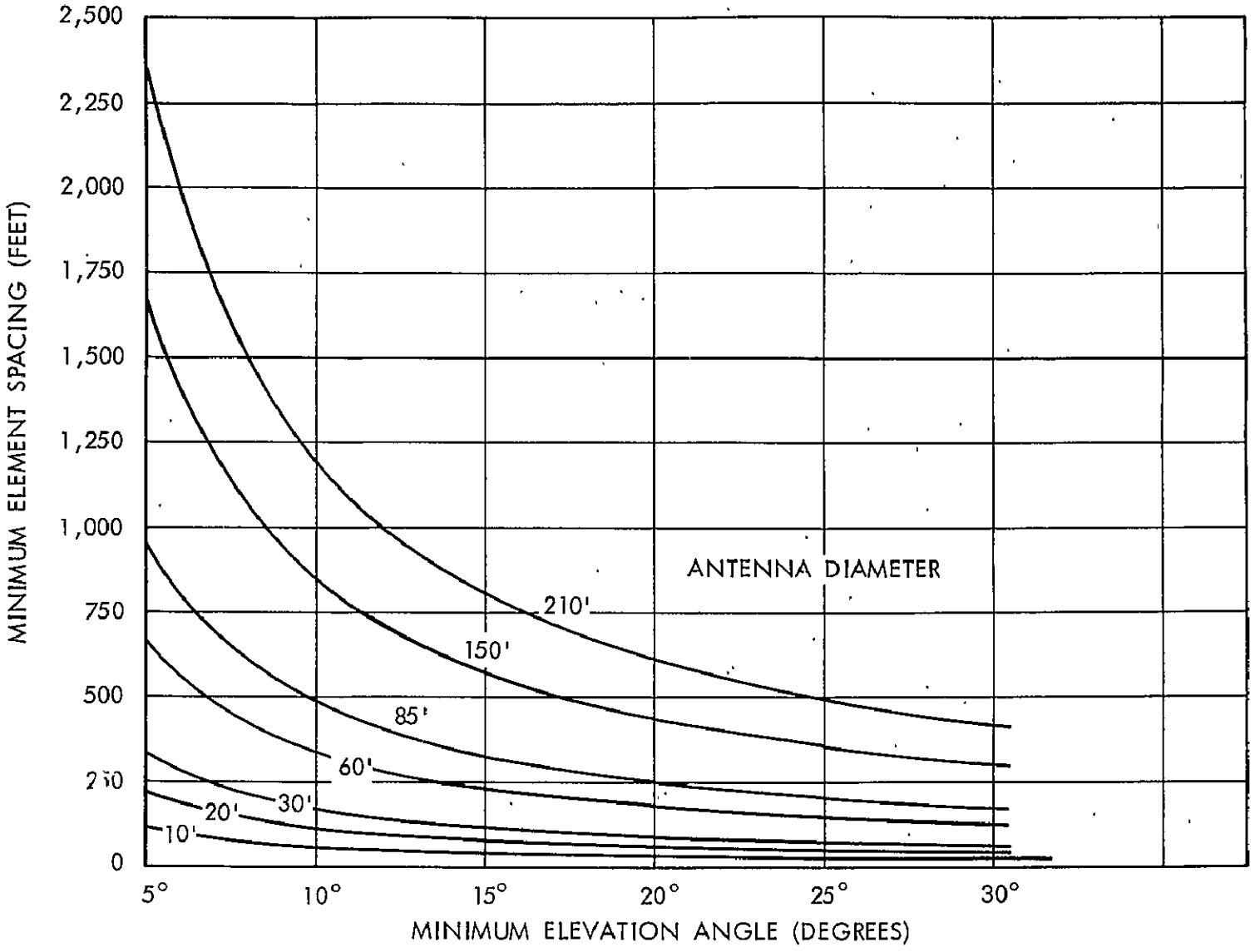

Figure 2-24: Minimum Element Spacing vs. Minimum Elevation to Prevent Shadowing

The transient response tests of the two models indicated significant differences. Figure 2-25 shows the input and output pulse of the transmission line delay model, indicating no distortion of the input envelope with the exception of attenuation. Figure 2-26a indicates the input and output pulse for the lumped parameter model. Note the ripple in the output response prior to start of the delayed pulse and the ripple on the delayed pulse when the input pulse stops. The input and output pulses are superimposed in Figure 2-26b. The peak magnitude of the precursor and postcursor was -14 db below that of the output pulse. The existence of transients in the lumped parameter network model prompted the decision to use transmission line delay increments for the time delay system.

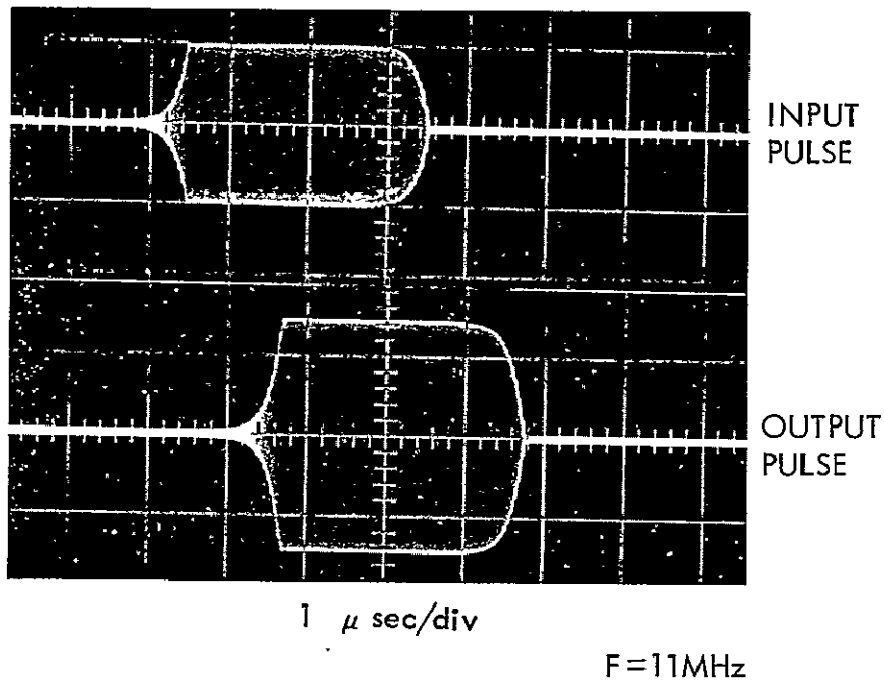

igure 2-25: Transient Response of a 720 Nanosecond Transmission Line Time Delay Breadboard Model Using RG. 178/U Coaxial Cable

For a two element array, the time delay units are incorporated into the IF stage of the phase lock receiver (Figure 2-3) as in Figure 2-27. The reference channel contained a fixed delay of 2.909 μsec. The delay in the variable channel was digitally variable from zero to 5.727 μsec in 90.9 nsec. increments. Increments of 90.9 nsec were chosen to correspond to one period of the 11 MHz IF. Switching in one cycle increments of the carrier minimizes phase transients in the receiver. A block

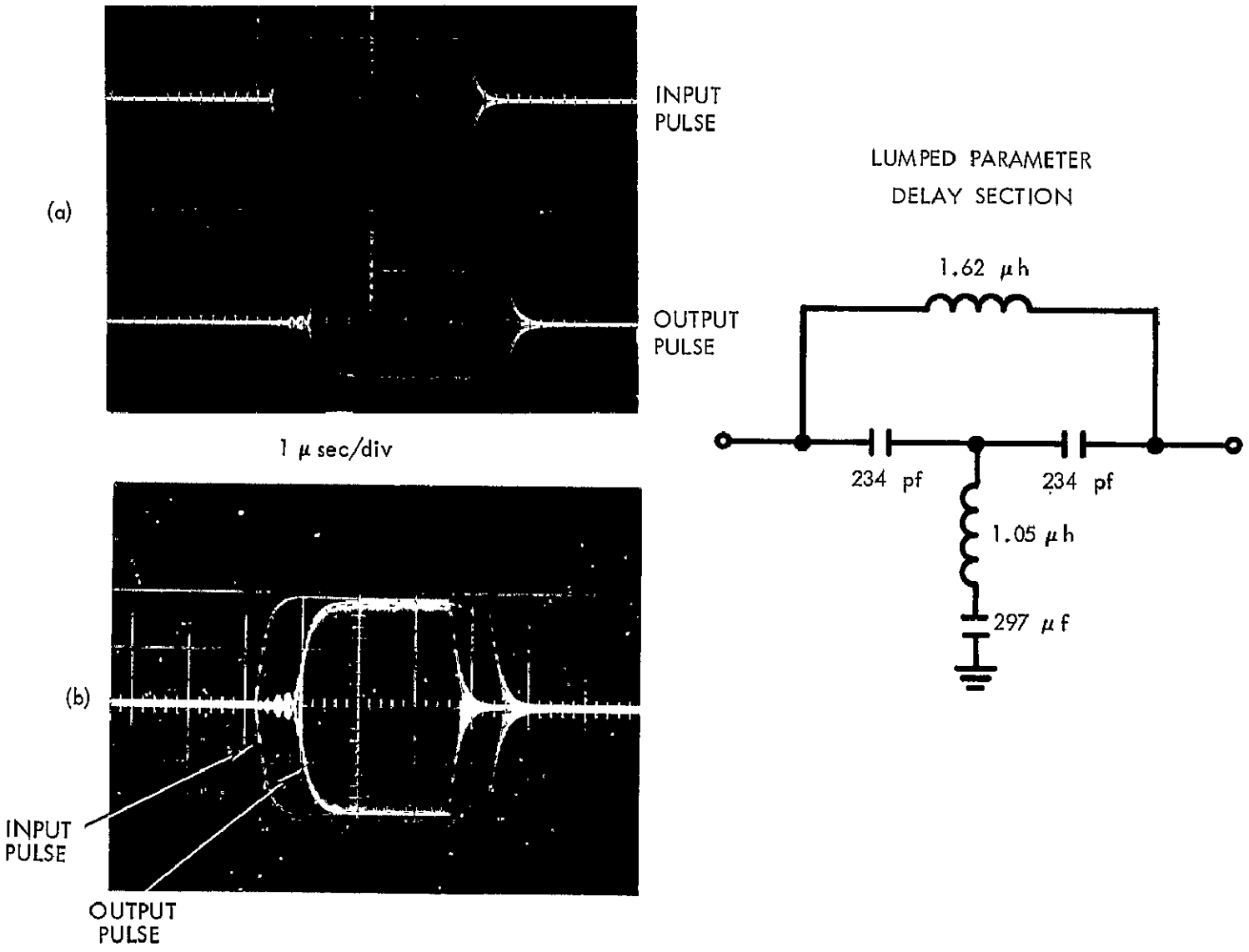

Figure 2-26 a & b: Transient Response of an 8 Section Lumped Parameter Network Breadboard Model

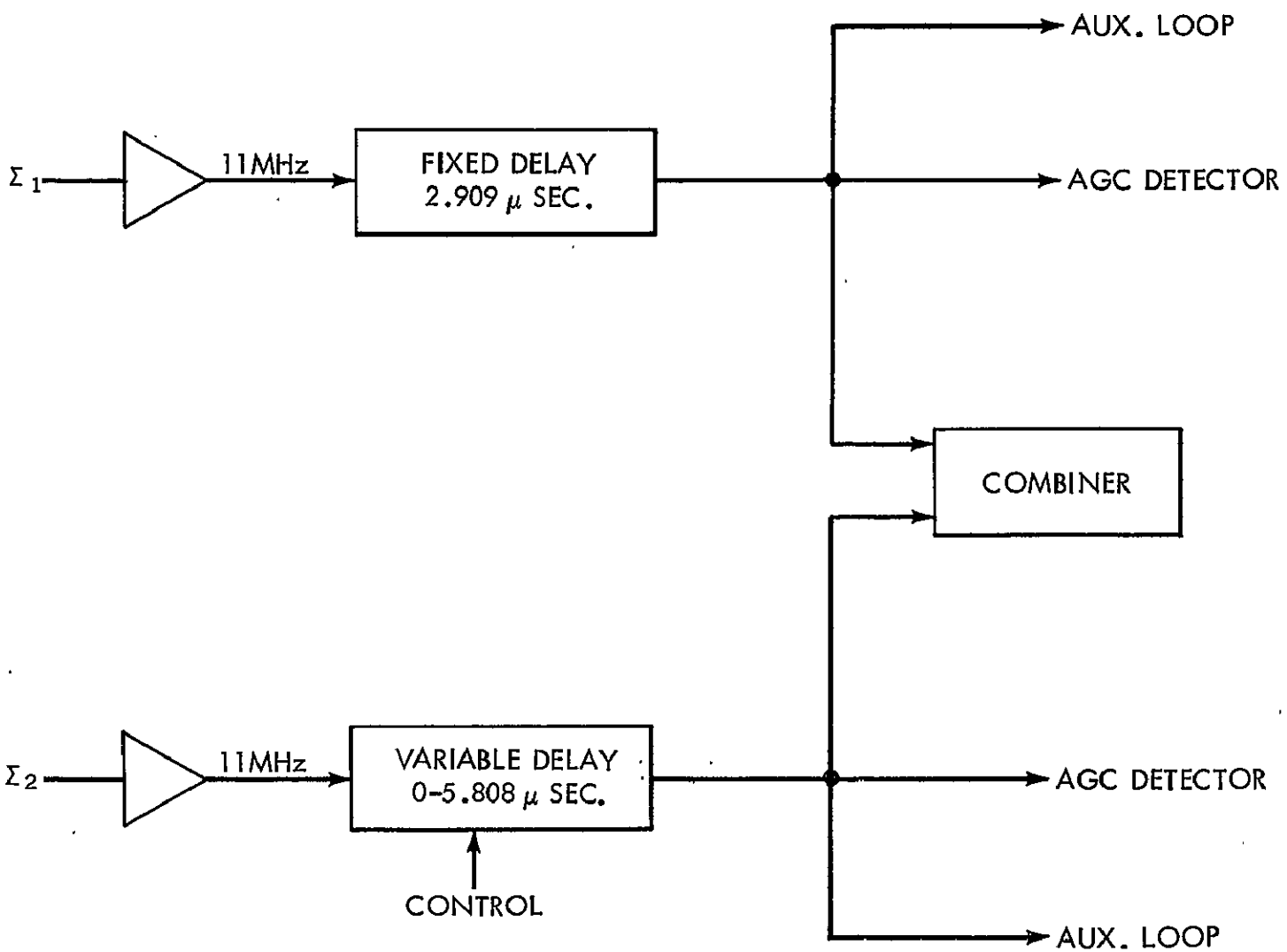

Figure 2-27: Incorporation of Time Delay System Into APDAR Receiver

diagram of the variable unit is given in Figure 2-28. The delay increments were achieved with coils of RG 178/U coaxial cable. Amplifiers ahead of each delay increment were adjusted to maintain a gain of zero for any delay setting. As indicated in Figure 2-23, the time delay system reduces the SNR loss due to time of arrival delay for up to 2800 feet spacing to that which would result from an array with no delay correction at 50 feet spacing.

The time delay system was built by the Philco-Ford Corporation to meet the antenna combining requirements. The system includes both a manual control mode for checkout and an automatic mode for continuous delay correction while tracking spacecraft. A block diagram of the automatic mode of operation is given in Figure 2-29. The process involves taking the normalized azimuth and elevation angle of the spacecraft and calculating the required delay setting. The required delay is then compared to the current setting of the delay system. When the difference between the required and actual delay exceeds 50 nsec, the system is automatically updated to the setting that is within 45 nsec of the calculated delay requirement. A special purpose computer performs this operation based upon the input angles supplied by two Scientific Atlanta Model 1841 Synchro to Digital Converters. The only other parameter, antenna separation, is set by a thumbwheel adjustment on the front panel of the control unit. The special purpose computer within the automatic control unit requires 25 msec to calculate the required time delay. Actual switching time is less than 50 μsec. The automatic control unit will maintain the delay setting within 50 nsec of the calculated value for spacecraft with angular velocities up to three degrees per second.

The improvement in array bandwidth capability can be clearly seen in Figure 2-23. If no time delay system were used a 40 kHz bandwidth at a 2800-foot antenna spacing would result in 0.5 db loss in the output SNR at band edge. With the time delay system included, the 0.5 db bandwidth is extended to 2 MHz. This is a bandwidth extension of 50 times.

The evaluation of the time delay system in the receiver was limited to measurements of AGC and phase. A better indication of the effects would be a measurement of bit error rate but the system did not include demodulation equipment and these tests could not be performed. The effect of switching on receiver AGC is indicated in Figure 2-30 for the fastest AGC speed (25 msec) available on the APDAR receiver. The effect on the relative phase between channels at the input to the combiner is indicated in Figure 2-31. In each case, the effect of switching transients could not be seen in the measurements.

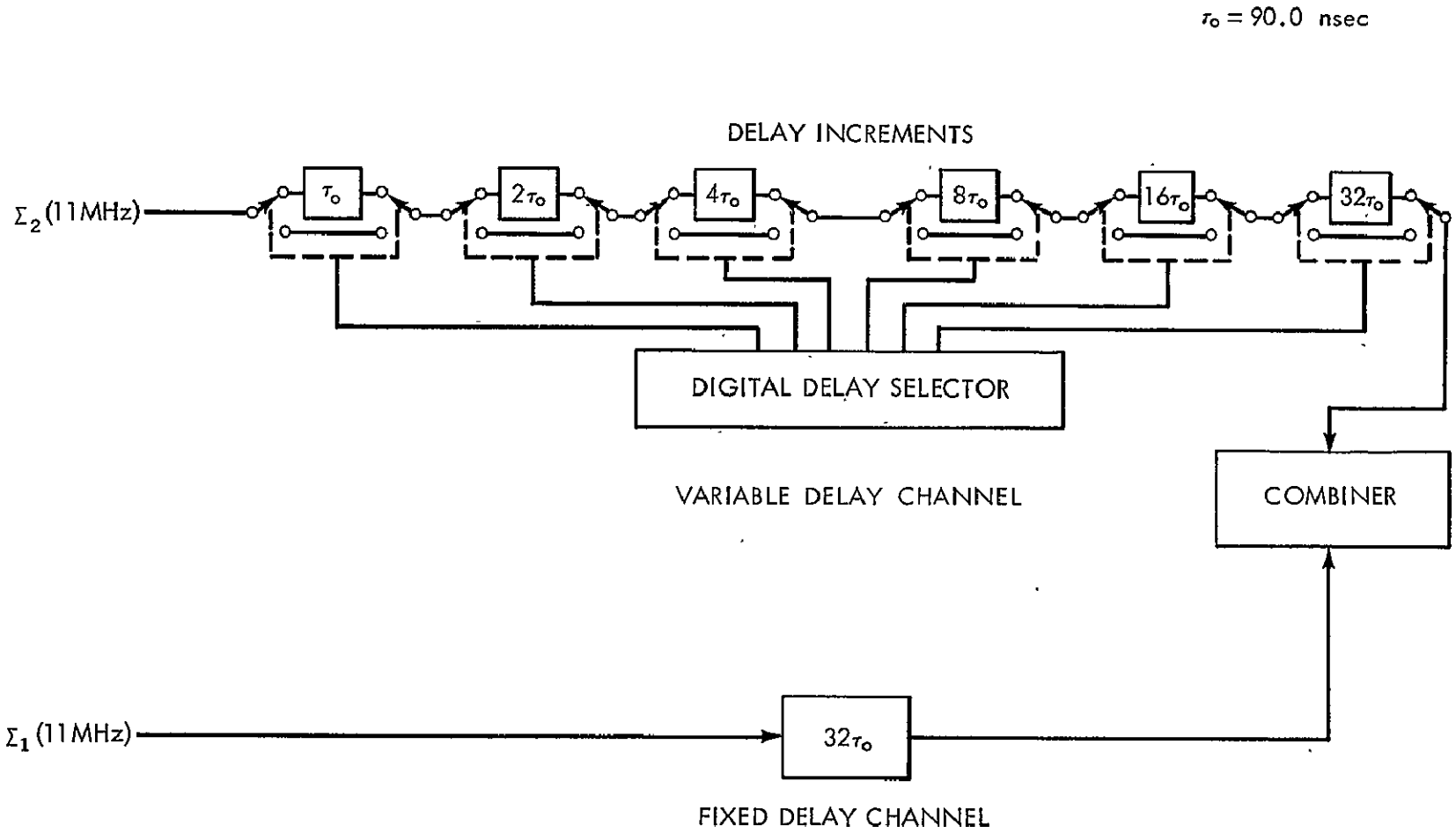

Figure 2-28: Block Diagram of Time Delay Compensation System

$$T = \frac{D}{c} \cos(\theta) \cos(\phi)$$

γ = AZIMUTH ANGLE OF SOURCE REFERRED TO BASELINE
ϕ = ELEVATION ANGLE OF SOURCE
c = VELOCITY OF LIGHT
D = ANTENNA SEPARATION
T = TIME DELAY, SECONDS

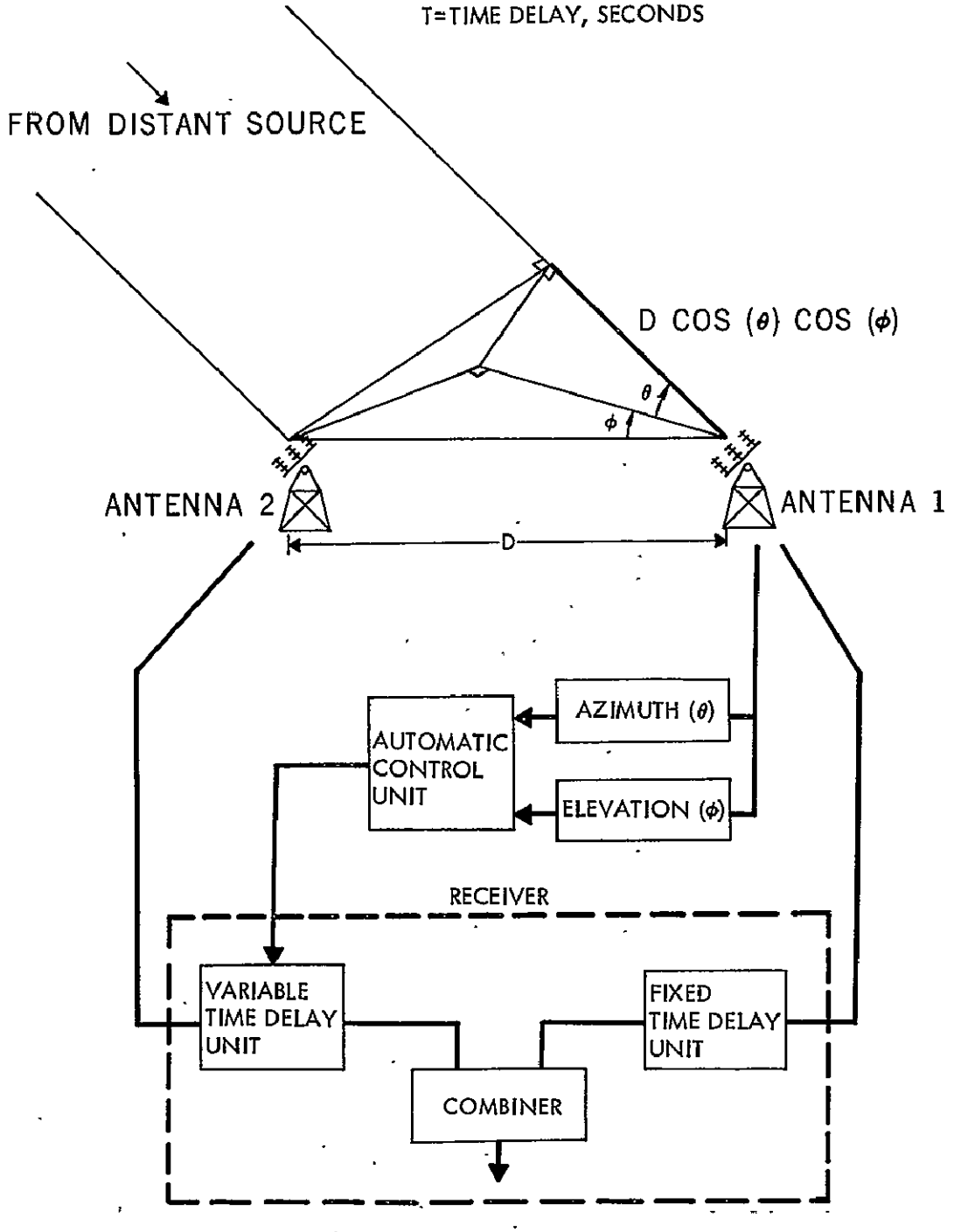

Figure 2-29: Block Diagram of Time Delay System with Automatic Control

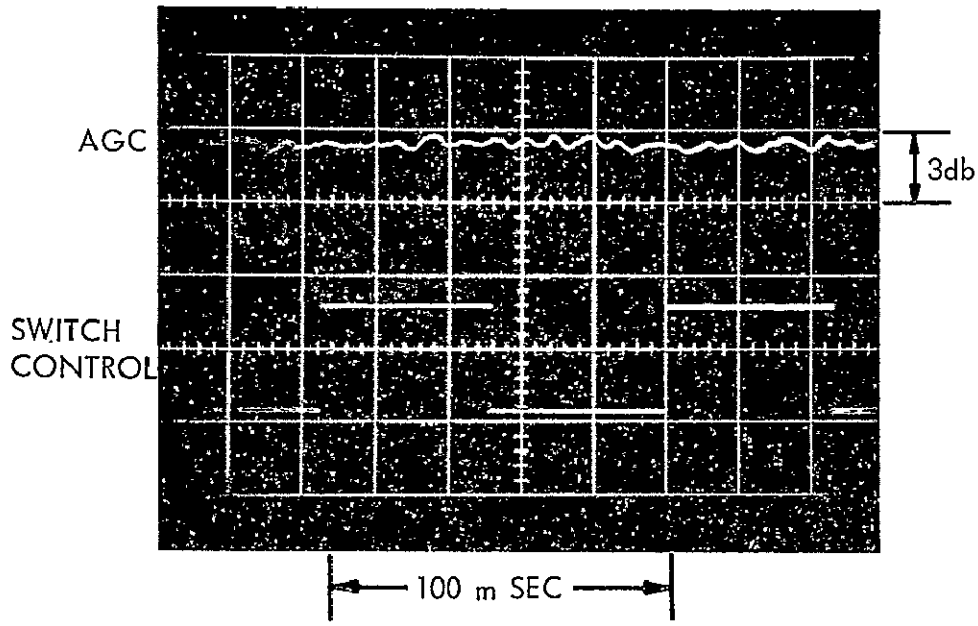

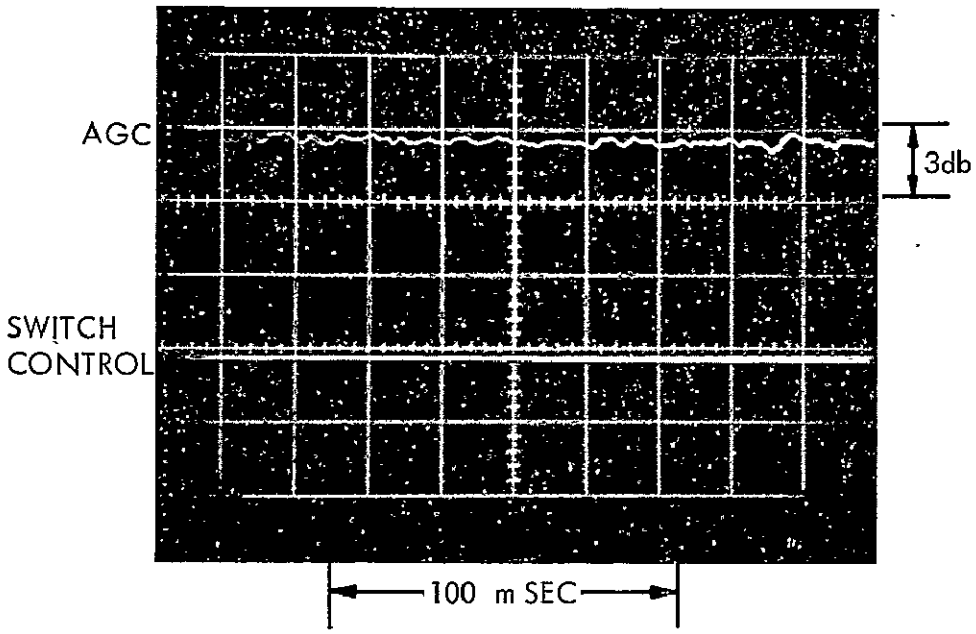

AGC SPEED = 25 m SEC
INPUT SIGNAL LEVEL = -110dbm

Figure 2-30: Effect of Time Delay Switching on Receiver AGC

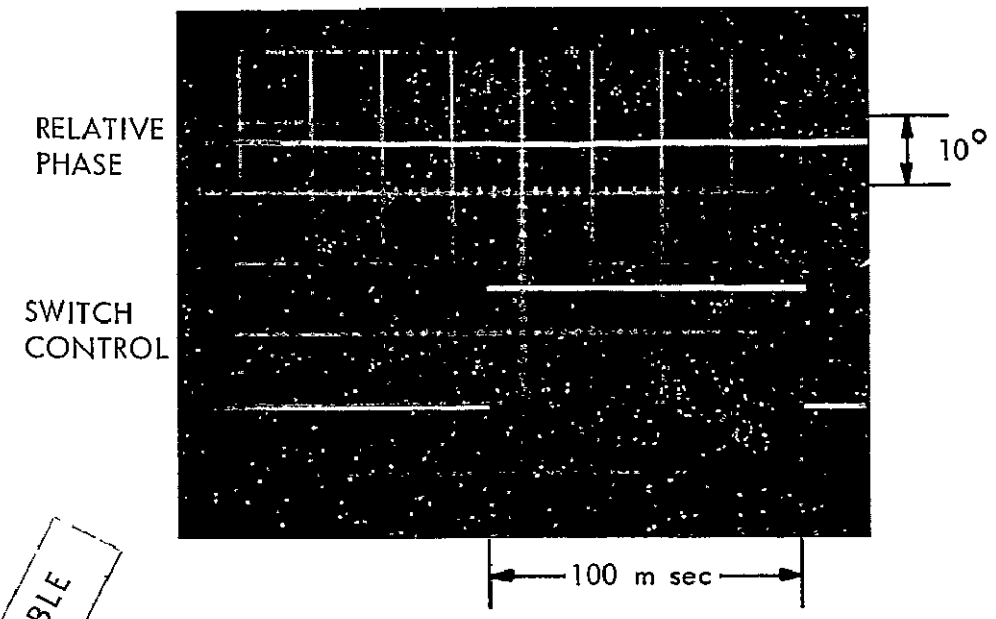

TIME DELAY SYSTEM TEST

NOT REPRODUCIBLE

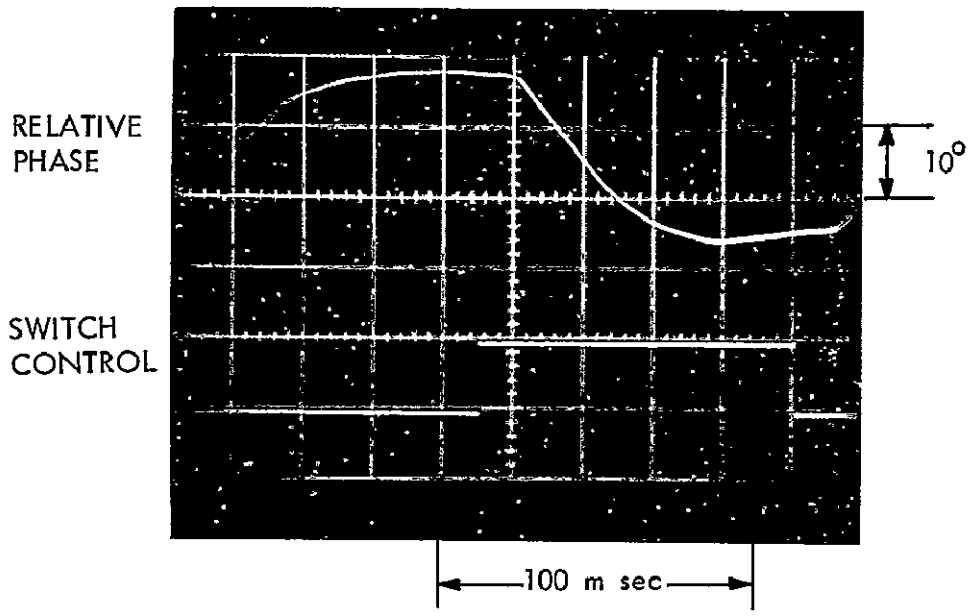

CALIBRATION TEST USING 24° PHASE SHIFT

PHASE DETECTOR BANDWIDTH = 60 Hz

Figure 2-31: Effect of Time Delay Switching on Relative Channel Phase

3 EXPERIMENTS

The objective of the measurement program was to determine the operational feasibility of arraying large aperture antennas for gain improvement. To this end the following considerations were of primary concern.

1. The statistical distribution of gain improvement while tracking spacecraft.

2. The effect of a digital time delay system on receiver performance.

3. A measurement of phase front distortion.

The gain improvement is determined by measuring the carrier to noise ratio improvement at the combined output of the receiver to that in each input channel. The effect of a digital time delay system on phase lock receiver performance has already been summarized in Section 2.3. The measurement of phase front distortion was to be accomplished by comparing the phase of the carrier received at each of two antennas as a function of antenna separation.

The antenna site was located within the Goddard Optical Range Facility in Beltsville, Maryland. Figure 3-1 indicates the site layout with the baseline inclined approximately 10° to the equatorial plane. Each rectangular box represents a concrete pad suitable for a mobile tracking antenna. The reference or master antenna was located permanently on the largest pad at the east side of the baseline. The array was composed of two identical elements with the mobile antenna mounted on a flat bed trailer to facilitate baseline changes.

3.1 Measurement Technique

The gain improvement of the array is equal to the CNR improvement of the combined output over that of the best input channel. Combining is performed at 11 MHz in the APDAR receiver (Figure 2-3). A coherent automatic gain control (AGC) maintains the carrier (C) level at IF essentially constant over its operating range. Each 11 MHz IF channel, however contains carrier plus noise (C+N) which can vary from -35 dbm to -5 dbm typically. For CNR measurements, any modulation present on the carrier contributes to the noise component of the total IF level. Since modulation was present on several of the spacecraft down links that were

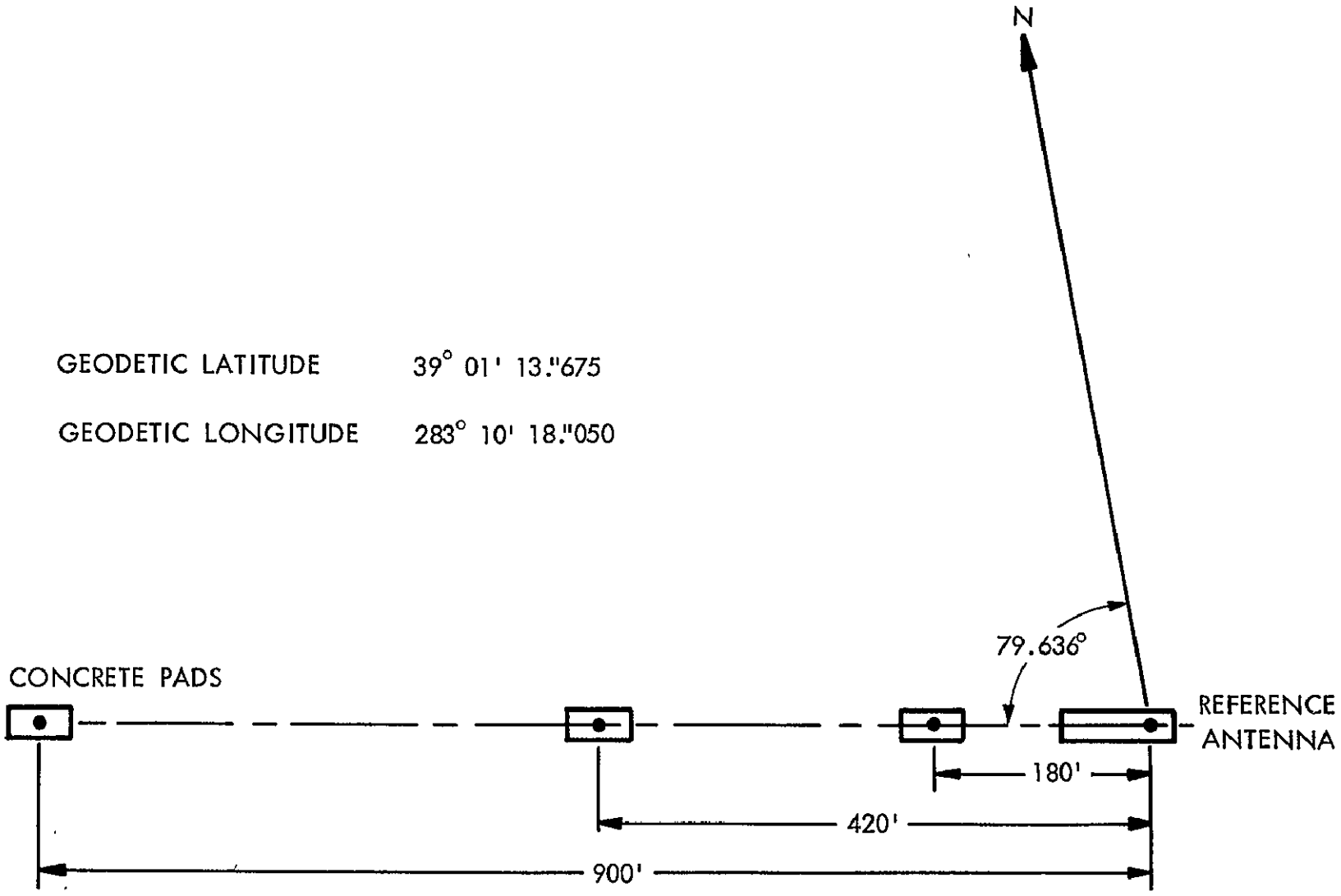

Figure 3-1: Site Layout of Antenna Combing Range

being tracked, it was important that the CNR measurement scheme operate effectively under these conditions.

Figure 3-2 indicates the scheme that was developed for measuring CNR improvement and relative phase. The CNR measurement circuit operates on the same principle as the circuit described for channel weighting using a bandpass limiter (Section 2.2.3d of this report). The only difference in operation is that the noise bandwidth in the CNR measurement circuit was adjusted by changing the IF bandwidth of the receiver (i.e., 30 kHz, 1000 kHz, 300 kHz or 1 MHz). This feature permitted adjusting the noise bandwidth to insure that the CNR into the limiter was below -5 db. Since telemetry was not of concern in these tests the wider IF bandwidth had no effect on system performance. The C and C+N levels are simultaneously measured and recorded for later data processing and calculation of CNR. As shown in Figure 3-2, C was measured with a coherent detector. An rms voltmeter simultaneously monitored the C+N, which was a constant since it followed a hard limiter.

Practically, the CNR calculation would not be continuous but would be determined at discrete intervals. The discrete nature of the output made possible the use of a single detection circuit for all three IF channels: Σ_c, Σ_1 and Σ_2. Channel selection was accomplished by appropriately setting each of three 3-port coaxial switches as in Figure 3-3. The sampled channel is limited, then downconverted to the 3.25 MHz input frequency of the coherent detector. As discussed in Section 2.2.3d, the coherently detected carrier level out of the hard limiter uniquely defines the CNR at IF for a given C+N. The coherent detector output is put on punch paper tape for processing.

The sampling operation was performed automatically. The sampling period was adjustable from one to five seconds. The sampling rate is limited by the coherent detector stabilization time and the recording instruments. Figure 3-4 is a typical strip chart recording of the coherent detector output as a function of time for a five second sampling period. The synchronization pulse on the strip chart represents no input carrier, corresponding to input port IV of Figure 3-3. The synchronization pulse allows an observer to easily identify each of the three IF channels on any recording.

Detection of the relative phase between signals received at the two antennas was a much simpler process than that required for CNR measurements. The CNR at the 11 MHz IF varied, typically, from +16 db for RELAY II to 0 db for ATS-C. The relative phase measurements should be as independent of the received carrier levels as possible to reduce

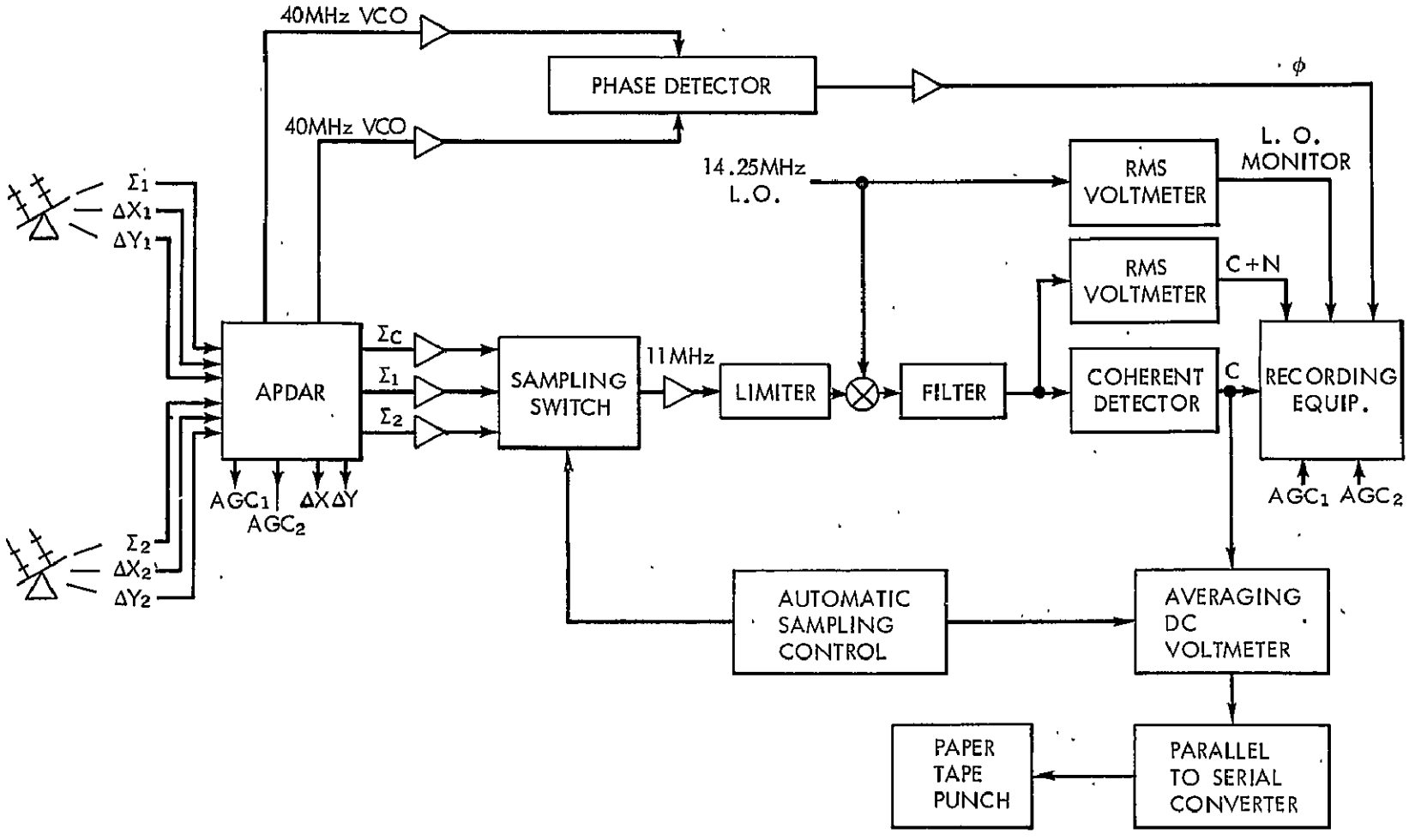

Figure 3-2: Block Diagram of Measurement Scheme

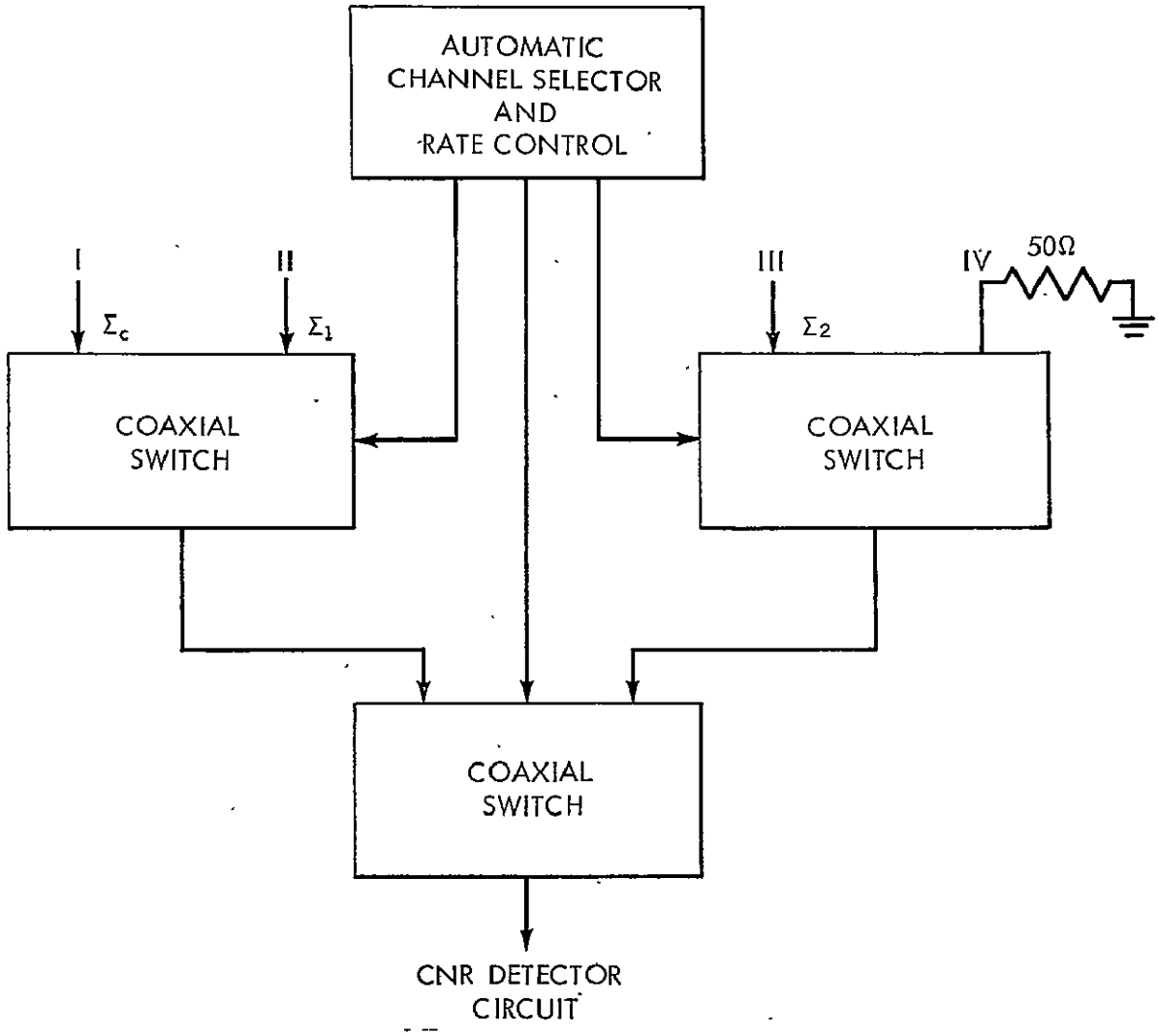

Figure 3-3: Sampling Switch

the noise contributions in low CNR situations. The APDAR receiver described earlier (Figure 2-3) provides independent automatic gain control to each input channel. This AGC process minimizes the effect of incoming signal level variations, permitting the phase detectors used to control the PLLs to operate on a constant 11 MHz input. The phase detector output then modulates a nominal 3.2 MHz carrier for each input channel. A similar process is performed in the combined sum channel with the phase information modulating a 43.2 MHz carrier. The order of the filters used in the input and combined channels are such that the doppler frequency shifts are supported by the 43.2 MHz and the lower frequency phase changes by the 3.2 MHz carrier.

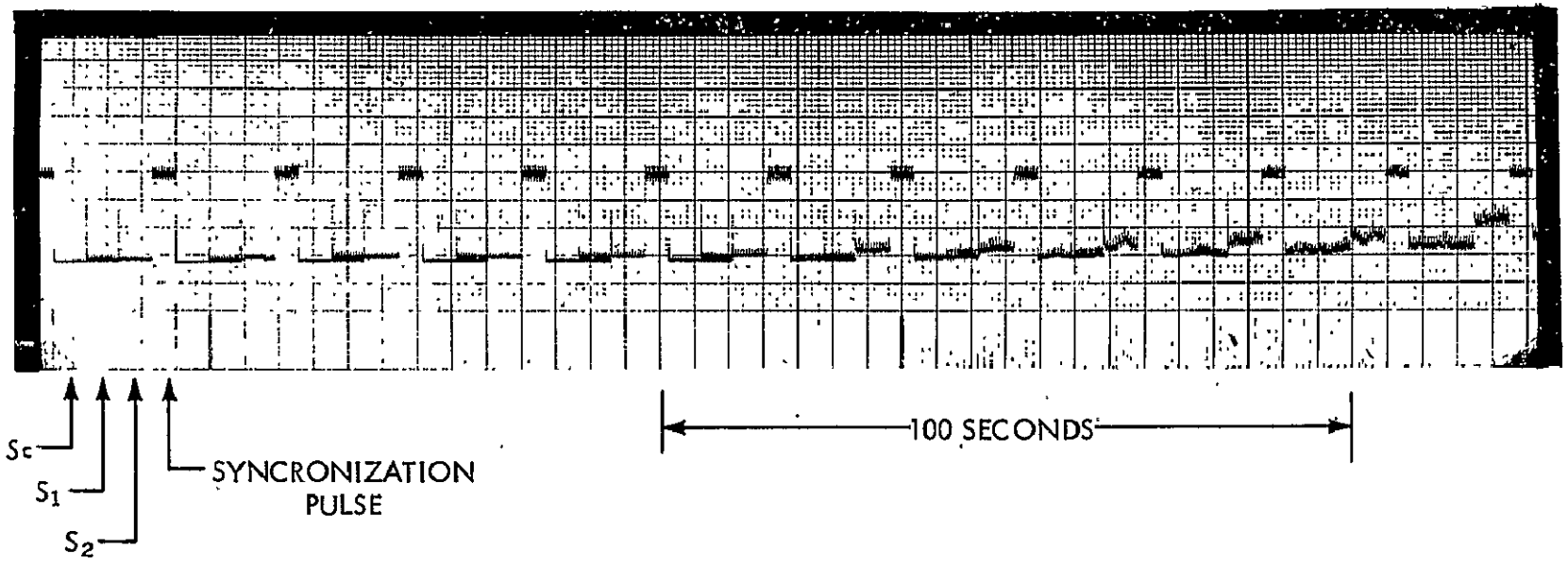

Figure 3-4: Typical Detection Sequence for CNR Measurements

The 43.2 MHz VCO output is mixed with each 3.2 MHz signal and the corresponding 40 MHz components are used in the second mixing stage of the receiver. Each 40 MHz signal then contains the following components:

$$S_1(40\ \text{MHz}) = A_1 \cos\left[2\pi(F_o + F_{d1})\ t + \theta_1\right]$$

$$S_2(40\ \text{MHz}) = A_2 \cos\left[2\pi(F_o + F_{d2})\ t + \theta_2\right]$$

where:

F_o = 40 MHz nominal

F_{d1}, F_{d2} = doppler frequency shifts seen at each antenna

θ_1, θ_2 = phase difference between each input channel and the receiver reference.

The magnitude of A_1 and A_2 are determined by the VCO output levels and are constant. By mixing the two 40 MHz signals together, followed by a low pass filter, the output will be:

$$\phi = \frac{A_1 A_2}{2} \cos\left[2\pi(F_{d1} - F_{d2}) + (\theta_1 - \theta_2)\right] \qquad (1)$$

Where $F_{d1} - F_{d2}$ represents the differential doppler frequency and $(\theta_1 - \theta_2)$ represents the relative phase due to path length differences, constant phase differences in the two channels and effects of the propagation medium. The ϕ given by Equation (1) is the relative phase difference between the received signals and was recorded on magnetic tape for later processing.

This technique offers several desirable features in performing the relative phase measurements. The more significant of these features are given below:

1. Completely eliminates the overall doppler frequency components.

2. Provides measurement accuracy equal to that performed in the APDAR receiver.

3. Minimizes the effect of incoming signal levels.

20

3.2 VHF Results

The 136 MHz array consisted of two five element Yagi arrays (Figure 3-5). One Yagi element was situated at each corner of a 12.3 foot square support structure. The fifth element was centrally located and weighted 6 db greater than the corner elements in forming the sum beam to reduce sidelobe levels in the principle planes. The monopulse error channels are formed from the corner elements only. Figure 3-6 gives a circuit diagram of the monopulse network. The array is right circular polarized. Figures 3-7 and 3-8 represent the sum and error channels respectively in one principle plane (azimuth).

Solid state preamplifiers for each monopulse channel were mounted directly at the antenna output terminals. The preamplifiers were nominally 30 db gain with a 10 MHz 3 db bandwidth. The sum channel preamplifiers were chosen to match their noise figures at 3.5 db so that front end noise figures would not contribute to errors in the AGC weighting process (Section 2.2.4) of the APDAR receiver. Semi-rigid coaxial cables (1/2 inch diameter) with foamed polyethylene dielectric were used between the antennas and electronics van. The cable length varied with antenna separation but was identical for each antenna at any given spacing.

Relay-2, ESSA-6 and ATS-3 were used as sources for the VHF experiments. Relay-2 transmitted 0.25 watts CW at 136.14 MHz. At a nominal range of 6,000 km, the signal level at the receiver was -83.5 dbm resulting in a +16 db CNR in the 30 kHz IF bandwidth of the APDAR. The ESSA-6 136.77 MHz CW beacon also transmitted 0.25 watts, but at its nominal range of 4,000 km the CNR at the receiver was 19.2 db. Both Relay-2 and ESSA-6 gave a CNR of greater than 10 db in a 30 kHz IF bandwidth and neither of these two satellites could be used to measure gain improvement. ATS-3 transmitted 0.75 watts of PCM/PM telemetry. With all the transmitted power in the carrier the CNR at the receiver is +5 db with 30 kHz bandwidth. The measured CNR for ATS-3 varied between +5 db and -5 db and was therefore an ideal source for gain improvement tests. The CNR measurement circuit works on the same principle as the weighting scheme described in section 2.2.3d. Therefore, the modulation on the carrier does not contribute significantly to the CNR measurements. Figure 3-9 indicates the distribution of measured gain improvement of the combined output over that of each input channel. The median gain improvement was 2.5 db.

The distribution in Figure 3-9 is an average of all the experiments and does not indicate the improvement in CNR at the output over that of the best input channel for any given test. This information is shown in

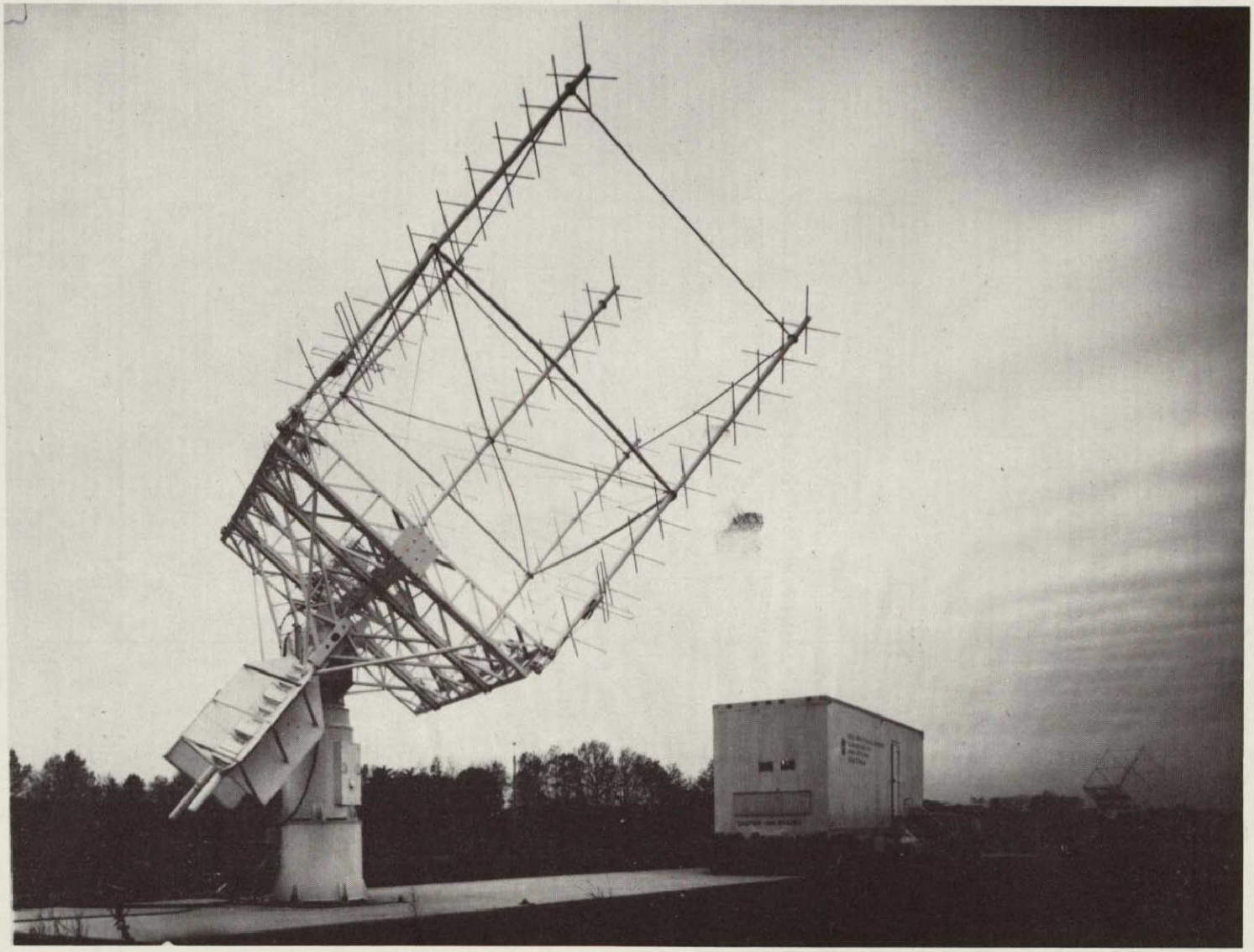

NOT REPRODUCIBLE

Figure 3-5: Two Element VHF Array and Electronics Van

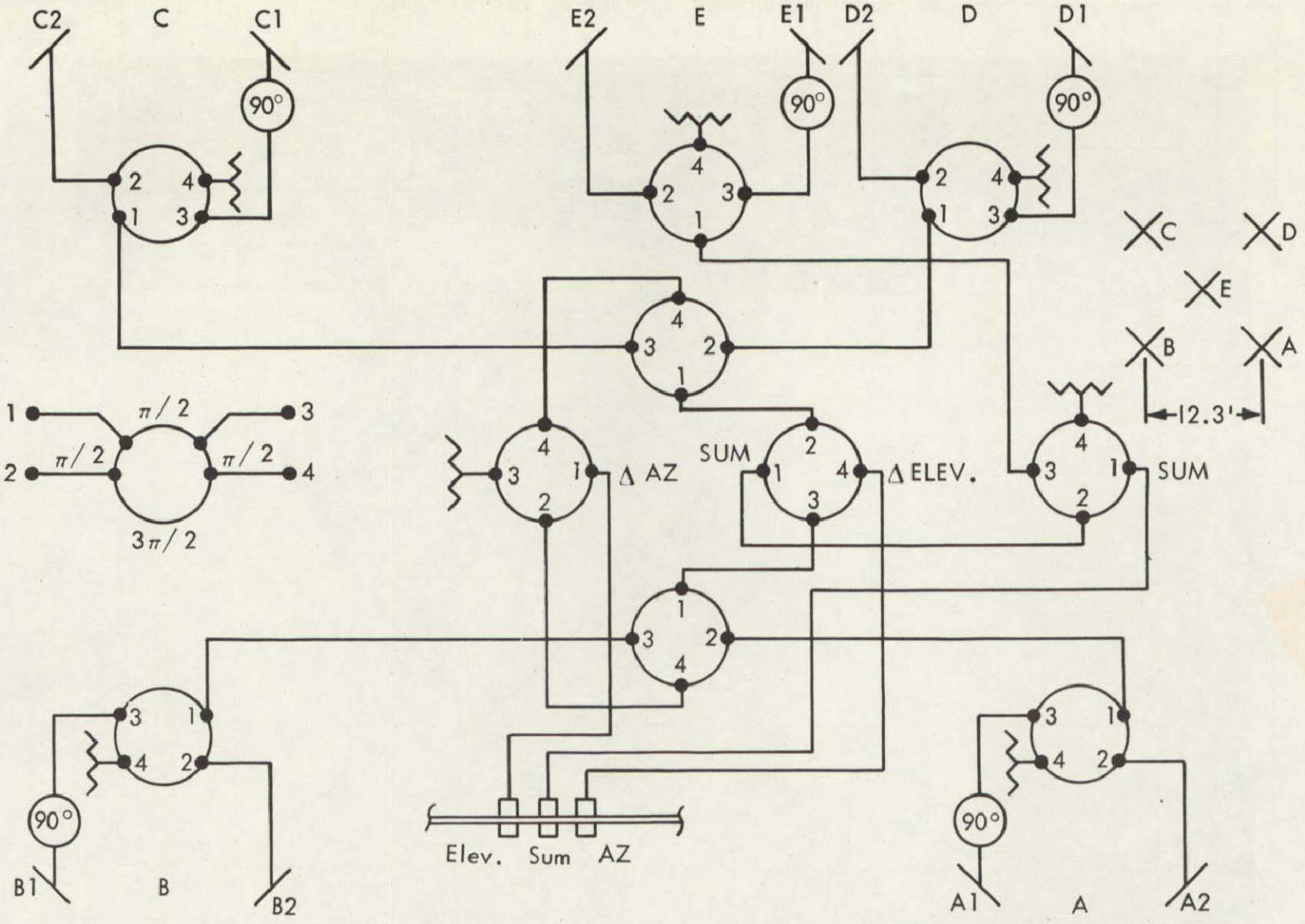

Figure 3-6: Circuit Diagram of Monopulse Network for a Five Element Yagi Array

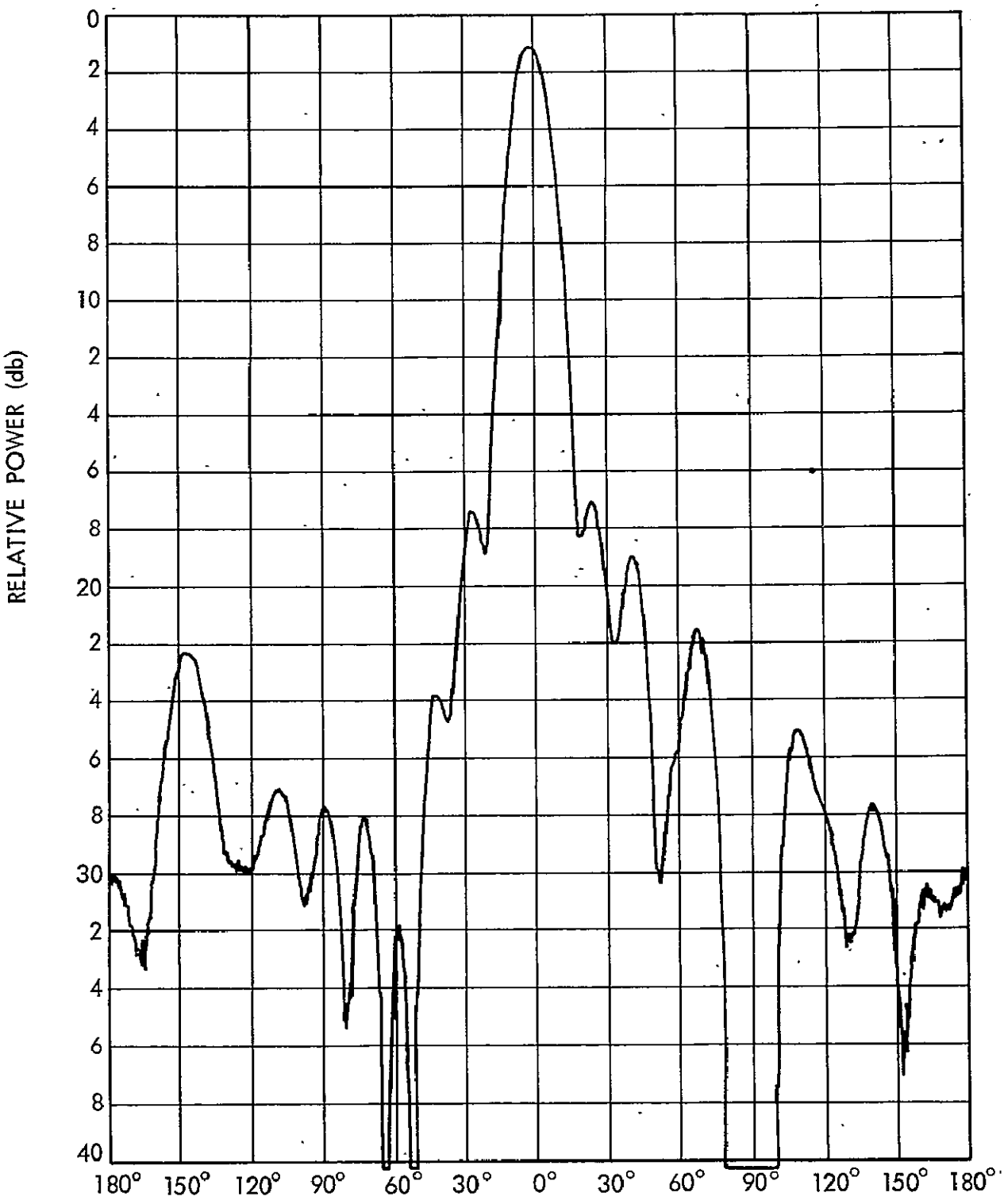

igure 3-7: Sum Pattern of YAGI Array, RHC Polarization

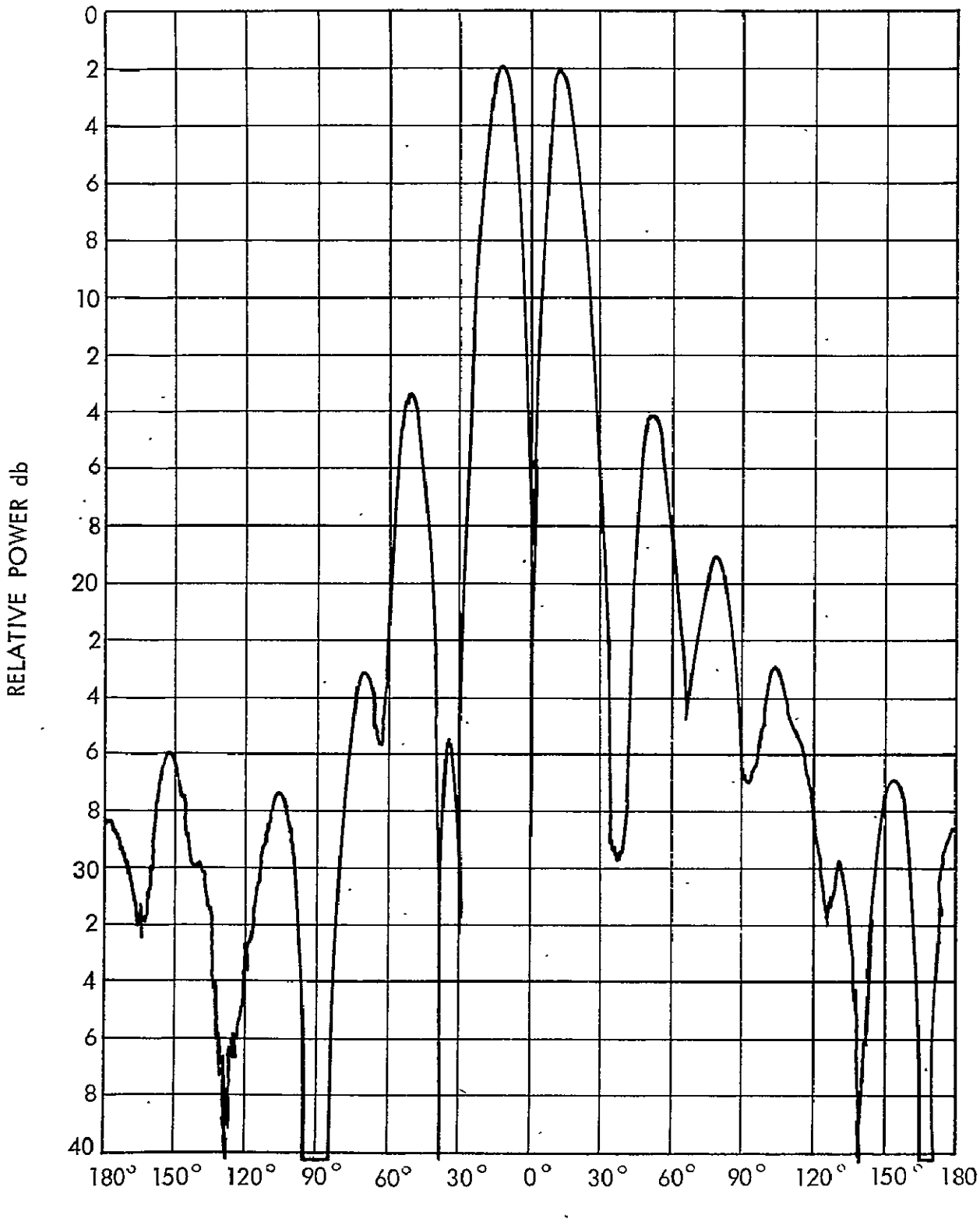

Figure 3-8: Azimuth Difference Pattern for YAGI Array, RHC Polarization

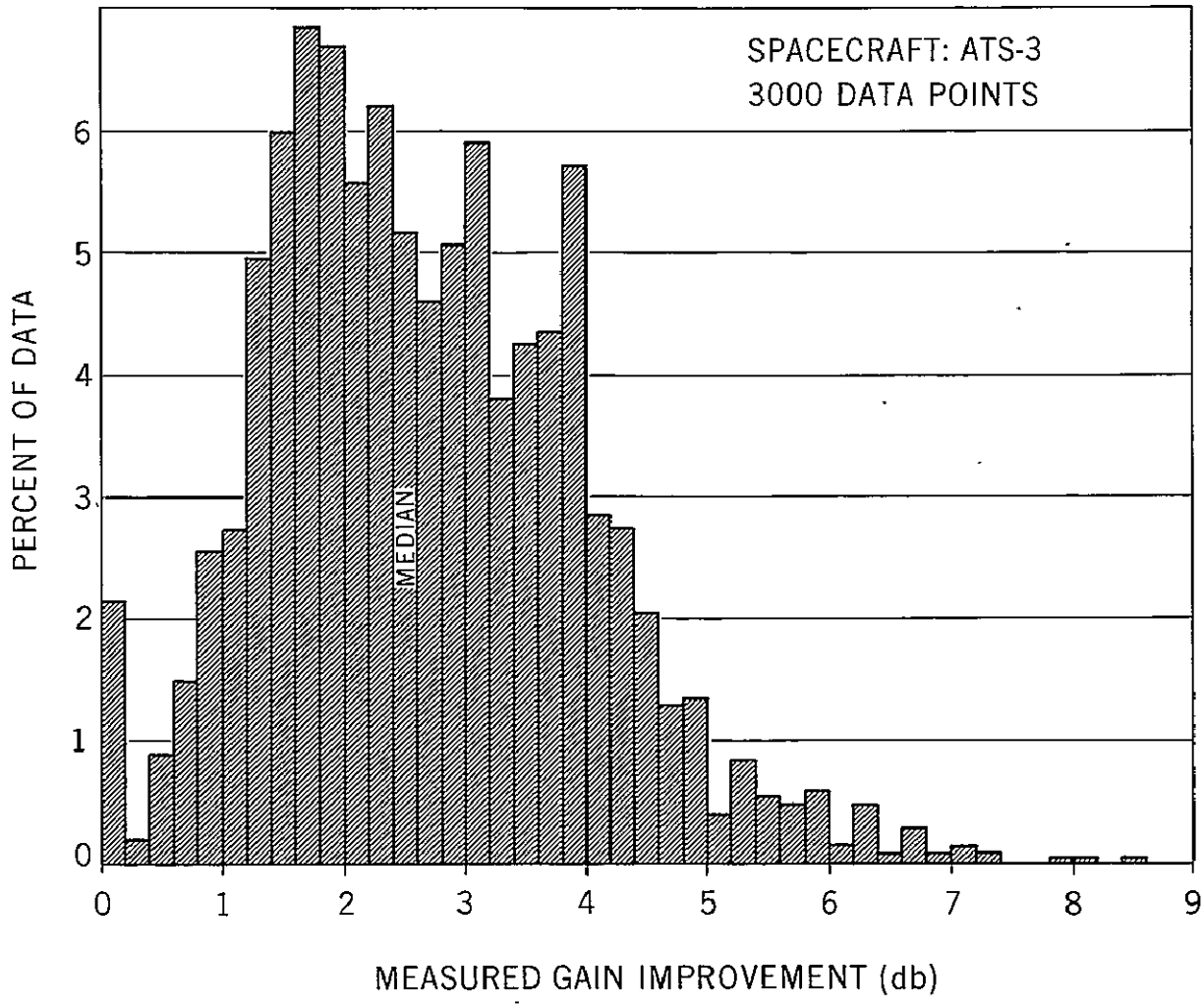

Figure 3-9: Combined Results Including Data from Channels 1 and 2

Figure 3-10. The upper curve represents the maximum gain improvement distribution of the combined output over that of the best input channel based upon the relative CNR in the input channels of the receiver for each test. The dashed line represents the distribution 0.5 db below the theoretical curve. The solid line indicates the distribution of measured results computed on the basis of individual experiments. Approximately 90% of the experiments gave a gain improvement within 0.5 db of theoretical expectations. The data presented in Figures 3-9 and 3-10 are a summary of four hours of measurement consisting of ten 25 minute testing periods during the months of February and March 1968.

The relative phase between antennas was measured and recorded on magnetic tape. The measured time varying relative phase includes

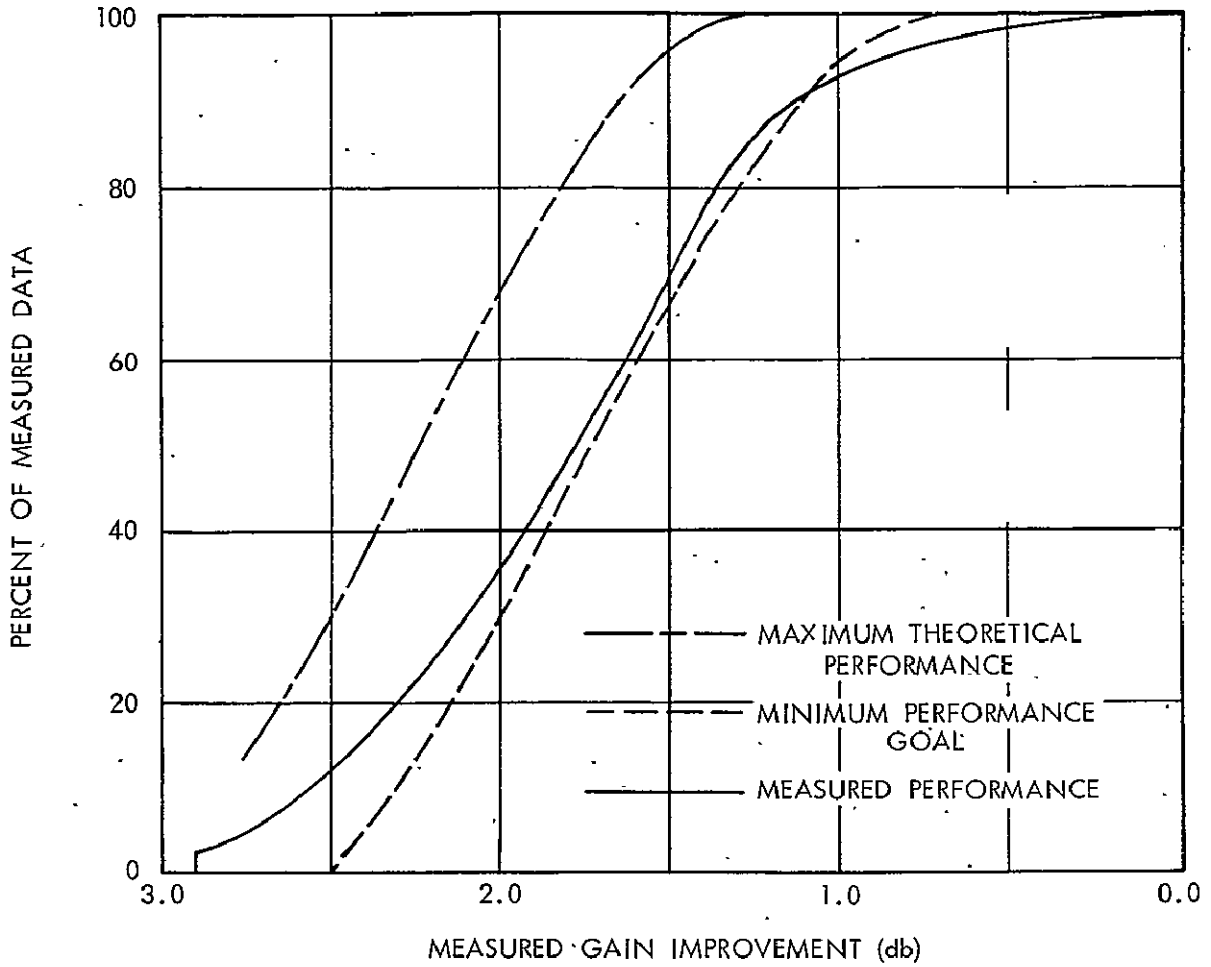

Figure 3-10: Cumulative Distribution of the Measured and Expected Gain Improvement (ATS-C Experiments)

components due to uncorrected time of arrival delay and differential doppler as well as phase front distortion. However, time delay will contribute only to the low frequency components of the measured relative phase. The strip chart recording in Figure 3-11, for example, shows the time delay component as the predominant sinusoidal variation. The differential doppler at VHF was less than 1 Hz for Relay-2 at 900 feet antenna spacing. Therefore the phase front distortion can be separated from the measured relative phase if those components are greater than 1 Hz. A spectral analysis of the relative phase data was therefore performed to determine the dependence of measurable phase front distortion on antenna separation.

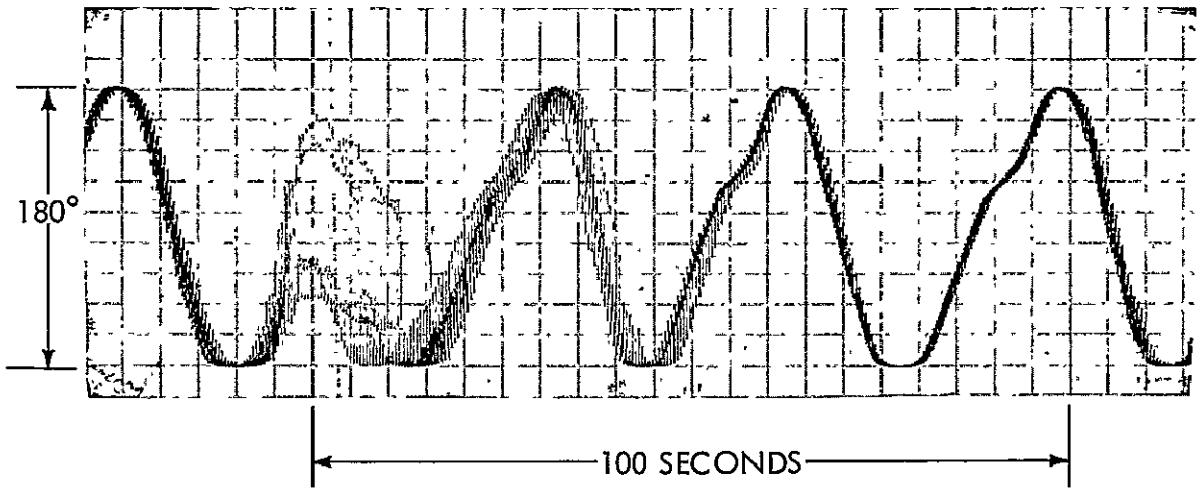

STRIP CHART RECORDING OF RELATIVE PHASE

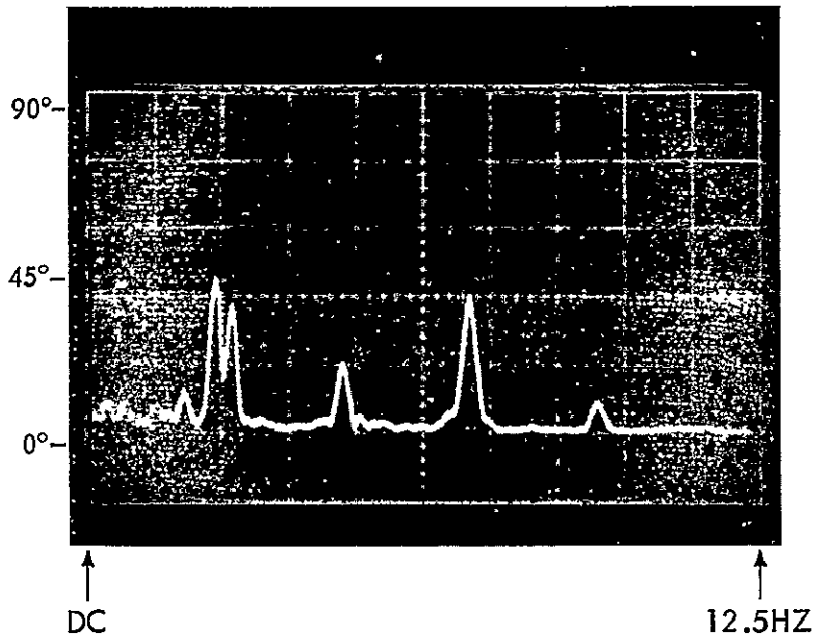

TYPICAL FREQUENCY SPECTRUM OF THE RELATIVE PHASE

Figure 3-11: RELAY 2 Experiment, 180' Antenna Spacing

An antenna separation of 180 feet resulted in a relatively calm response as shown in Figure 3-11 and 3-12. ESSA-6 showed significant response only for frequencies below 1 Hz, and these are predominantly due to changing time of arrival delay. Relay-2, however, contained repetitive frequency components of approximately 2.5, 4.5 and 6.8 Hz.

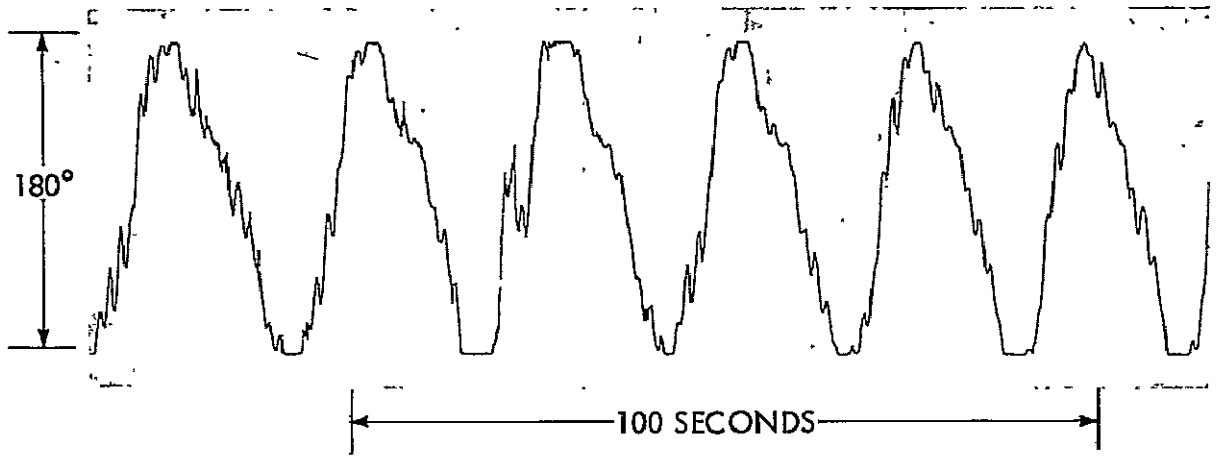

STRIP CHART RECORDING OF RELATIVE PHASE

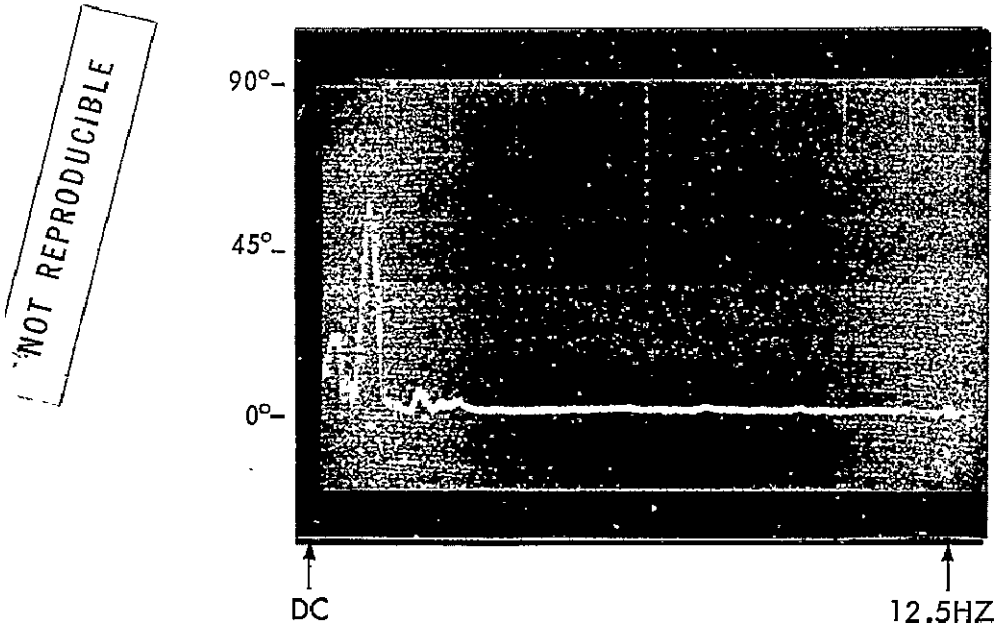

TYPICAL FREQUENCY SPECTRUM OF THE RELATIVE PHASE

Figure 3-12: ESSA-6 Experiment, 180' Antenna Spacing

These components were measured only with Relay-2 and were present at all array spacings. These components are characteristic of the satellite and related to its spin rate of approximately 2 rps, as compared to 16 rpm for ESSA spacecraft.

The random phase components for the 180 foot spacing were small for both satellites, but increased directly with antenna separation. Figures 3-13 and 3-14 give results at a 440 foot spacing. ESSA-3 indicates small random phase contributions over the entire frequency band investigated. Relay-2, however, contained large random contributions at distinct frequencies, the frequencies being in general non-repetitive. The frequency components predominating at the 180 foot spacing were also present at 440 feet but were considerably less significant.

Increasing the antenna spacing to 900 feet resulted in a small increase in the random components of the phase spectra for both Relay-2 and ESSA satellites. The change from 440 to 900 foot spacing was considerably less significant than from 180 to 440 feet. Figures 3-15 and 3-16 represent two experiments with Relay-2 which indicate substantial differences for a 900 foot antenna spacing. The difference in relative phase spectra for Figures 3-15 and 3-16 was a phenomenon that occurred, to a lesser extent, at all spacings and attempts to correlate the spectral characteristics with satellite trajectory and local weather conditions have been unsuccessful.

The spectra of the relative phase (Figures 3-11 through 3-16) represent eight-second averages of the data recorded on magnetic tape. Although these photographs indicate the spectra for only a few seconds of an entire pass, care was taken to make them as representative of the actual data as possible. The strip chart segments associated with each spectrum represent typical relative phase measurements corresponding to that experiment. The slowly varying relative phase components are due to changing time-of-arrival delay between antennas, and the rate of variation is a function of the satellite angular velocity and the antenna spacing.

The occasional superposition of large random components on the strip chart recordings for Relay-2 are due to periods of signal fading in one of the antennas. Frequency spectra of this data indicate that these periods of increased activity are random. Spectral analysis beyond 12.5 Hz was performed. However, since no repetitious components were present and since the random components were similar to those for spectra below 12.5 Hz, the data is not presented here.

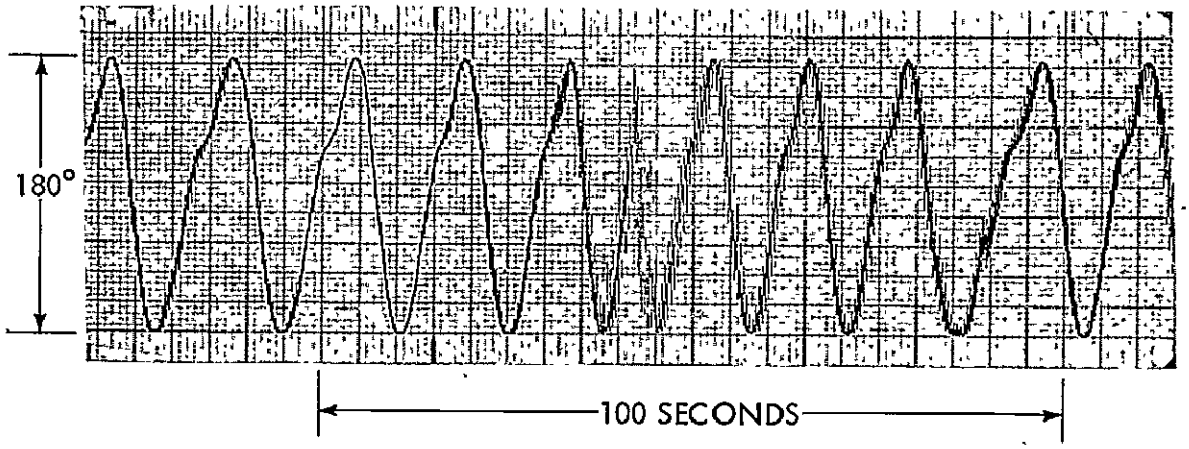

STRIP CHART RECORDING OF RELATIVE PHASE

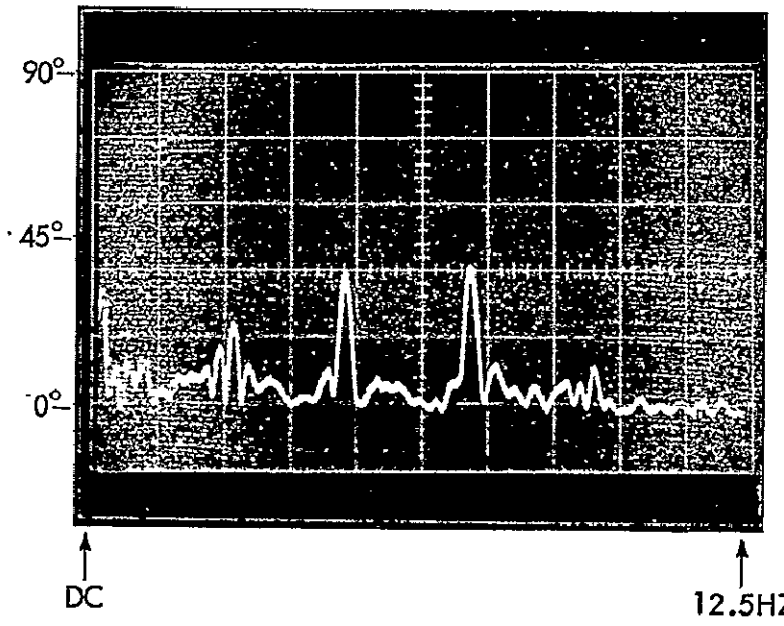

TYPICAL FREQUENCY SPECTRUM OF THE RELATIVE PHASE

Figure 3-13: RELAY 2 Experiment, 440' Antenna Spacing

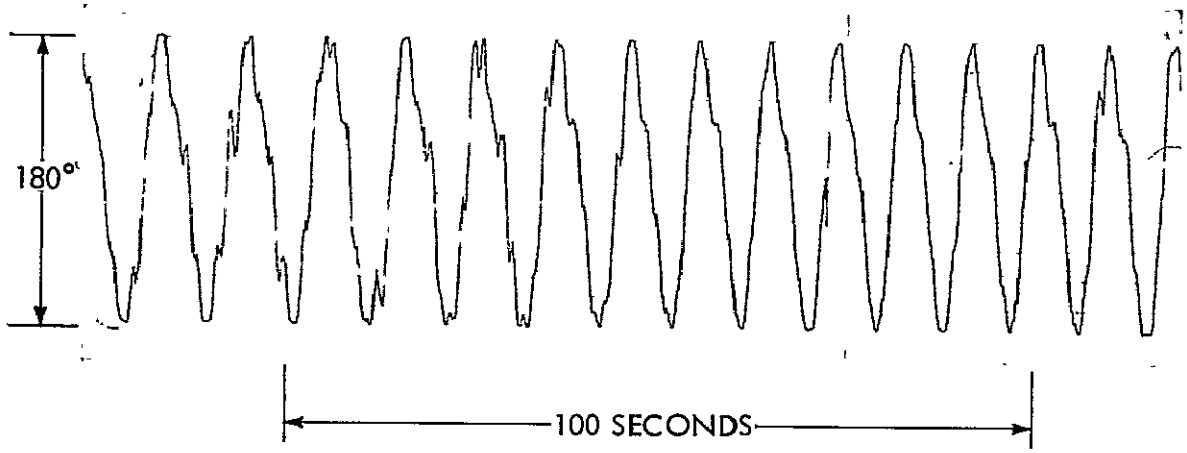

STRIP CHART RECORDING OF RELATIVE PHASE

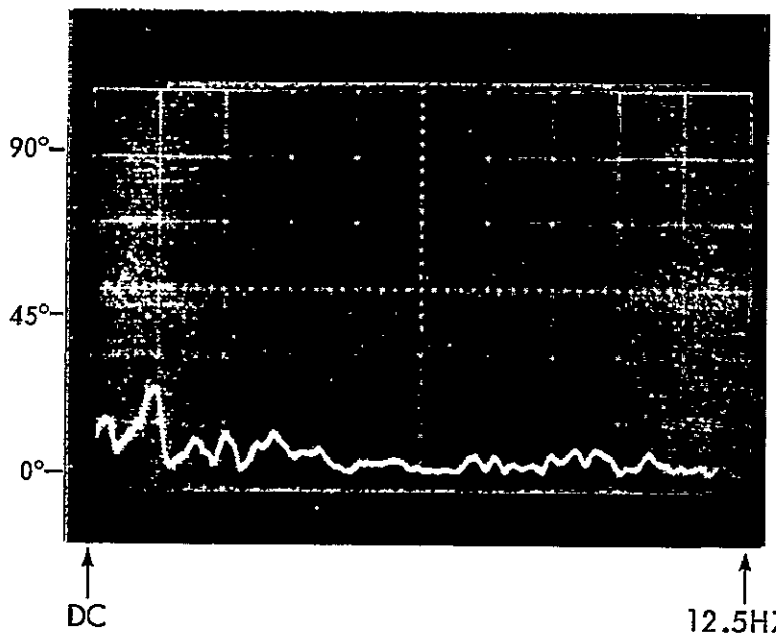

NOT REPRODUCIBLE

TYPICAL FREQUENCY SPECTRUM OF THE RELATIVE PHASE

Figure 3-14: ESSA-3 Experiment, 440' Antenna Spacing

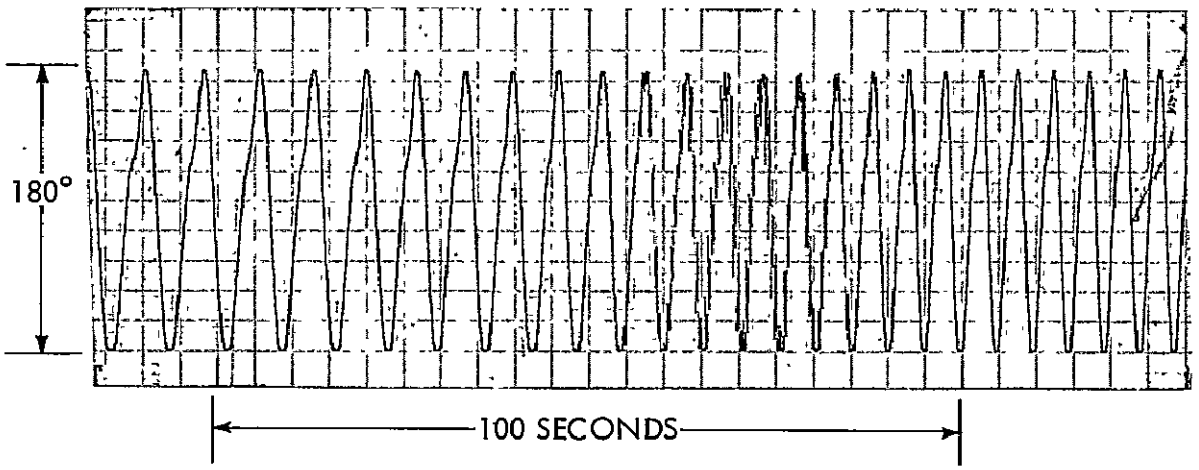

STRIP CHART RECORDING OF RELATIVE PHASE

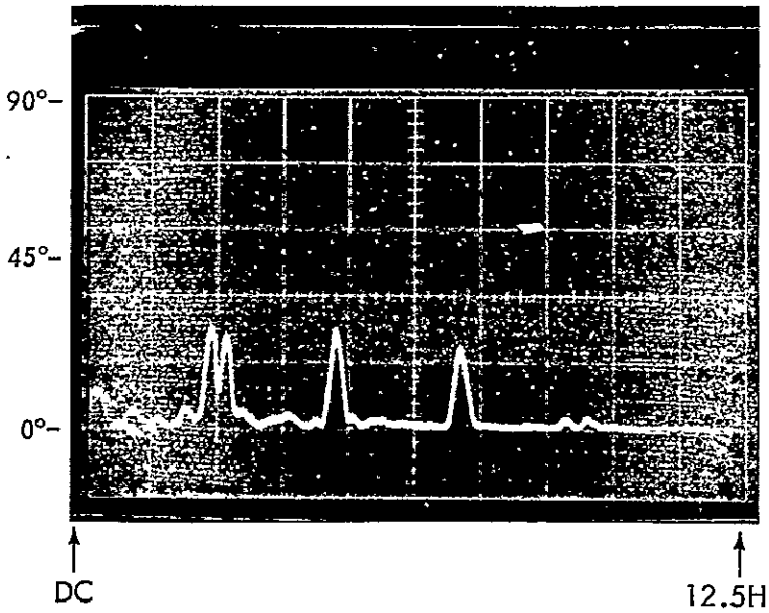

TYPICAL FREQUENCY SPECTRUM OF THE RELATIVE PHASE

Figure 3-15: RELAY 2 Experiment, 900' Antenna Spacing

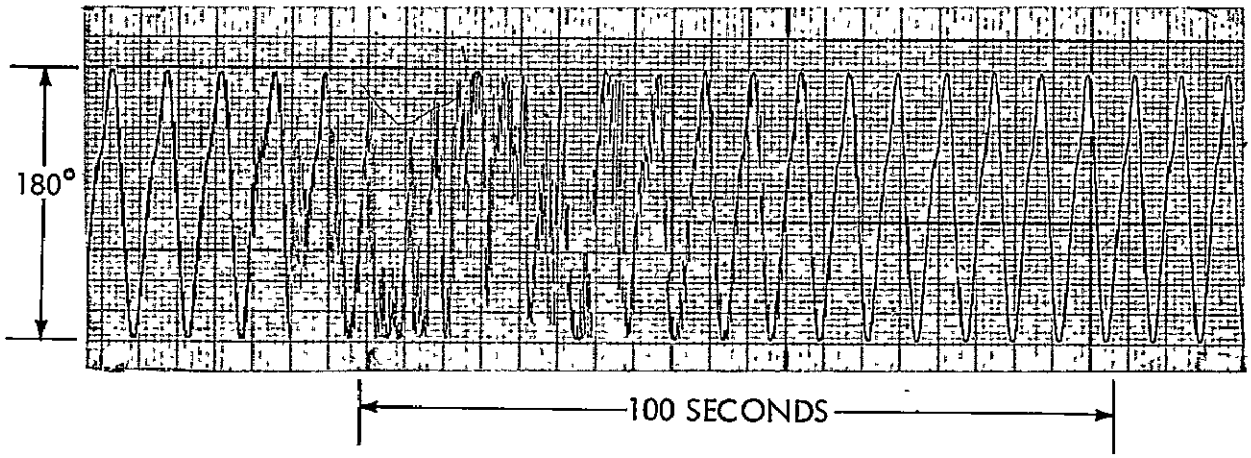

STRIP CHART RECORDING OF RELATIVE PHASE

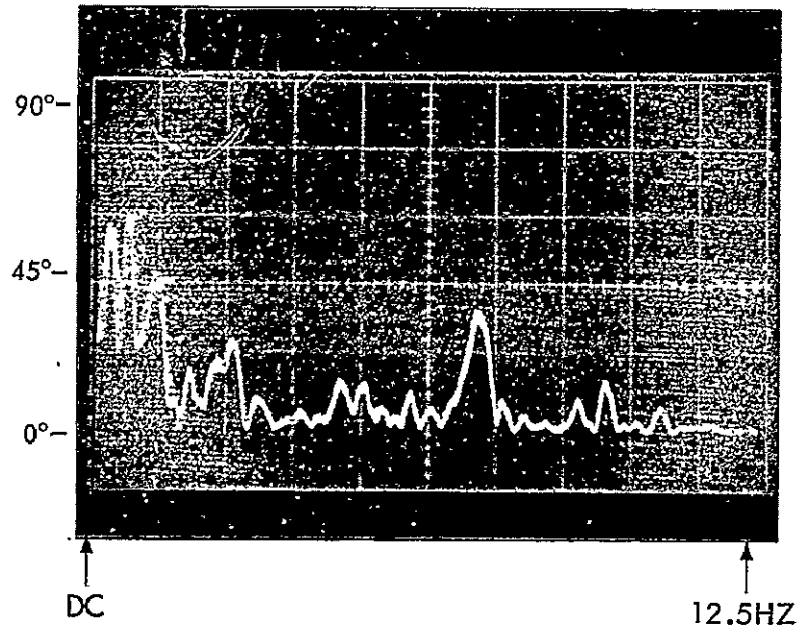

NOT REPRODUCIBLE

TYPICAL FREQUENCY SPECTRUM OF THE RELATIVE PHASE

3.3 S-Band Results

For the S-band experiments, two 15-foot diameter parabolic reflector antennas were used as array elements (Figure 3-17). Each of the two reflectors had an F/D of 0.4 and a surface tolerance of 1/16 inch rms. A five element array of dual polarized, sleeve dipoles was used to feed each reflector. The feed provided three channel monopulse output with remotely selectable RHC and LHC polarization (Figure 3-18). The center element alone was used for the sum channel to provide 7.5 ±1 db feed pattern taper in the principal planes at the edge of the reflector (65° from boresight). Including the 3 db space loss at the reflector edge, the illumination taper on the reflector was 10.5 ±1 db. Figure 3-19 gives the RHC and LHC polarization patterns of the feed for sum and error channels measured with a vertically polarized transmitting source.

A converter/preamplifier was mounted directly behind each feed to downconvert the received 2200-2300 MHz RF to VHF. The output center frequency was 135 MHz with 10 MHz bandwidth. An externally supplied reference signal was frequency selectable in 10 MHz steps to mix any S-band signal within the 100 MHz RF bandwidth down to the 135 ±5 MHz output band. The preamplifier output frequency and bandwidth is compatible with the input requirements of the APDAR receiver. A block diagram of the converter preamplifier is shown in Figure 3-20. Each channel of the converter preamplifier had a minimum gain of 20 db and a noise figure of 6 ±0.5 db. With the exception of the antennas and front end electronics, all the equipment used for the VHF experiments was again used at S-band.

The external reference signal is derived from 10 crystals ranging in frequency from 97.5 MHz to 101.25 MHz. The crystal frequencies are doubled, fed to a power divider and then sent to the two antennas for use in the converter preamplifier. In addition to providing ability to select a given 10 MHz bandwidth, the external reference signal insures that the downconversion process is coherent between antennas. Therefore, the downconverters do not affect relative phase measurements. The converter preamplifiers accept the external reference input of 195 to 202.5 MHz and multiply × 12 in one conversion using step recovery diodes. The 2340 to 2430 MHz output is then used as the L.O. for downconverting the received S-band signals. A simplified block diagram of the entire S-band system is shown in Figure 3-21. The time delay system (within the dotted lines) was only included in the receiver for an evaluation of its effect on receiver performance (Section 2.3). The time delay system was not used during gain improvement or relative phase experiments to eliminate any possibility of affecting the results.

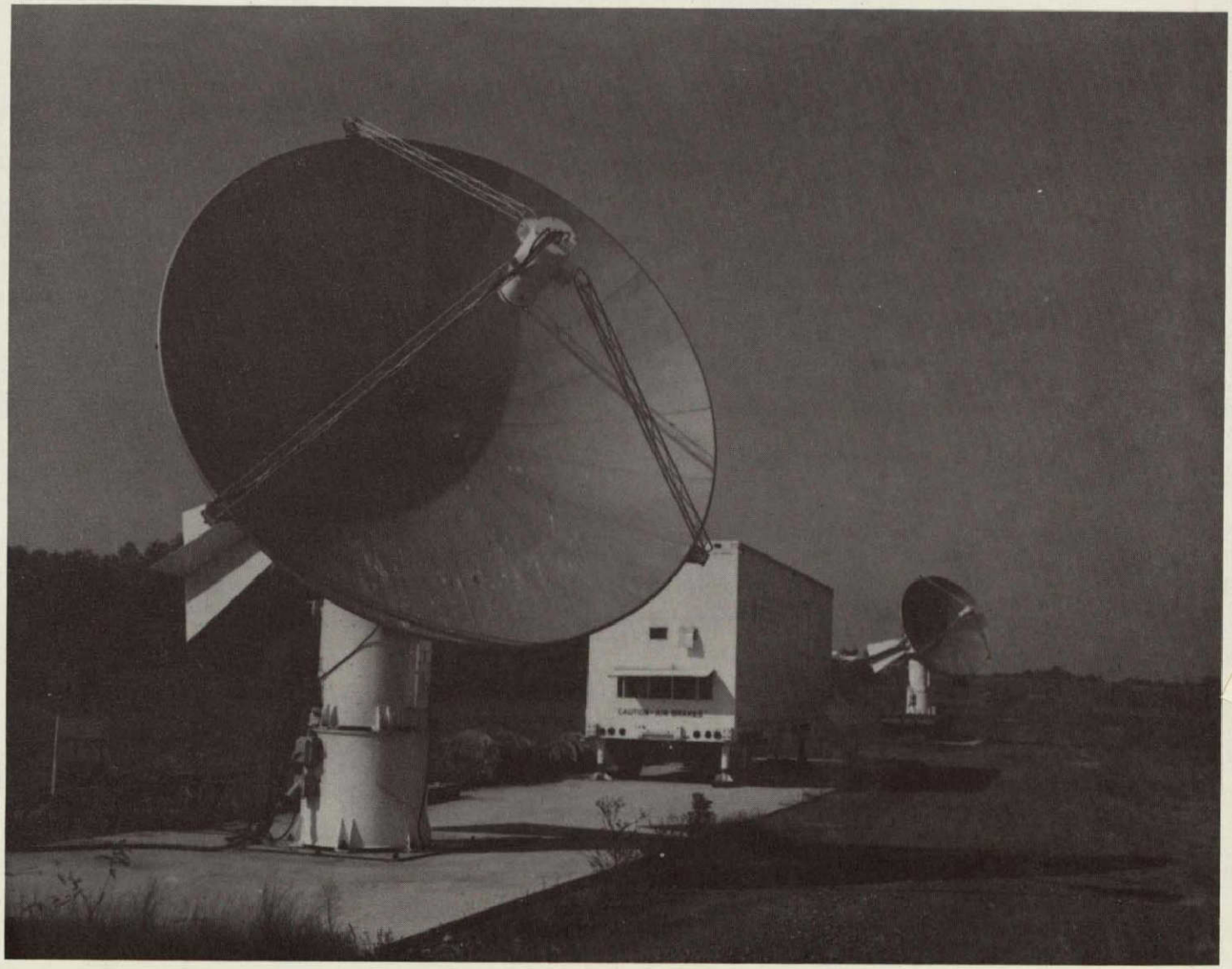

NOT REPRODUCIBLE

Figure 3-17: Two Element Array of 15' Diameter Parabolic Antennas at S-Band

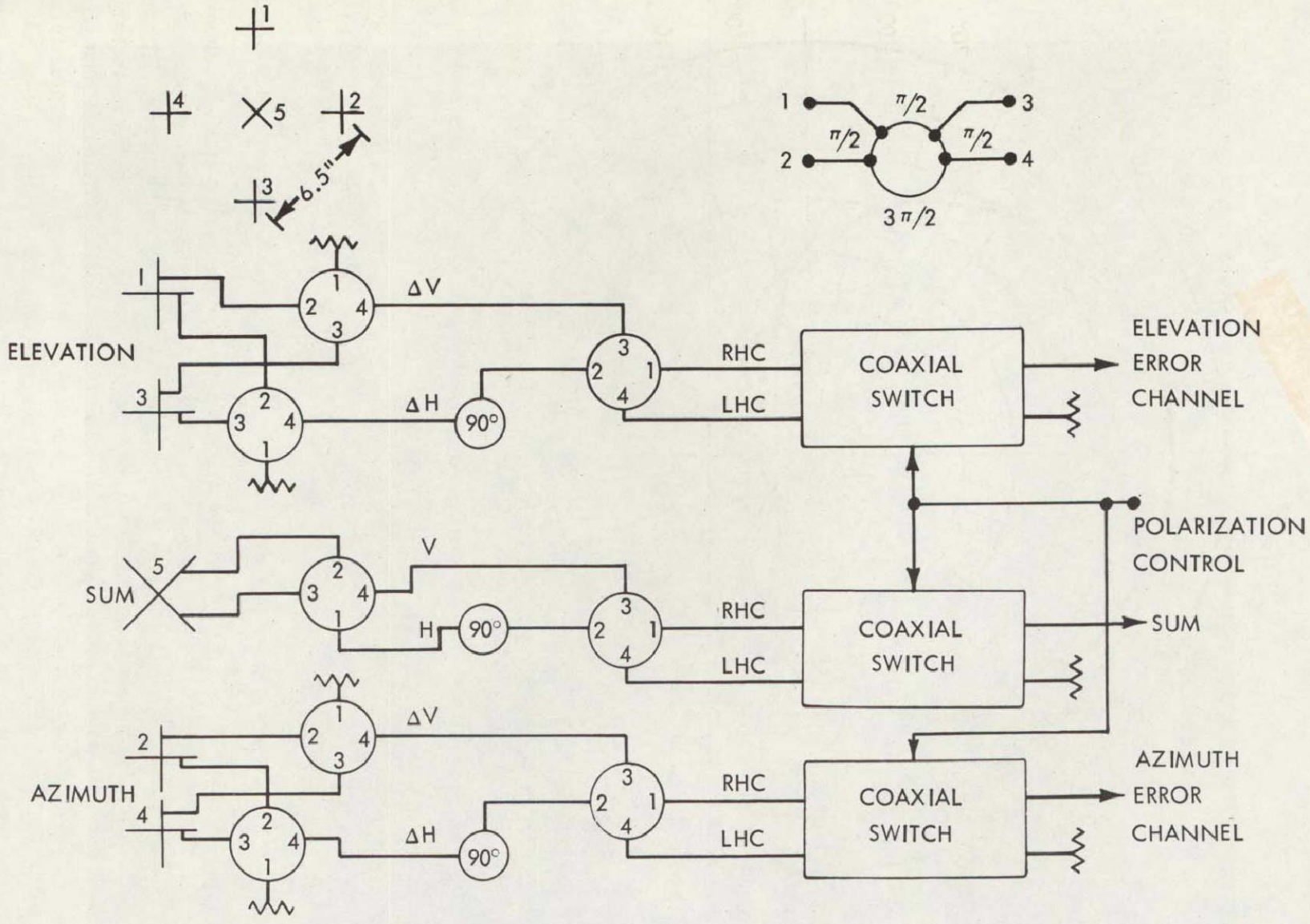

Figure 3-18: Block Diagram of S-Band Feed and Monopulse Network

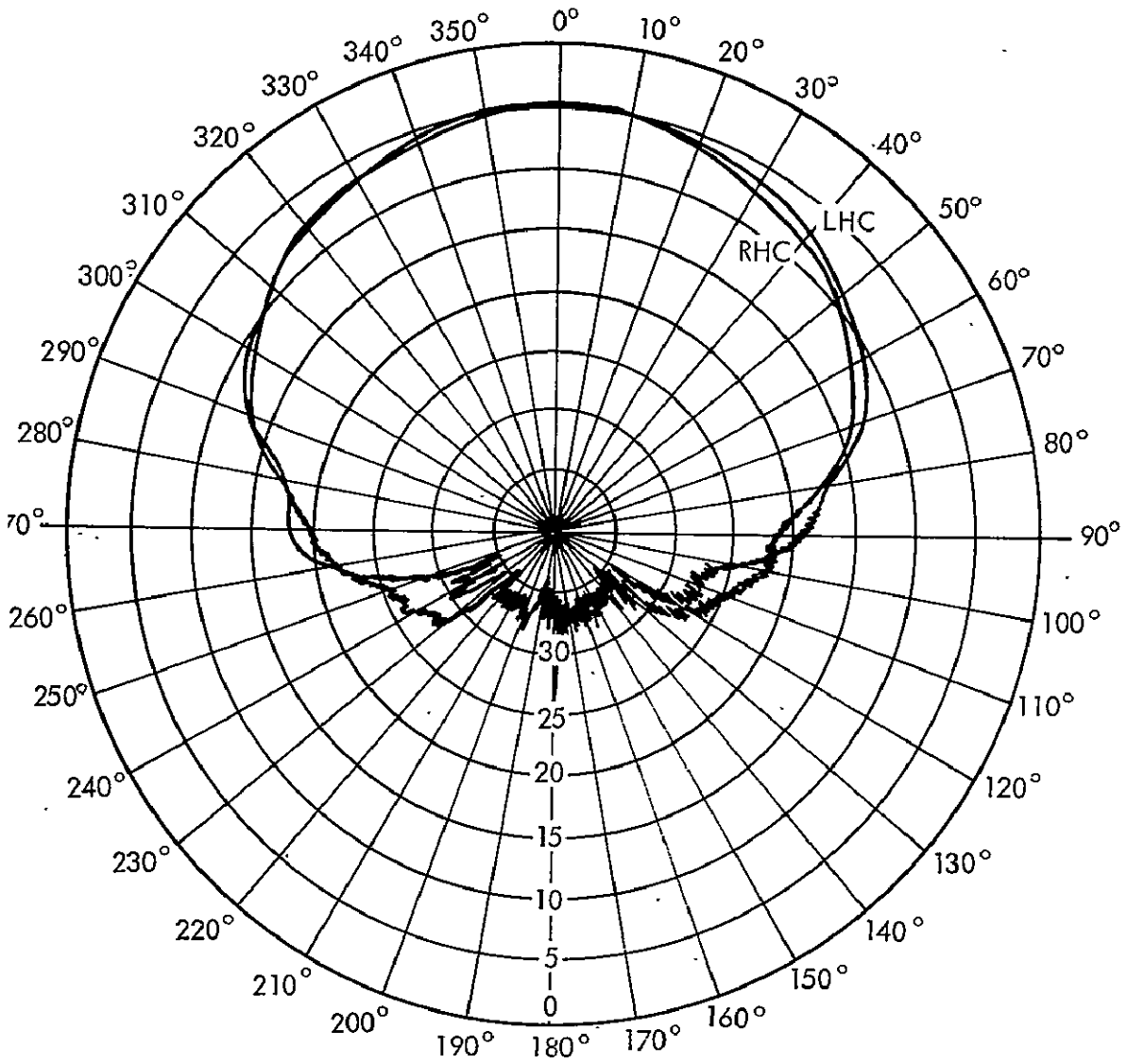

Figure 3-19a: Sum Channel in Azimuth Plane for RHC and LHC Polarization

The 2282.5 MHz downlink from TETR-2 was used to initially checkout the autotrack performance of the system. These tests were conducted over the three month period from September to November 1969. Although TETR-2 was satisfactory for checkout purposes, it was not satisfactory for gain improvement measurements. As discussed previously, the input CNR in each channel must be less than +10 db to permit acceptable measurement of CNR improvement. The received CNR from TETR-2 exceeded +10 db in all cases. The Apollo-12 2287.5 MHz downlink carrier was used for all gain improvement measurements.

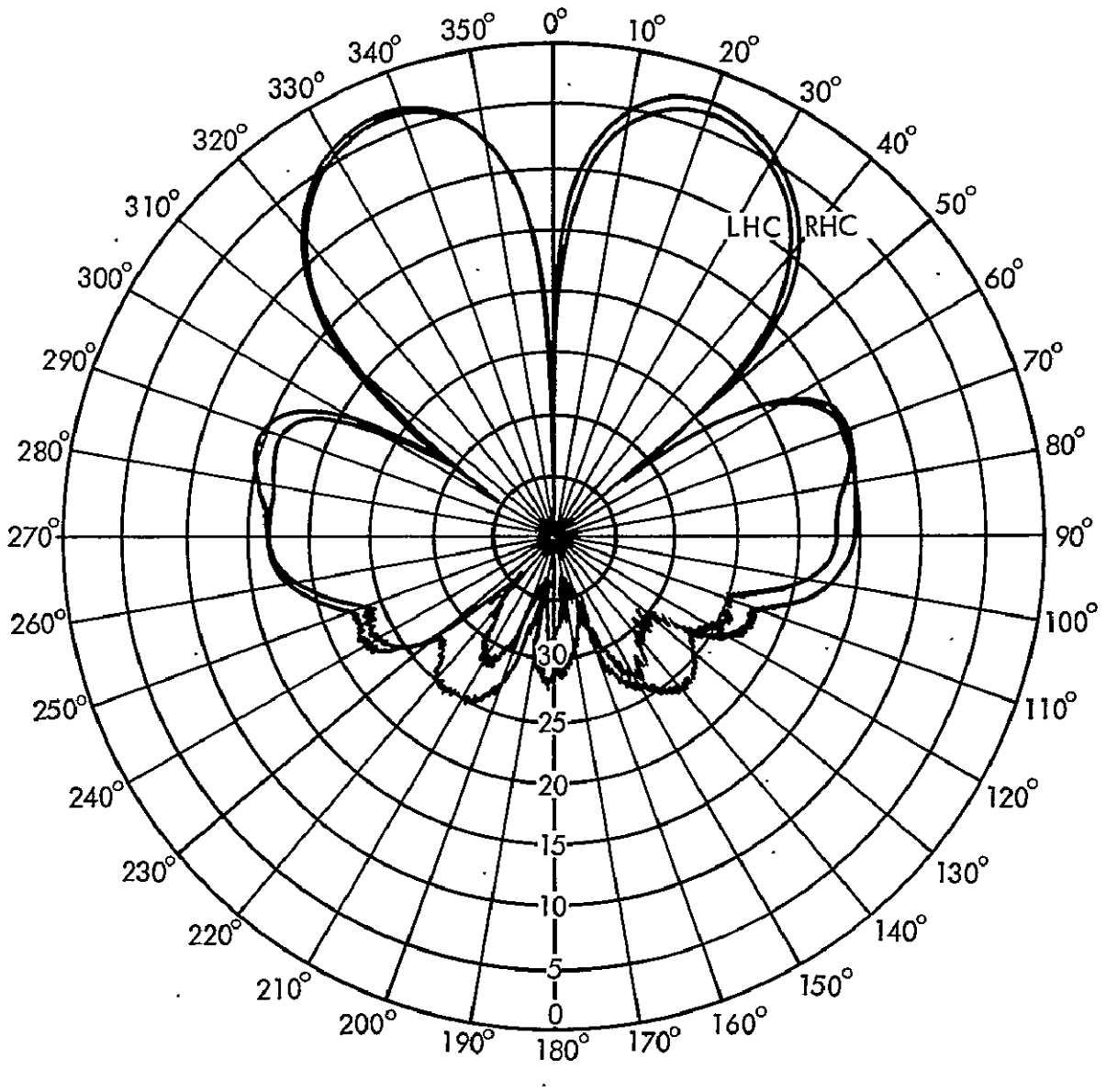

Figure 3-19b: Azimuth Error Channel in Azimuth Plane for RHC and LHC Polarization

The gain improvement distribution shown in Figure 3-22 represents a summary of 5-1/4 hours of continuous measurements while tracking Apollo-12. The measurements were made from 5:45 p.m. to 11:00 p.m. local time on November 14, 1969 while the spacecraft was on its trans-lunar trajectory. During this period the spacecraft was transmitting with its high gain antenna and the received CNR was sufficiently high for the APDAR receiver to maintain phase lock while never exceeding +10 db.

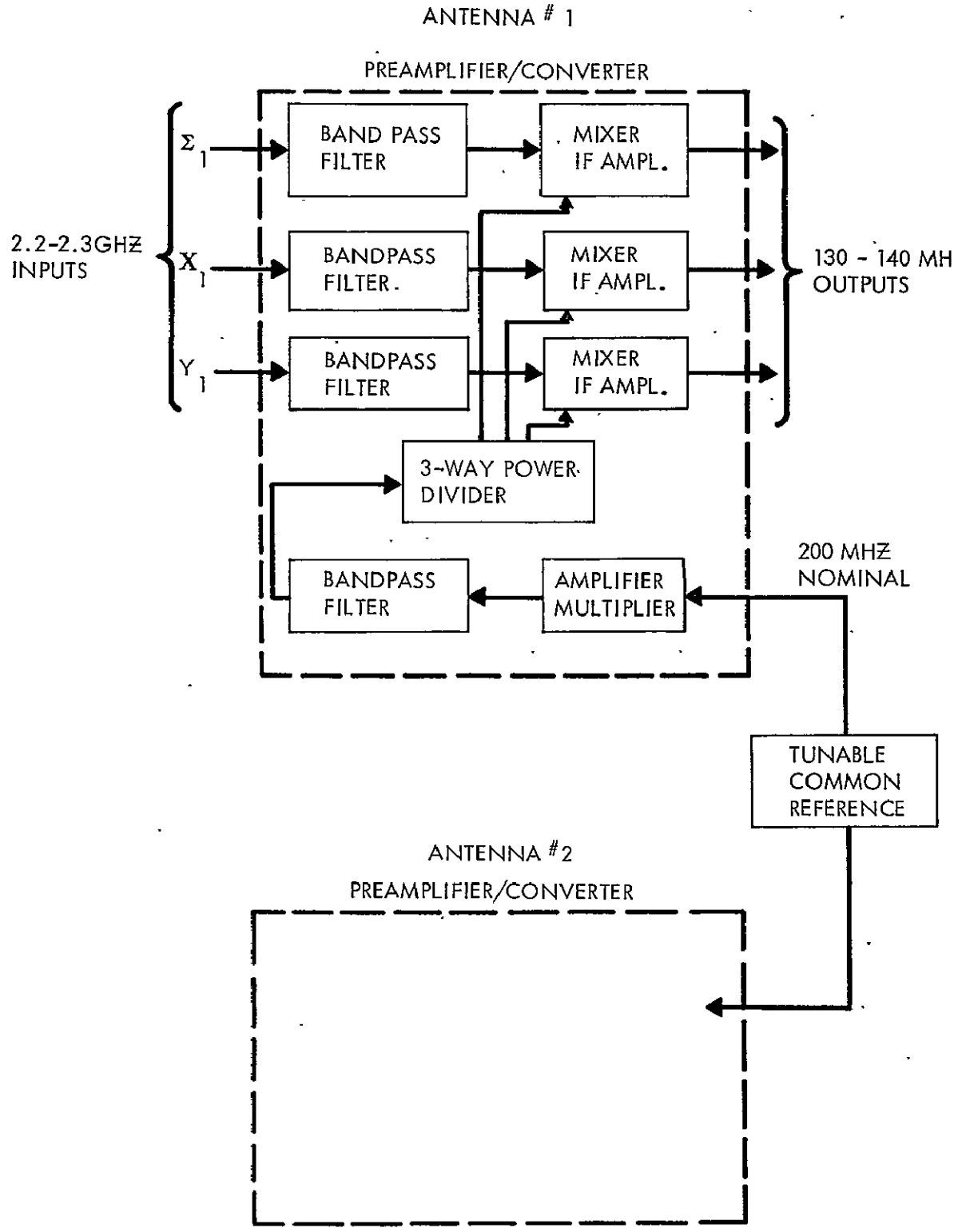

Figure 3-20: Block Diagram of Converter Preamplifier

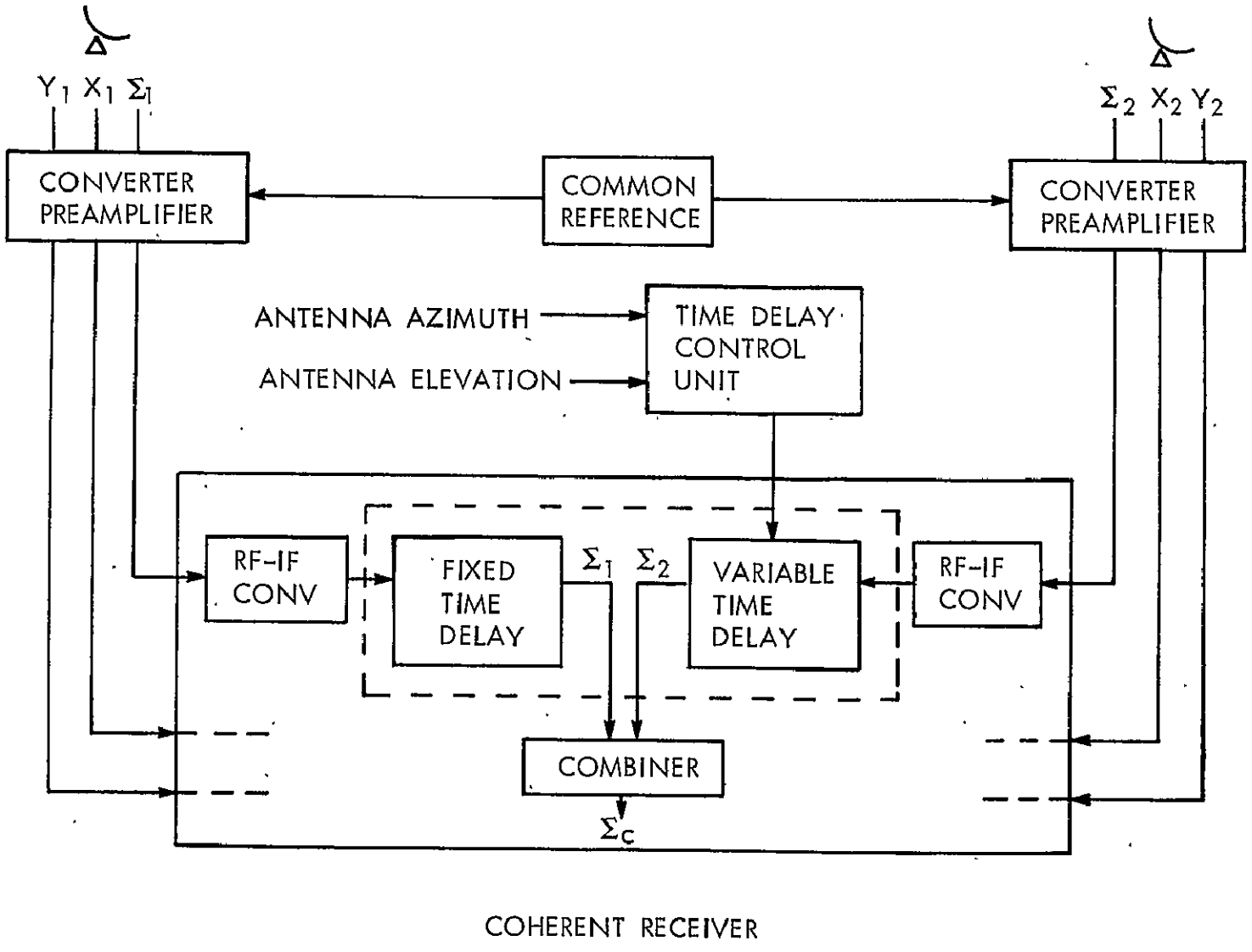

Figure 3-21: Block Diagram of S-Band System

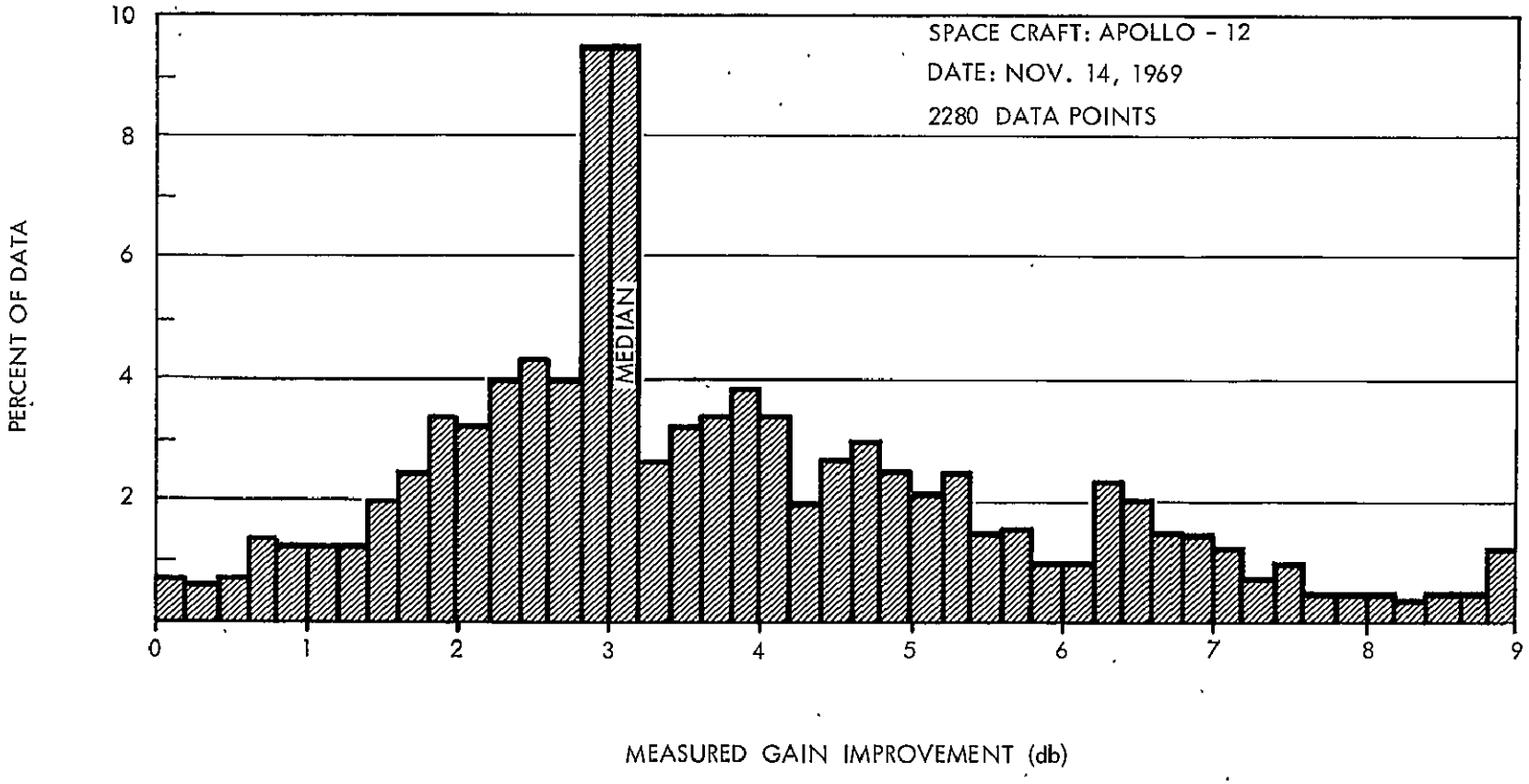

Figure 3-22: Gain Improvement Distribution Over Input Channels

The data used to construct the distribution in Figure 3-22 consisted of all relative measurements of CNR at the output of the receiver to that in each input channel. Since this includes measurements relative to the weaker as well as the stronger channel, the distribution will extend beyond a 3 db improvement limit of the combined output over that in the best input channel. The median of this distribution would be expected to fall at 3 db improvement. The median of the measurements fell within the increment centered at 3.1 db.

The measured data was also analyzed to determine the actual CNR improvement over the best input channel, for any given set of measurements, compared with the theoretical improvement for that set of input conditions. The theoretical improvement is related to the input conditions as shown in Figure 2-18 of Section 2.2.4. This analysis indicated that the measured improvement fell within 0.5 db of the theoretical with 93.1% probability.

The data presented above was measured at a 180-foot antenna separation. The antenna separation was changed to 420 feet for the Apollo-12 return to earth on November 23. Predicted observations for the return flight indicated the spacecraft would be visible continuously for eight hours. However, the high gain antenna was used for only 15 minutes during the entire eight hour observation. As a result, the received carrier was 20 db lower than anticipated and fell below the -130 dbm threshold level of the APDAR receiver. No gain improvement measurement data was taken on the return flight of Apollo-12.

While the received carrier levels of -110 to -120 dbm from Apollo-12 on November 14 were compatible with the CNR measurement technique, it was too low for relative phase measurement. At these levels, the internally generated phase noise of the receiver exceeded the desired phase components. As a result, the relative phase recorded on magnetic tape could not be used to reproduce the actual phase front distortion.

4 SUMMARY

The gain improvement measurements using ATS-C as the transmitting source at VHF were within 0.5 db of theoretical expectations 90% of the time. At S-band, using Apollo-12 as the source, 93.1% of the gain improvement results were within 0.5 db of the theoretical values. Gain improvement was measured by comparing the CNR at the output of the combiner to that at the input channels. Assuming ±0.25 db accuracy on each CNR measurement, the gain improvement results are accurate to ±0.5 db.

The digital time delay system developed for this program is capable of correcting for time of arrival delay between a two element array with up to 2800' spacing to that of an array at 50' spacing with no delay correction. The time delay system provides 2 MHz instantaneous bandwidth with less than 0.5 db loss at band edge for array spacings up to 2800'. Tests have indicated that the time delay system does not significantly affect either the amplitude or phase performance of the APDAR receiver.

These experiments have demonstrated the operational feasibility of large aperture arrays for gain improvement. Although the time delay system developed and tested in this program extended the array bandwidth to 2 MHz (0.5 db loss at band edge and up to 2800' antenna spacing), the only limiting factor on bandwidth extension is the accuracy in determining the angular position of the spacecraft relative to the receiving antennas.

PRECEDING PAGE BLANK NOT FILMED

Appendix A: Economics of Arrays

A recent survey of the state of the art in gain limited antennas [15] indicates that the rms surface accuracy (σ) and reflector diameter (D) are related by

$$\sigma = 10^{-4.6} D \qquad \text{(A-1)}$$

as shown in Figure A-1. The curves plotted in Figure A-2 represent the maximum gain versus diameter defined by Equation A-1 at 2, 6, 10, 15 and 30 GHz. The gain limitation of single aperture antennas is clearly shown for each frequency with the exception of 2 GHz. The feasibility of constructing a single aperture antenna to achieve a required gain is dependent on the state of the art (Figure A-2) and on the cost relative to arrays of smaller aperture antennas.

The cost model for large reflector antennas was constructed by Bell Telephone Laboratories (BTL) recently, under contract to GSFC [16]. The model for exposed reflector antennas is given by

$$C_o = a_1 D^{-1/3} \exp D/45 \qquad \text{(A-2)}$$

where

C_o = cost in dollars

D = reflector diameter in feet

$a_1 = 6.7 \times 10^5$

In determining their cost model, BTL was careful to use only antennas with well established surface accuracies and costs. Three antennas were chosen (Aerospace 15-foot mm antenna, NRL 85-foot antenna and JPL 210-foot antenna) and Equation A-2 was found to connect each point.

BTL's survey of the state of the art in reflector antennas indicated surface accuracy and diameter related as

$$\sigma = 10^{-5.37} D^{3/2} \qquad \text{(A-3)}$$

The relation between surface accuracy and diameter is a major factor in determining cost (Equation A-2). BTL therefore modified its cost model to include a quality factor which would permit changing the ratio of σ to D.

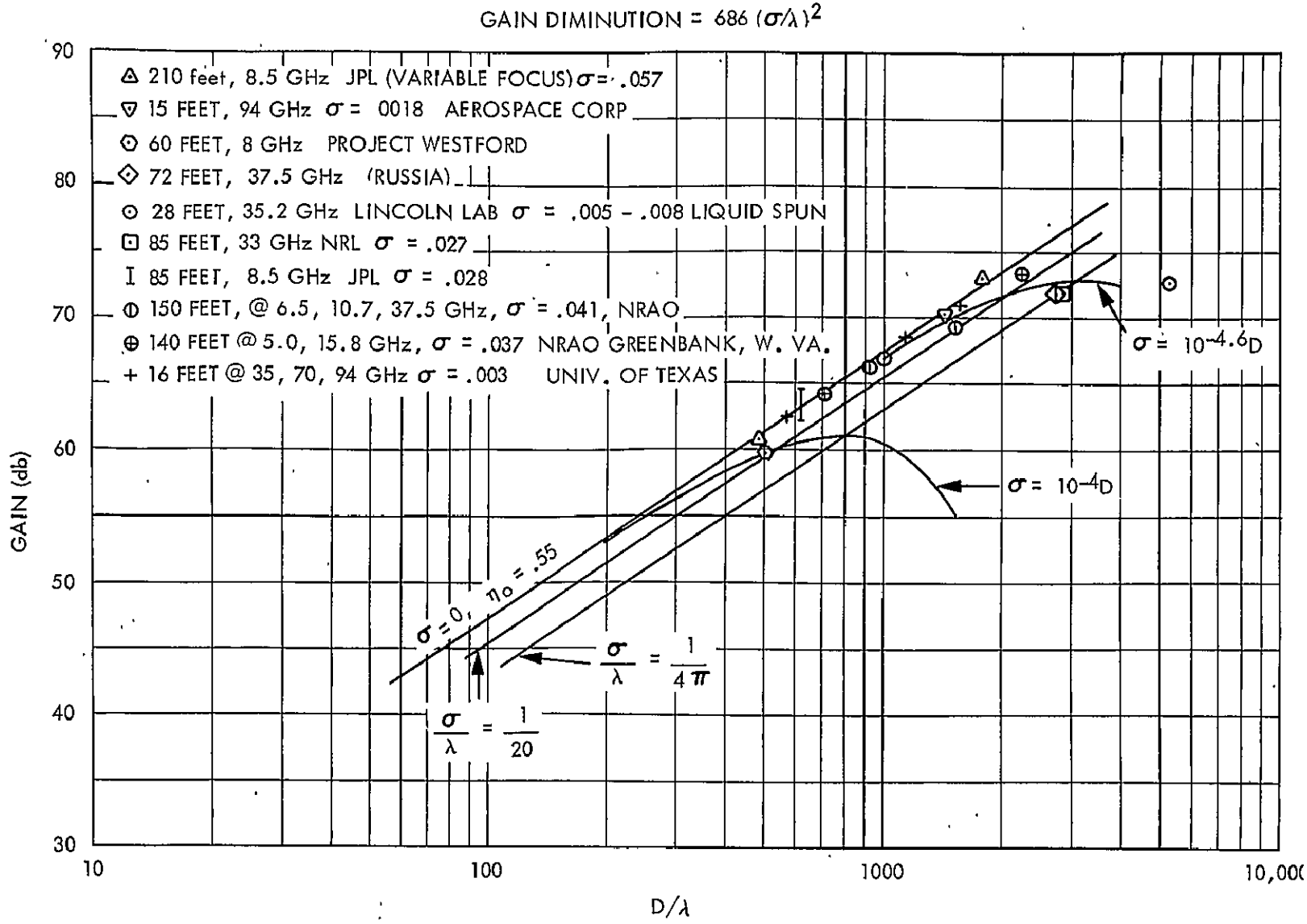

Figure A-1: Antenna Gain vs. Surface Tolerance (Reference 15)

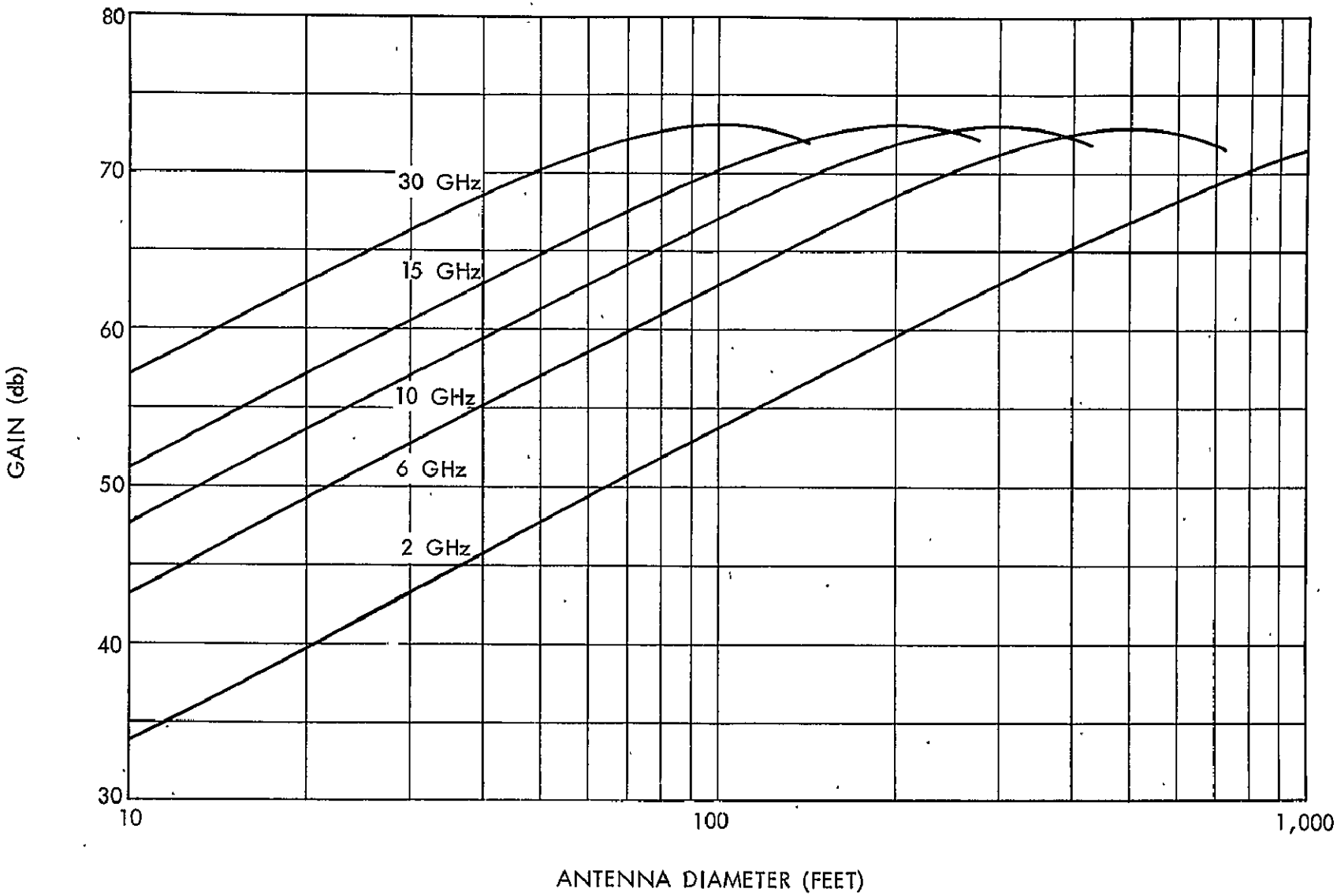

Figure A-2: State of the Art Gain vs. Antenna Diameter for 2, 6, 10, and 30 GHz

The idea of a quality factor was first introduced by Stack [17]. Stack assumed an inverse relationship between fractional reductions in surface tolerance (σ) and fractional increases in total cost. The physical limitations in reducing surface tolerance even with substantial increases in cost would indicate an exponential relationship between fractional changes in σ to fractional changes in cost. BTL therefore assumed the improvements in σ/D would effect surface tolerance as

$$\sigma = \sigma_o\left(\frac{1}{X}\right)$$

and cost as

$$C = C_o \exp (X - 1)$$

where

σ_o = surface tolerance given by Equation A-3

C_o = antenna cost given by Equation A-2

X = quality factor

σ = improved surface tolerance

C = antenna costs with improved surface

The new BTL cost model, including the quality factor (X), is given by

$$C = a_2 D^{-1/3} \exp (a_3 D + X - 1) \qquad \text{(A-4)}$$

where

$$a_2 = 6.7 \times 10^6$$

$$a_3 = 2.22 \times 10^{-2}$$

The analysis that follows will assume that σ and D are related as in Equation A-1 with a quality factor of

$$X = 10^{-0.77 D^{1/2}} \qquad \text{(A-5)}$$

The cost given by Equation A-4 includes reflector, support structure, pedestal, feed and control system. Fixed electronics costs for the station will not be considered in comparing single apertures versus arrays. Only the cost of additional electronics in an array will be considered. The costs of additional electronics per additional array element will be assumed 100K for all frequencies. A sample itemization is given below.

Additional Front End Equipment	$ 50K
Additional Receiver Channel	30K
Additional Time Delay Channel	20K
Total Cost per Additional Array Element	$100K

The cost of an array of smaller aperture antennas for achieving equivalent gain to that of a single large reflector is given in Equation A-5

$$C_A = (0.95)^{\log_2 N}\left[NC_E + (N - 1)\, C_D\right] \qquad \text{(A-5)}$$

where

N = number of array elements

C_E = cost of each antenna in the array

C_D = incremental electronics costs, $100K

C_A = total array cost

The term $(0.95)^{\log_2 N}$ is the learning factor of constructing N identical elements. A 0.95 learning coefficient has consistently been used in cost estimations of antenna arrays [18, 19]. Although cost reductions in array elements can be made if the array will always operate as a unit [20], the assumption of identical array elements has been made in this analysis to preserve the inherent multi-beam capability of the array.

The cost of an array element (C_E) is determined by the required element gain. The element gain is calculated from the total array gain by

$$G_E = G_A - 10 \log_{10} N + \ell$$

where

G_A = total array gain required, db

G_E = gain required for each array element (db)

ℓ = loss in combining the array elements, 0.5 db

The element diameter is now read off Figure A-2 and used in Equation A-4 to compute the element cost (C_E).

A comparison between single aperture antennas and arrays must be done on the basis of total costs. Maintenance and operation and electronics replacement costs must also be considered. For this analysis, a yearly electronics replacement cost of 10% of initial equipment investment is assumed [21]. Since electronics costs are normalized to that for the single aperture, there is no electronics replacement cost for the single antenna and 10% of \$100K or \$10K per year per additional array element for the array. A recent study of STADAN operation costs [22] has determined M&O to be 25% of initial antenna investment per year. Costs presented for both the single aperture and array will include a yearly M&O cost of 25% of initial antenna construction cost.

Based upon the analysis presented up to this point, the cost of construction and operation of a single aperture and several array sizes over a 10 year period were calculated. The results are shown in Figures A-3 through A-7 for frequencies of 2, 6, 10, 15 and 30 GHz, respectively. In each case, there is a point at which the array becomes less costly than the single aperture antenna. It is important to remember that a σ/D of $10^{-4.6}$ was assumed in all cases. This assumption was made since it represents the present state of the art and gain maximization is desired. Constructing reflectors for a σ/D of $10^{-4.6}$ will not represent the most effective decision at the lower frequencies where a greater surface tolerance is sufficient. Figures A-3 through A-7 are intended to illustrate the relative advantages of arrays over single aperture antennas for a σ/D of $10^{-4.6}$ only.

Electronics Communications, Inc. (ECI) had made a cost analysis of arrays for GSFC several years ago [23]. The cost analysis presented in this section was performed because the ECI report was based upon an outdated state of art in reflector antennas and because ECI had assumed a 2% yearly M&O cost as opposed to the 25% figure determined from current experience [22].

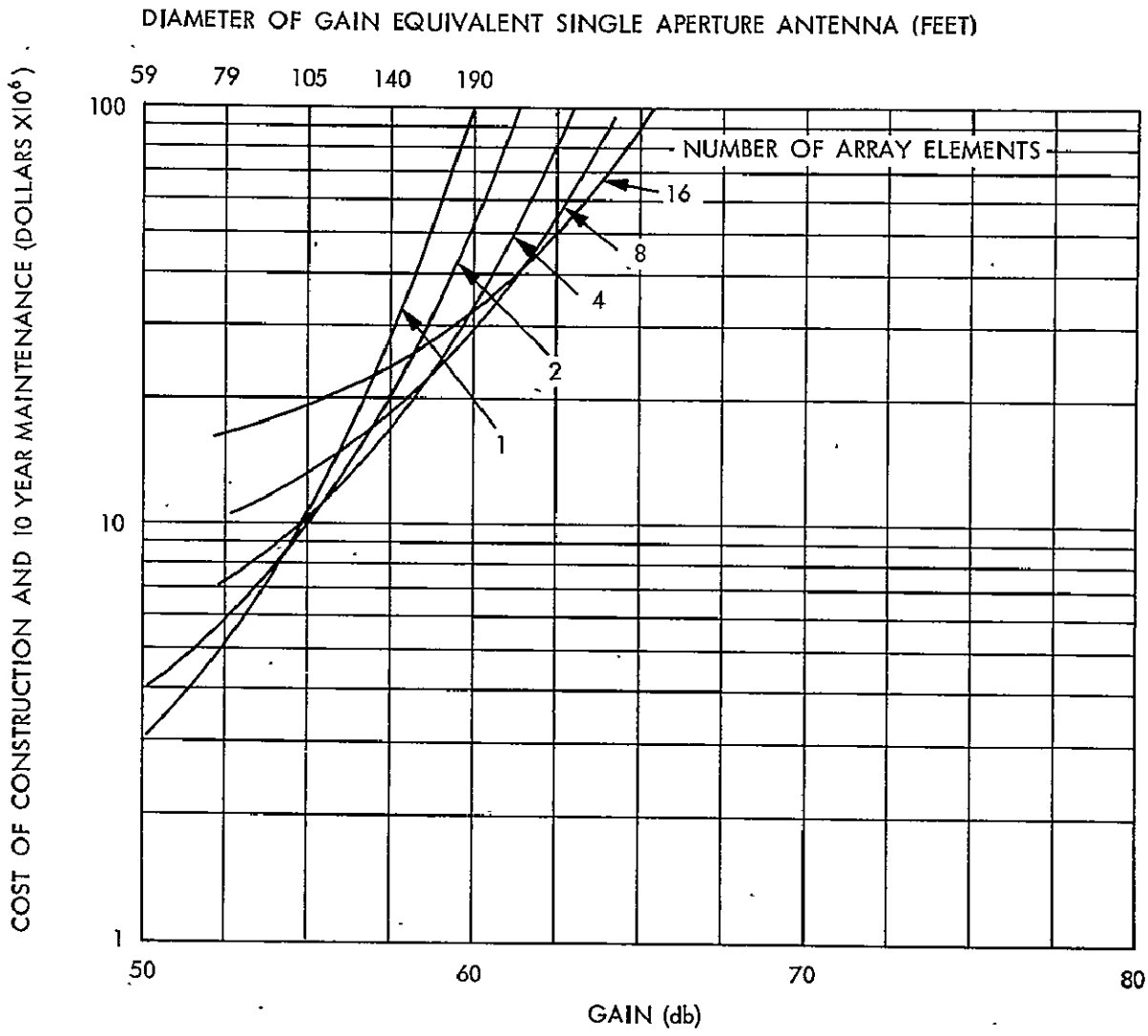

Figure A-3: Cost of Construction and 10 Year Maintenance of Several Array Sizes vs. Gain at 2 GHz

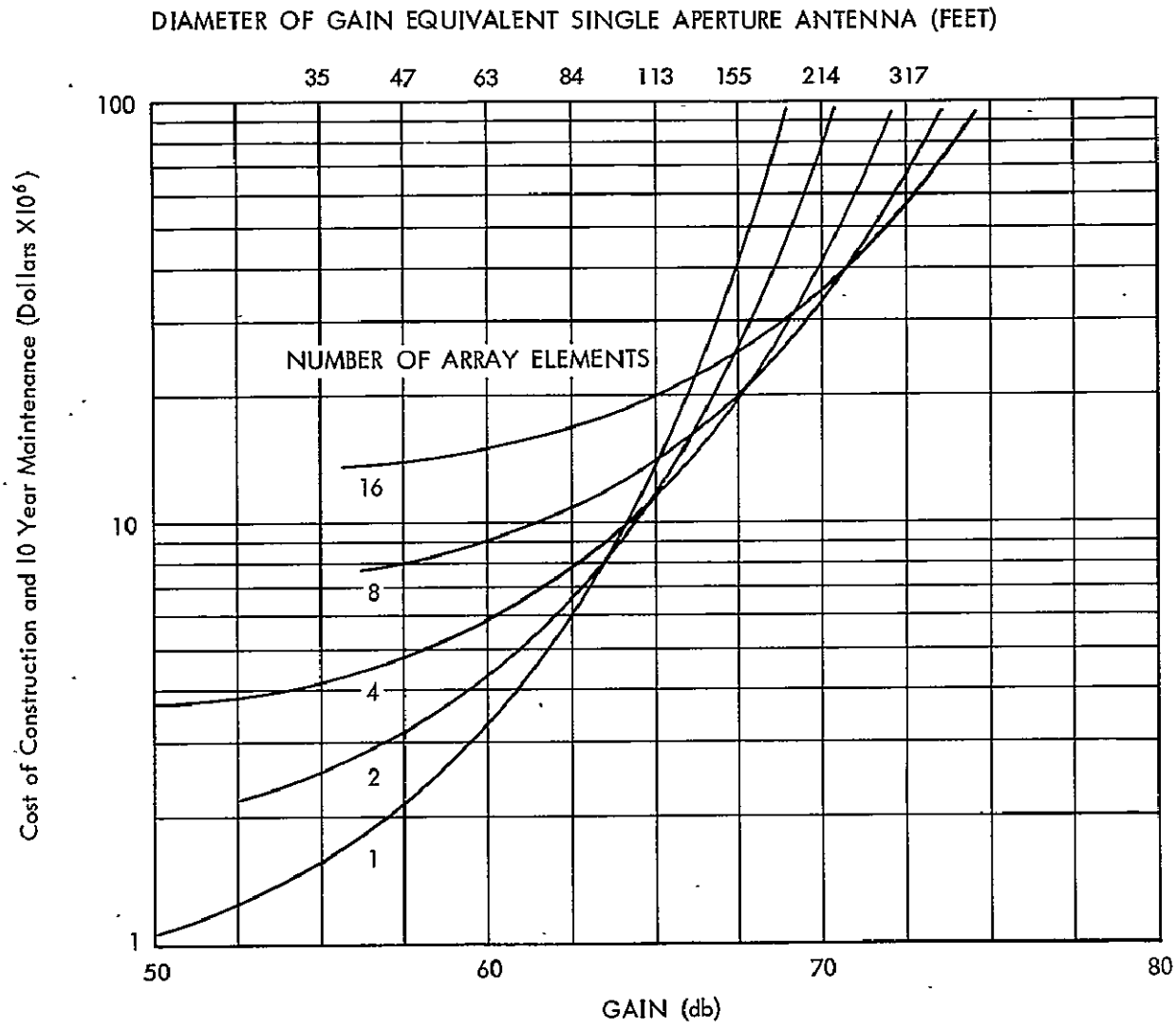

Figure A-4: Cost of Construction and 10 Year Maintenance of Several Array Sizes at 6 GHz

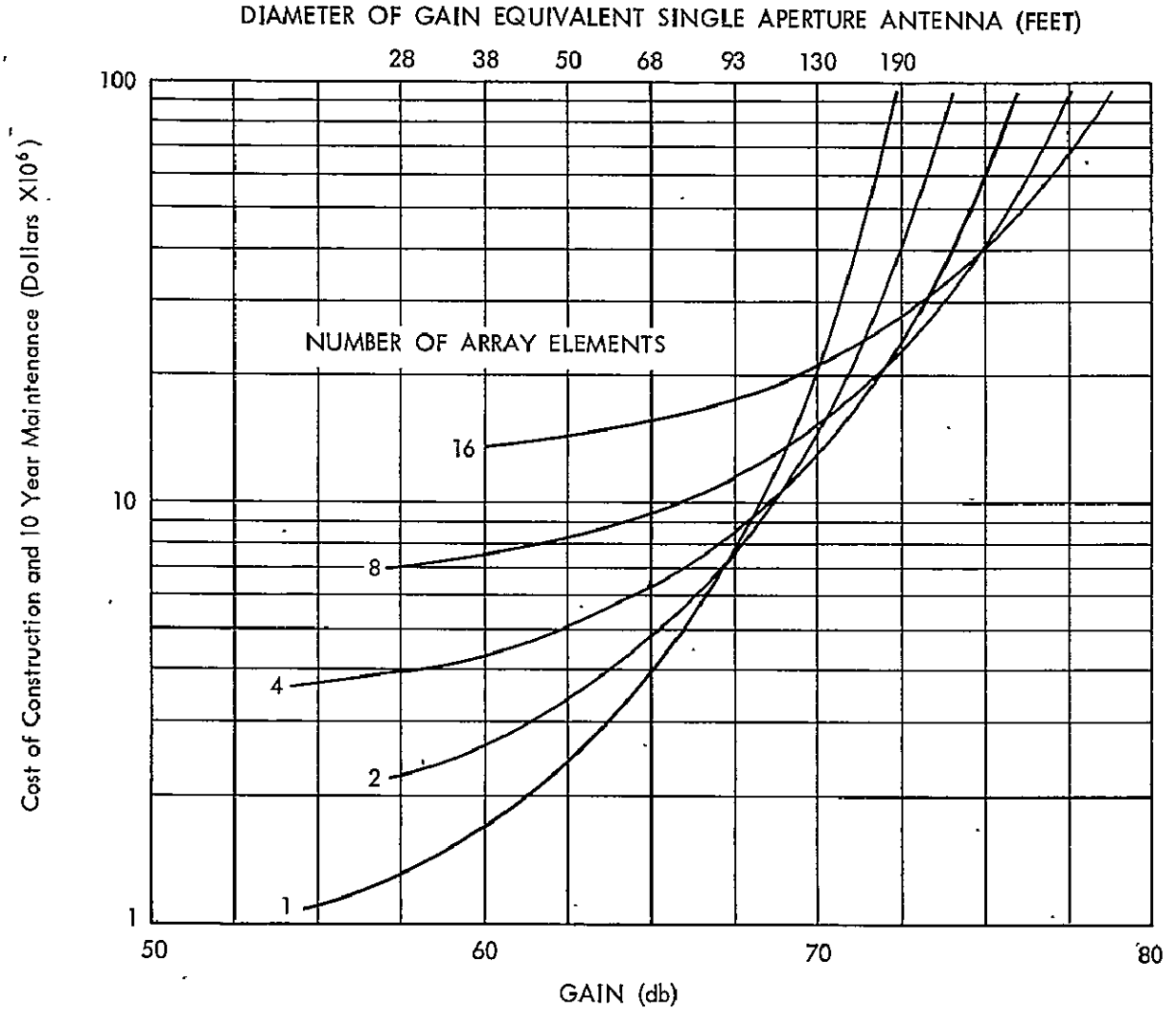

Figure A-5: Cost of Construction and 10 Year Maintenance of Several Array Sizes at 10 GHz

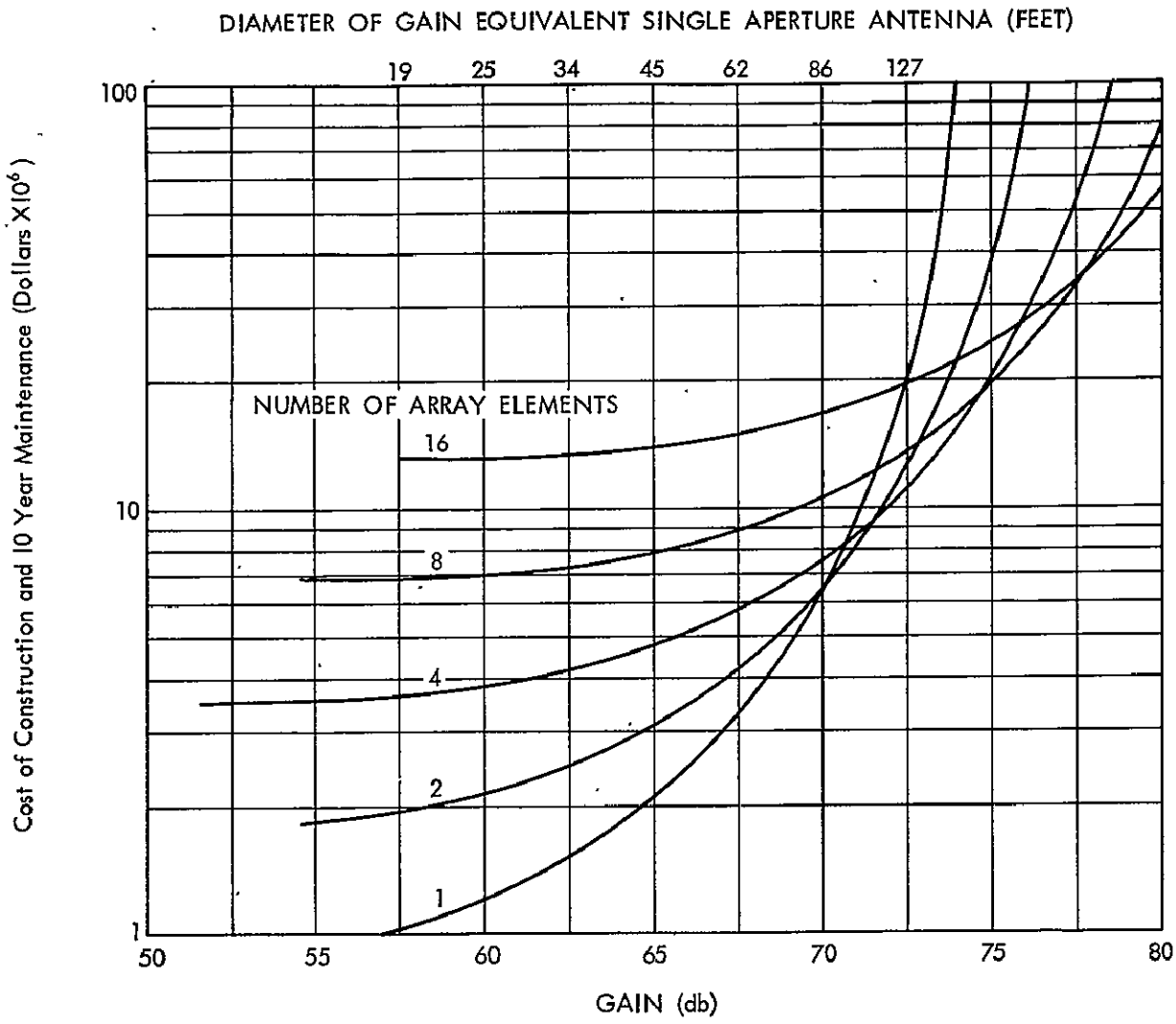

Figure A-6: Cost of Construction and 10 Year Maintenance of Several Array Sizes at 15 GHz

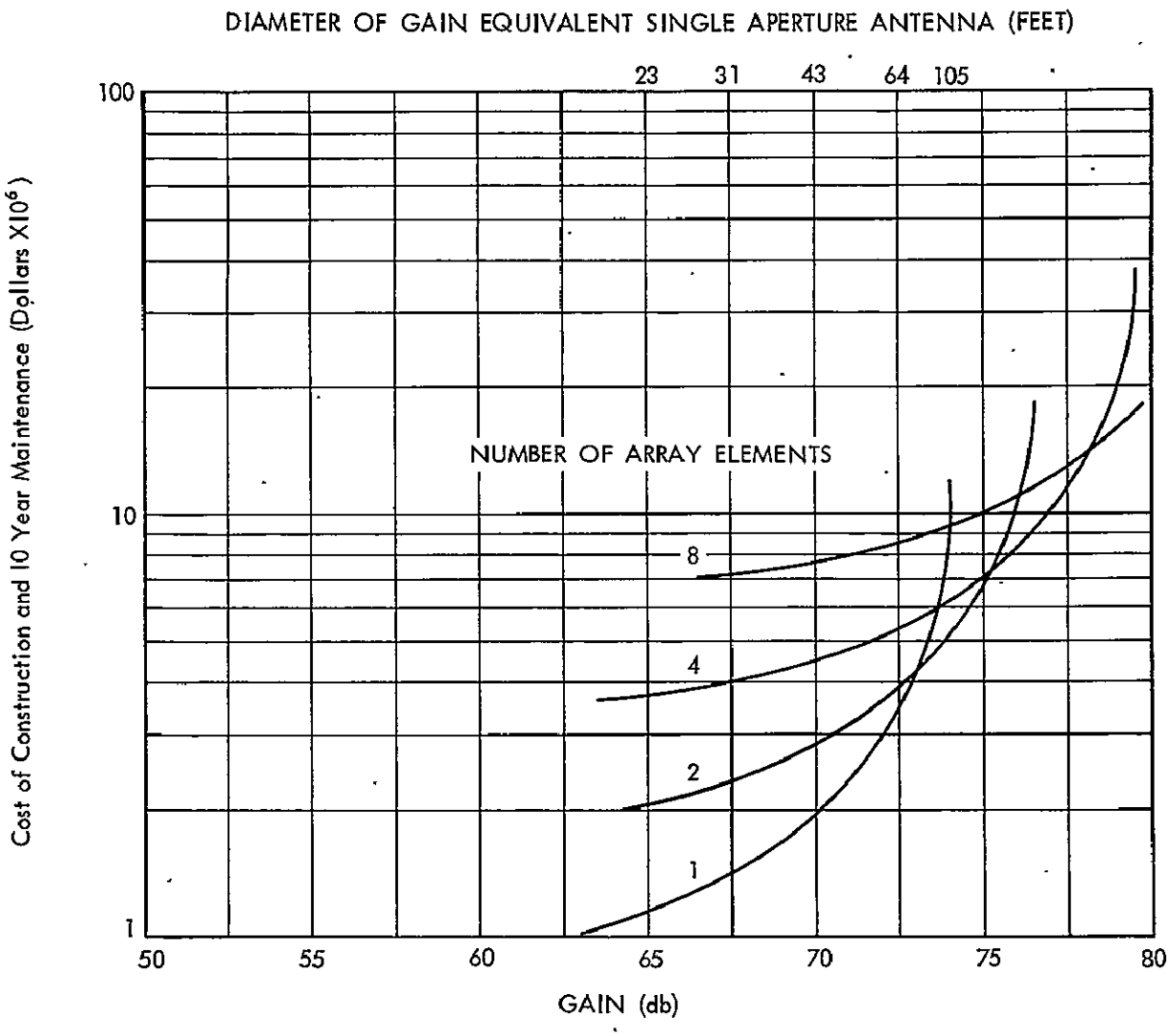

Figure A-7: Cost of Construction and 10 Year Maintenance of Several Array Sizes at 30 GHz

PRECEDING PAGE BLANK NOT FILMED

Appendix B: Phase Front Distortion

In addition to the gain limitation imposed by surface tolerance (Appendix A) antenna gain is also dependent on the amount of phase front distortion across the antenna aperture caused by transmission through the atmosphere. Phase front distortion is a function of frequency, antenna size and local environmental conditions. The total phase front distortion can be described statistically by considering separately a single ray path through the atmosphere, the correlation between ray paths, and the fluctuation in angle of arrival.

A thorough review of phase front distortion was compiled by the Stanford Research Institute [24] under contract to NASA. In this report, the contributions to phase front distortion by the troposphere and by the ionosphere are considered separately because of their distinct relation to frequency.

Troposphere:

The single ray path characteristics are related to frequency and elevation as given below [25]

$$\sigma_t = 7.5\ F\ \csc^{1/2}(\phi) \qquad \text{(B-1)}$$

where

F = frequency, GHz

ϕ = angle between ray and earth surface at receiving point

σ_t = rms phase deviation of a single point on a phase front, mean equal to zero (milliradians)

when $\phi \geq 3°$. The fluctuation in angle of arrival or tilting of the mean phase front also contributes to the total phase front distortion across the aperture. The angle of arrival fluctuation is given by

$$\sigma_\beta = 0.01\ \csc^{1/2}\phi \quad \text{milliradians} \qquad \text{(B-2)}$$

and is independent of frequency. The value of σ_β does not exceed 0.01 radians and its contribution to gain loss is insignificant for antennas with $BW_{3\,db} \geq 0.02°$.

The effect of phase front distortion on antenna gain requires a statistical model of that distortion over the antenna aperture. Only single ray path statistics were considered in Equation B-1. The correlation between ray paths provides the information required for a complete description of the phase front distortion over the antenna aperture. The correlation function is assumed related to antenna diameter by a normal curve of error with 50% correlation determined by experiment to be approximately 200 feet [3]. The 50% correlation distance of 200 feet is a nominal value, individual measurements can vary from 50 to 1,000 feet.

The single ray path rms phase deviation (σ_t) and the correlation function combine to give the mean square phase front distortion over the antenna aperture by the equation [26]

$$\overline{\Delta\alpha^2} = 2\,\sigma_t^2\,[1 - C_\alpha] \qquad \text{(B-3)}$$

where

$\Delta\alpha$ = instantaneous phase deviation of a single point on the phase front from a plane

C_α = correlation coefficient for antenna diameter D

Ruze has developed an equation for gain loss as a function of mean square surface deviations of a parabolic reflector [27]. Assuming that this expression approximates the gain loss due to phase front distortions, the gain reduction of the antenna as a function of $\Delta\alpha^2$ can be expressed as

$$\frac{G}{G_o} = 1 - \overline{\Delta\alpha^2} \qquad \text{(B-4)}$$

where

G_o = antenna gain, no phase front distortion

G = actual gain

Figures B-1 through B-4 indicate the gain loss of a single aperture antenna as a function of antenna diameter at 6, 10, 15 and 30 GHz for several elevation angles. Ruze's gain reduction equation is true for small phase deviations only $\left(\frac{G}{G_o} > 0.5\right)$ and therefore the gain reduction is not shown beyond 3 db in the illustrations.

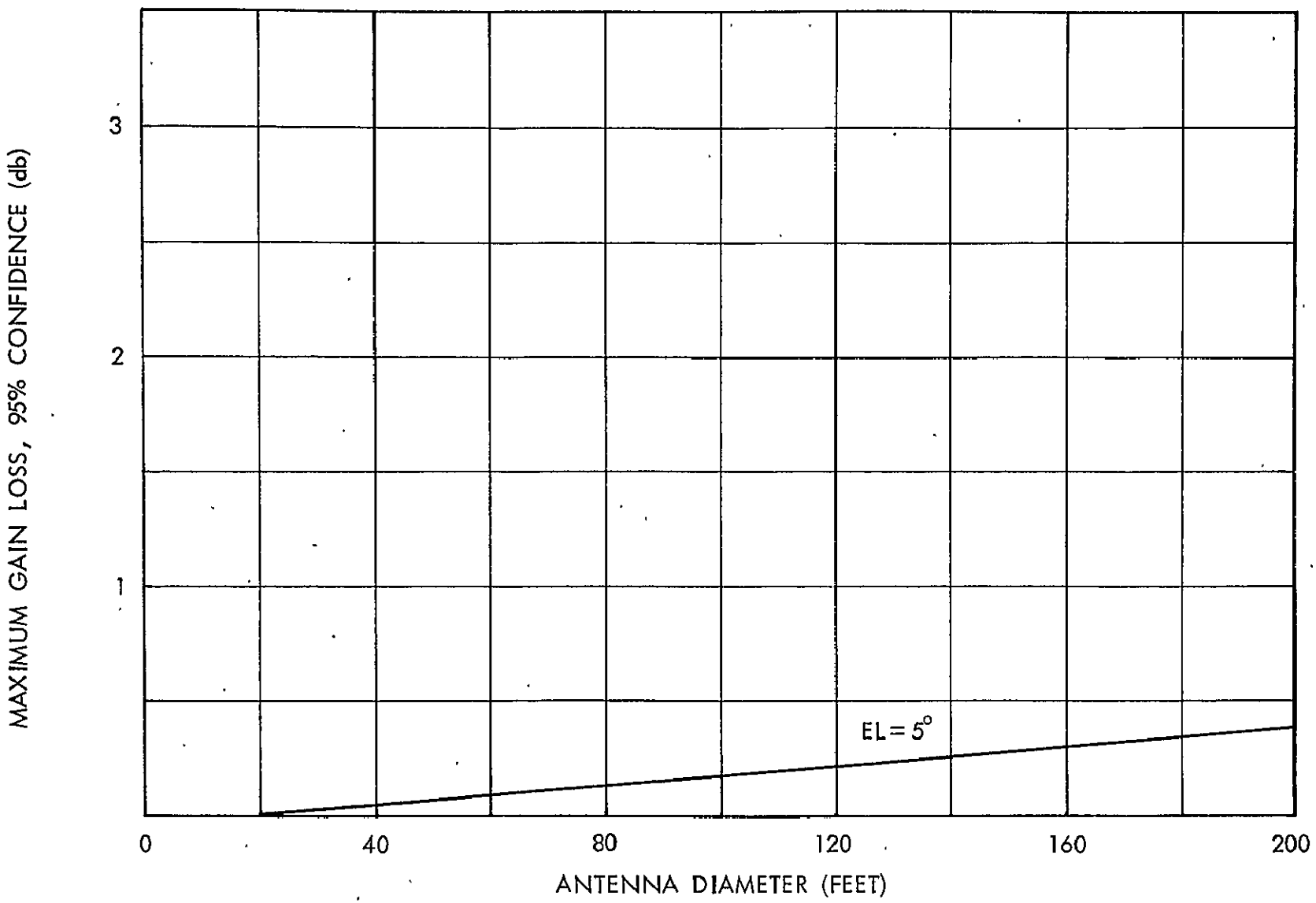

Figure B-1: Maximum Gain Loss vs. Antenna Diameter for Tropospheric Phase Front Distortion, F = 6 GHz

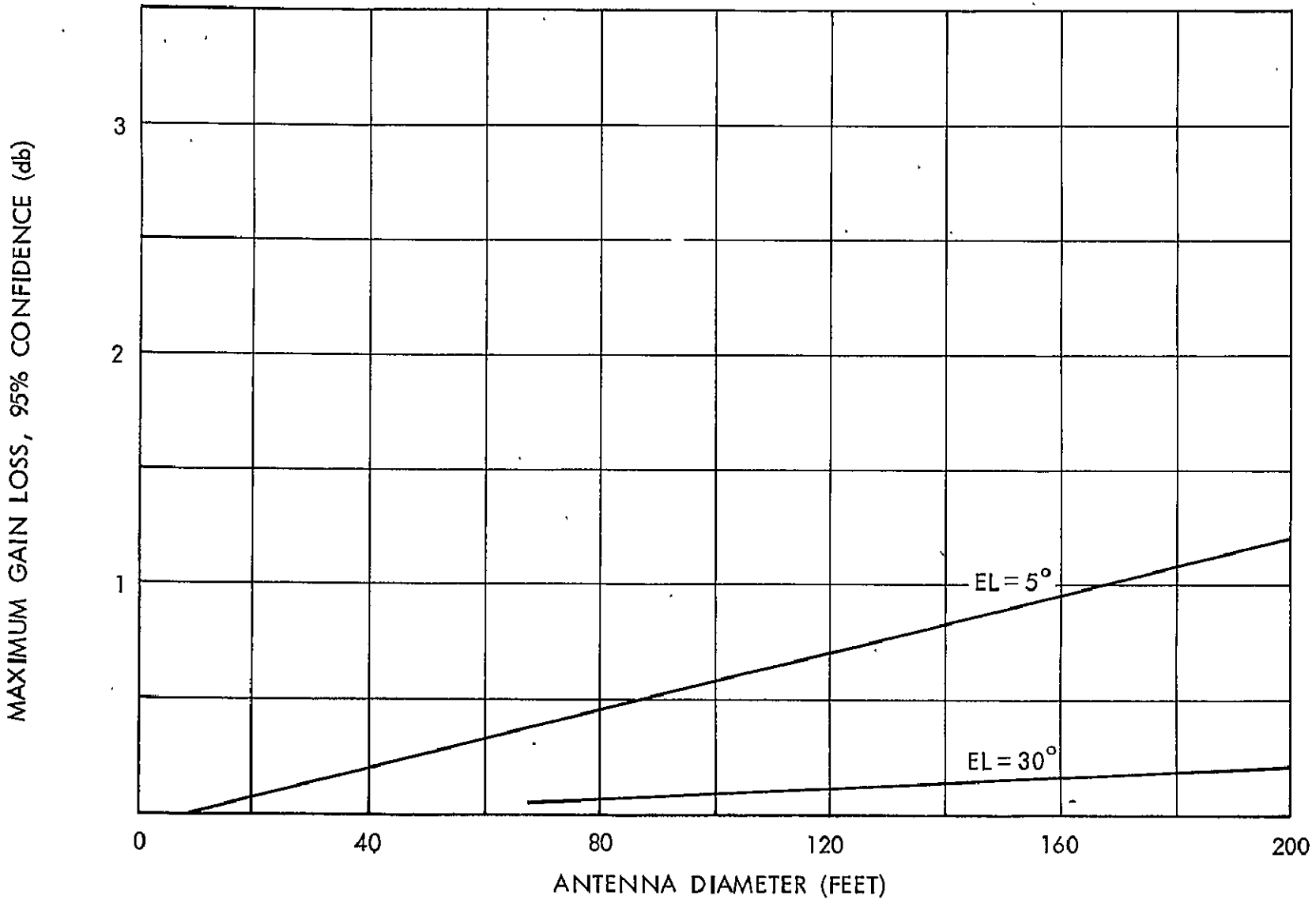

Figure B-2: Maximum Gain Loss vs. Antenna Diameter for Tropospheric Phase Front Distortion, F = 10 GHz

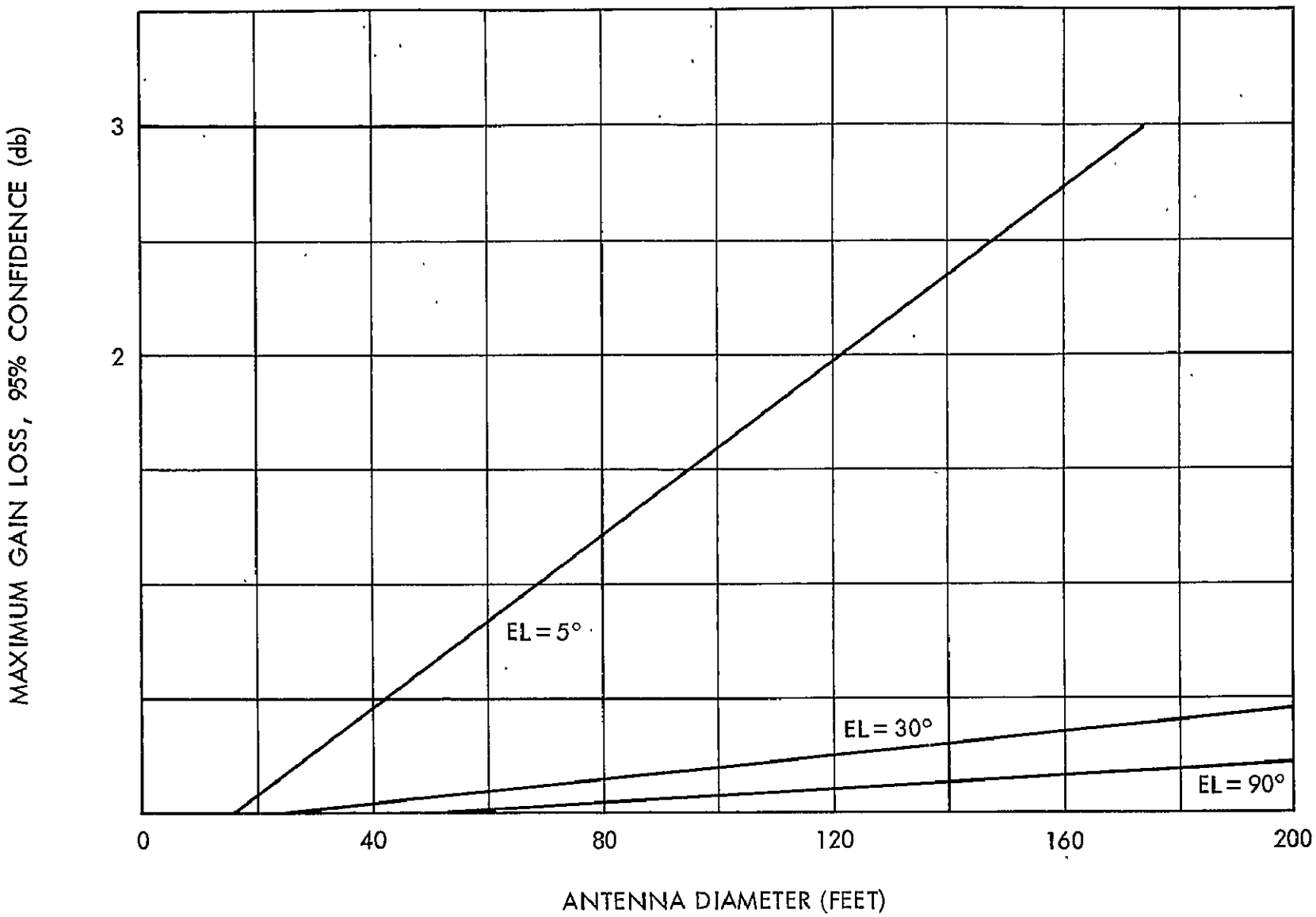

Figure B-3: Maximum Gain Loss vs. Antenna Diameter for Tropospheric Phase Front Distortion, F = 15 GHz

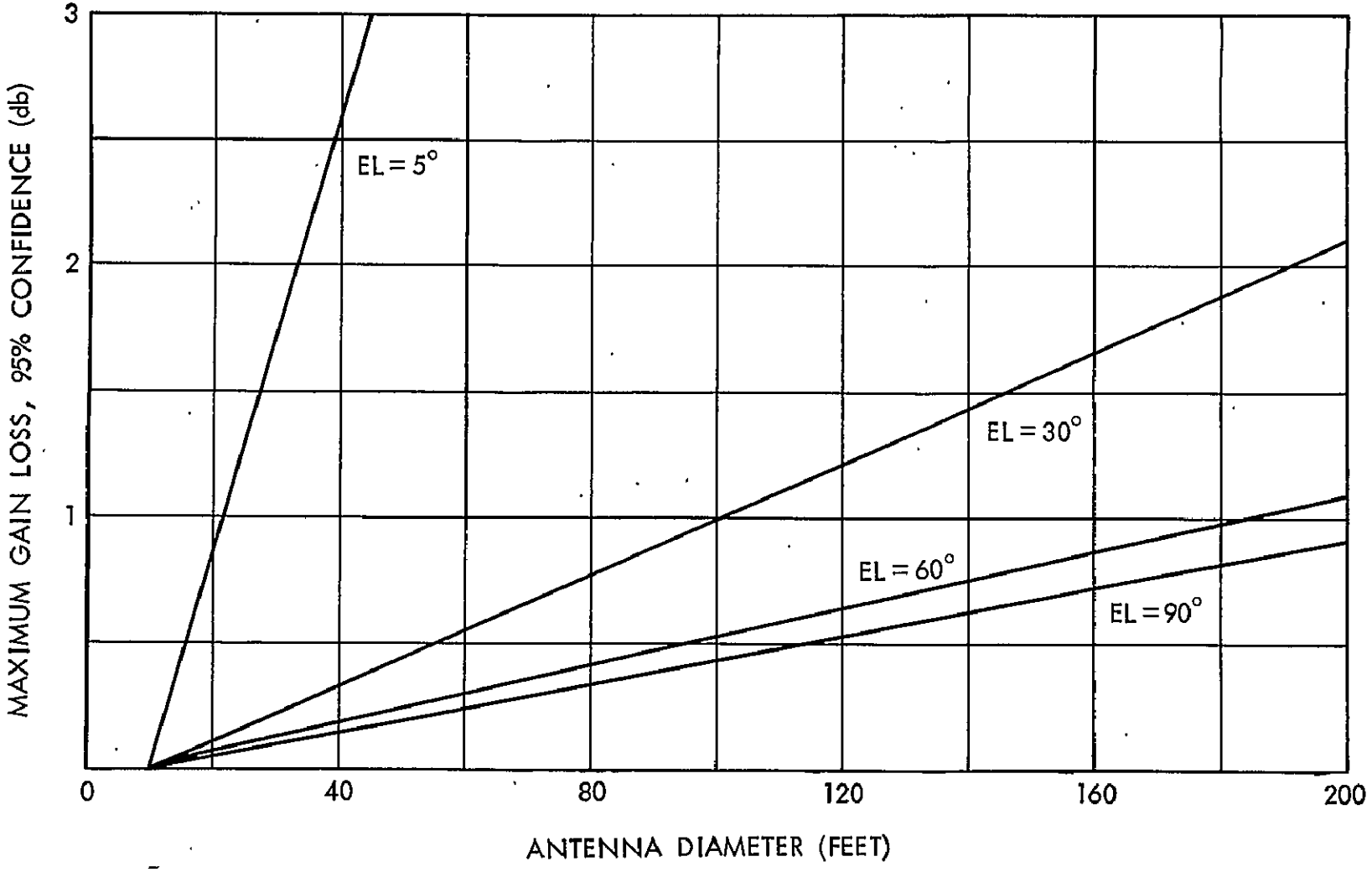

Figure B-4: Maximum Gain Loss vs. Antenna Diameter for Tropospheric Phase Front Distortion, F = 30 GHz

The gain reduction curves (Figures B-1 through B-4) were computed for a 95% confidence. Therefore, there is no more than a 5% probability that the gain loss due to troposphere turbulence will exceed the values indicated in clear weather. The confidence interval was computed from the standard deviation (Equation B-1) assuming a normally distributed phase error distribution [28].

Ionosphere:

The single ray path characteristics are related to frequency and elevation as given below [29]

$$\sigma_i = \frac{0.825}{F} \quad \text{radians} \qquad \text{(B-5)}$$

where

σ_i = rms phase deviation of a single point on a phase front, mean equal to zero

F = frequency, GHz

The angle of arrival fluctuations caused by the ionosphere are related to frequency as

$$\sigma_{\beta i} = \frac{\lambda^2}{5} \quad \text{milliradians} \qquad \text{(B-6)}$$

where

λ = wavelength of signal

$\sigma_{\beta i}$ = rms deviation in angle of arrival

A plot of the fluctuation in angle of arrival is given in Figure B-5 for both the troposphere and ionosphere. Equations B-1, B-2, B-5, B-6 are estimates of phase front distortion and angle of arrival fluctuations accurate to an order of magnitude only.

The 50% correlation distance for single ray paths ranges from 4 to 6.5 km [29]. Assuming a 50% correlation distance of 5 km, Equations B-3, B-4 and B-5 were used to compute the gain loss of a single aperture antenna versus frequency for several antenna diameters (Figure B-6). At 2 GHz and above, the gain loss of a single aperture antenna, due to ionospheric phase front distortion, is insignificant considering the order of magnitude accuracy of the models. Below 2 GHz, the

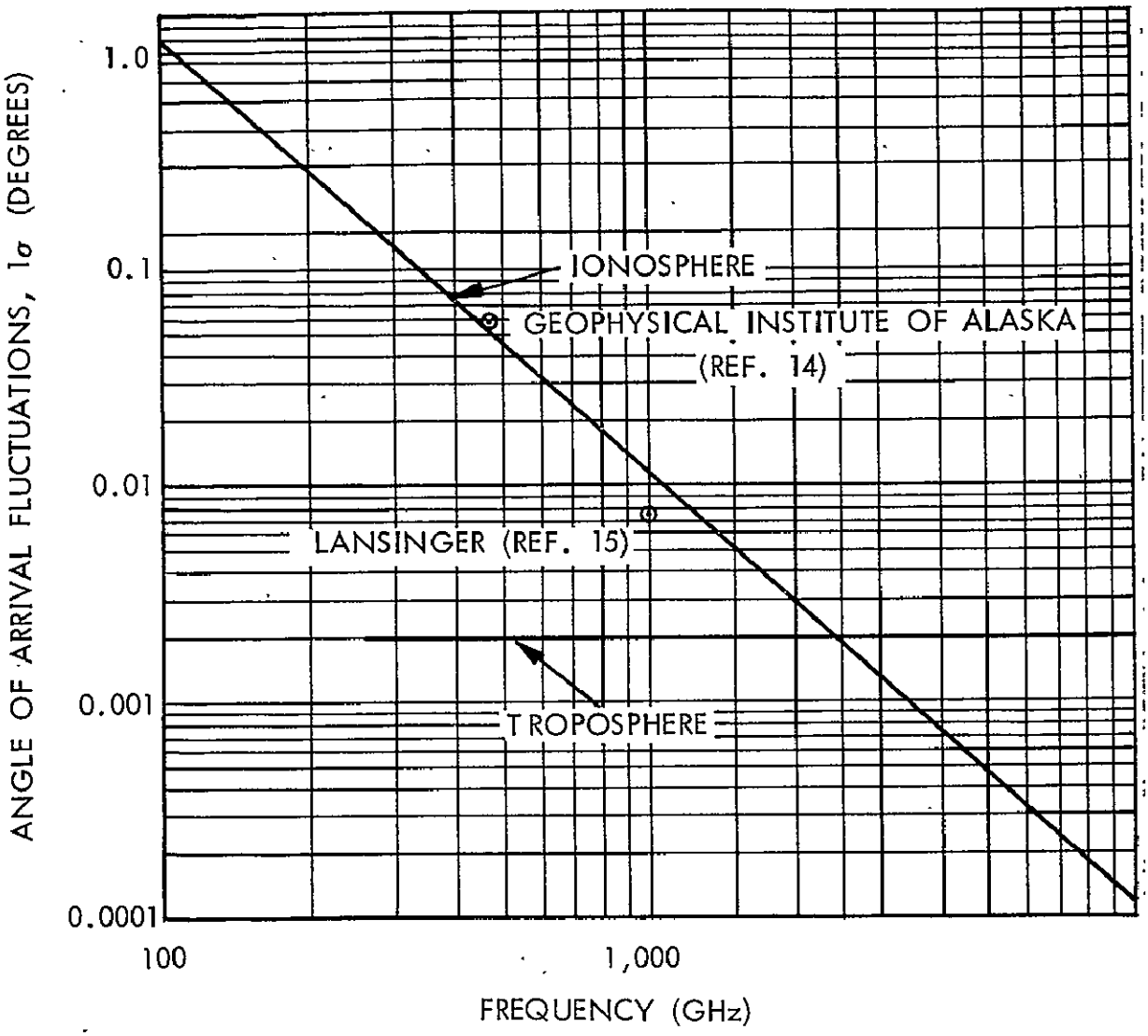

Figure B-5: Angle of Arrival Fluctuations vs. Frequency

gain loss rapidly increases. It should be remembered that these curves are upper limits (95% confidence) on the gain loss for an undisturbed ionosphere.

Phase front distortions much more severe than indicated by Equations B-5 and B-6 have been measured in the equatorial region [30-33]. These scintillations are composed of amplitude variations as well as phase front distortion. The amplitude scintillations are not the result of energy absorption in the ionosphere at VHF, but rather to the focusing of energy forming an effective interference pattern on the earth [12]. The movement of this interference pattern has been measured [12, 31]. Received signal levels at the ground have been found to exceed expected levels (assuming no ionospheric effects) within bright

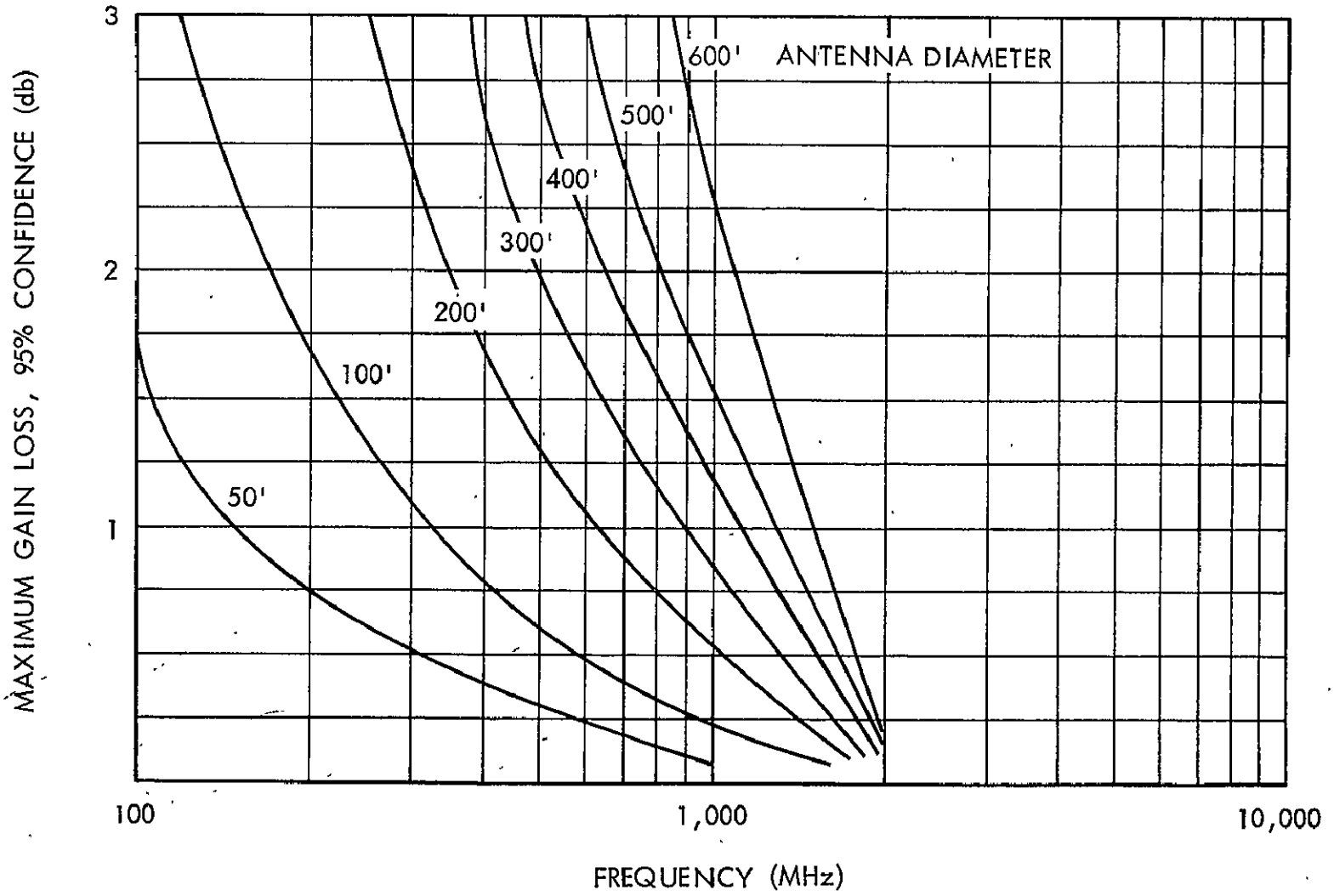

Figure B-6: Maximum Gain Loss vs. Frequency for Ionospheric Phase Front Distortion

zones of the interference pattern and to indicate substantial fading in dark zones.

The separation between antennas for 50% correlation of amplitude scintillations has been determined experimentally to range from 500 feet [12] to 1,000 feet [34] with the array baseline oriented parallel to the equatorial plane. The refractive mechanism of the ionosphere is highly elliptical [34] with 50% correlation distance approximately 20 times greater for a baseline oriented orthogonal to the equatorial plane.

The amplitude scintillation characteristic of the ionosphere in the equatorial region would comparably affect a single aperture antenna or a closely spaced array. Therefore, the spacing between array elements under these circumstances should be at least 500 feet and preferably 1,000 feet to minimize the possibility of simultaneously experiencing amplitude scintillations at the array elements. The array baseline should be parallel to the equatorial plane.

Spacing the antennas at 1,000 feet will increase the phase deviation between signals received at the array elements. However, phase correcting circuits will insure coherent addition of the signals in the combining receiver. The time delay between reception at the array elements can easily be compensated with a time delay system if the modulation bandwidth requires such correction (Section 2.3 of this report). The 1,000 feet spacing between array elements, therefore, would not significantly affect total system performance and capability.

5 ACKNOWLEDGEMENT

Acknowledgement is made for the work of Thomas W. Tunney in experimental phases of both the VHF and S-band programs and to John E. Fuchs for his work in the operation and data reduction of the VHF program.

REFERENCES

1. J. E. Eberle, An Adaptively Phased, Four Element Array of Thirty-Foot Parabolic Reflectors for Passive (Echo) Communication Systems, prepared by Ohio State University under Contract AF 30(602)-2166.

2. J. H. Shraeder, "Receiving System Design for the Arraying of Independently Steerable Antennas," IRE Transactions on Space Electronics and Telemetry, pp 148-153, June 1962

3. R. E. Taylor, "Satellite Tracking Simultaneous-Tabing Monopulse Receiving System with Polarization Diversity Capability," IEEE Transactions on Aerospace and Electronic Systems, pp 664-680, July 1967

4. W. J. Bickford, et al., Study of a Signal Processor Employing a Synthetic Phase Isolator, prepared by the Raytheon Company for NASA/ERC under Contract NAS 12-82, October 3, 1966

5. Analytical Study to Define an Experimental Program for the Evaluation and Optimization of Multi-Element Large Aperture Arrays, prepared by the Research Triangle Institute for NASA/LRC under Contract NAS1-3780, September 1964, pp 5-22 to 5-28

6. D. G. Brennan, "Linear Diversity Combining Techniques," IRE Proceedings, p 1083, June 1959

7. R. E. Taylor, "Field Operable Carrier-to-Noise Ratio (CNR) Monitor," Quarterly Progress Report of R&D Technological Development Activities, March 1970

8. L. Katz, R. Honey and V. Simas, Optimum Pre-Detection Diversity Receiving System, Patent Number 3,341,778

9. F. M. Gardner, Phaseback Techniques, John Wiley and Sons, Inc., 1966, pp 55-58

10. F. J. Altman and W. Sichak, "A Simplified Diversity Communications System with Polarization Diversity Capability," IEEE Transactions on Communication Systems, pp 50-55, March 1956

11. Investigation and Study of a Multi-Aperture Antenna System, Final Report prepared by Electronic Communications, Inc. for NASA/GSFC under Contract NAS5-3472, April 1964, pp 33-35

12. T. S. Golden, A Note on Correlation Distance of the Equatorial Ionosphere, NASA/GSFC Report X-520-69-345, August 1969

13. Time Delay Units for IF Applications, Progress Report prepared by the Philco-Ford Corporation for NASA/GSFC under Contract NAS5-10083, January 15, 1967 to February 15, 1967

14. Analytical Study of Arrays, Research Triangle Institute, pp 6-32 to 6038

15. L. F. Deerkoski, H. Estep, P. A. Lantz and N. A. Raumann, Ku-Band Tracking and Data Relay Satellite Ground Angenna Study, NASA/GSFC X-525-70-200, June 1970, p 4-6

16. Deep Space Communication and Navigation Study, Bell Telephone Laboratories, NASA/GSFC Contract NAS5-10293, Volume 2, May 1, 1968, pp 36-48

17. B. R. Stack, An Approximate Expression for the Cost-Gain Relationship in Large Parabolic Antennas, Stanford Research Institute, December 1967, pp 11-13

18. P. E. Potter, W. D. Merrick and A. C. Ludwig, "Big Antenna Systems for Deep-Space Communications," Astronautics and Aeronautics, p 90, October 1966

19. Bell Telephone Laboratories, Study, Volume 3, p 2-1

20. P. E. Potter, "Big Antenna Systems," p 92

21. J. H. Schraeder, "Receiving System Design for the Arraying of Independently Steerable Antennas," IRE Transactions on Space Electronics and Telemetry, p 151, June 1962

22. W. Gruhl, P. Villone and W. A. Mecca, Jr., Tracking and Data Relay Satellite Network (TDRSN) Cost and Benefit Study, NASA/GSFC X-264-69-526, December 1969, p 9

23. Investigation of Multi-Aperture Systems, Electronic Communications, Inc., pp 11-26

24. Feasibility Analysis of a Deep-Space Receiving Terminal Array of Large Equivalent Aperture, Final Report prepared by the Stanford Research Institute for NASA/LRC under Contract NAS1-3075, May 1964

25. Ibid. p 213

26. Ibid. p 215

27. J. Ruze, "Antenna Tolerance Theory — A Review," IEEE Proceedings, p 633, April 1966

28. Feasibility Analysis, SRI, pp 37-8

29. Ibid. p 223

30. H. G. Booker, "The Use of Radio Stars to Study Irregular Refraction of Radio Waves in the Ionosphere," Proceedings of the IRE, pp 298-314, January 1958

31. G. S. Kent and J. R. Koster, "Some Studies of Night Time F-Layer Irregularities at the Equator Using VHF Signals Radiated From Earth Satellites," Spread F and Its Effects Upon Radiowave Propagation AGARDograph No. 95, Mackay and Co., Ltd., London, pp 333-356, 1966

32. P. Bandyopadhyaz and J. Aarons, "The Equatorial-F-Layer Irregularity Extent as Observed from Huancayo, Peru," Radio Science, pp 931-942, June 1970

33. R. J. Coates and T. S. Golden, Ionospheric Effects on Telemetry and Tracking Signals From Orbiting Spacecraft, NASA/GSFC X-520-68-76, 1968

34. G. S. Kent and J. R. Koster, F-Layer Irregularities, p 346